RECEIVED
Nov 15 10 23 AM '65
OFFICE OF GRANTS & RESEARCH CONTRACTS

[redacted]

GPO PRICE $ ____________

CFSTI PRICE(S) $ ____________

Hard copy (HC) 4.00

Microfiche (MF) 1.00

ff 653 July 65

FACILITY FORM 602

N67 12041 (ACCESSION NUMBER)	(THRU)
145 (PAGES)	1 (CODE)
CR-80057 (NASA CR OR TMX OR AD NUMBER)	25 (CATEGORY)

PRINCETON UNIVERSITY

DEPARTMENT OF

AEROSPACE AND MECHANICAL SCIENCES

NATIONAL AERONAUTICS
AND
SPACE ADMINISTRATION

Research Grant NsG-306-63

STRUCTURE OF THE CURRENT SHEET
IN A
PINCH DISCHARGE

Report No. 783*

Prepared by Rodney L. Burton
Rodney L. Burton

Approved by R. G. Jahn
Robert G. Jahn
Associate Professor
and Research Leader

*This report is a reproduction in entirety of the Ph.D. dissertation of Mr. Rodney L. Burton. It is submitted to the sponsor and to the distribution list in this form both as a presentation of the technical material, and as an indication of the academic program supported by this Grant.

September 1966

Guggenheim Laboratories for the Aerospace Propulsion Sciences
Department of Aerospace and Mechanical Sciences
PRINCETON UNIVERSITY
Princeton, New Jersey

ABSTRACT

The structure of a propagating current sheet in a cylindrical pinch discharge in argon is studied experimentally and analytically. The azimuthal magnetic field, B_θ, is mapped throughout the discharge, yielding patterns of current density, $\vec{j}$. From an inventory of the $\vec{j} \times \vec{B}$ distributions, it is deduced that the bulk of the gas is accelerated to the current sheet velocity. The patterns of radial electric field, E_r, normal to the current sheet, are mapped with a coaxial floating double probe. Based on a one-dimensional, constant compression model, the E_r field appears to be of sufficient magnitude to allow conduction of all axial current by electrons in collisionless $\vec{E}_r \times \vec{B}_\theta$ drift. This field is not strong enough, however, to accelerate ambient ions to the sheet velocity, suggesting that gasdynamic forces also participate in the interaction. This model also identifies ohmic heating in the sheet with the product of radial ion current density and E_r. Comparative measurements in neon, argon, and krypton, keeping the ambient mass density constant, indicate that this ohmic heating decreases with increasing molecular weight.

CONTENTS

LIST OF ILLUSTRATIONS

LIST OF ILLUSTRATIONS-cont'd

LIST OF ILLUSTRATIONS-cont'd

LIST OF ILLUSTRATIONS-conc'd

Chapter I

INTRODUCTION

It is well known that manned voyages from the Earth to Mars, Venus, and other bodies will take many months, and cannot be accomplished efficiently using present-day chemical rockets. To carry the greatest payload, interplanetary propulsion systems must use drastically less fuel than chemical systems, and this can only be accomplished by increasing the propellant exhaust velocity. To date, a wide variety of electric propulsion systems are being studied, capable of producing two to twenty times the exhaust velocity of chemical rockets. The drawback to electrical systems is that they require large amounts of power from a relatively heavy source, and operate at relatively low thrust levels. Therefore, electric propulsion systems for long interplanetary missions must convert electrical energy to exhaust energy with high efficiency, and must also operate at the highest possible thrust density. Pulsed electromagnetic acceleration of a plasma promises to meet these two propulsion requirements.

Between 1820 and 1825, experiments by Biot and Savart, and later by Ampere, established that a current carrying wire generates around itself a magnetic induction field $\vec{B}$. The experiments also established a force law between two current carrying wires, written in terms of $\vec{B}$ and the current in the wires. This law for the electromagnetic force density on a conductor is more generally expressed in terms of current density $\vec{j}$:

$$\vec{f} = \vec{j} \times \vec{B} \qquad [newtons/m^3]$$

so that force is perpendicular both to current and to magnetic field. Neglecting the very small displacement current, $\vec{B}$ and $\vec{j}$ are related by Ampere's Law:

$$\vec{\nabla} \times \vec{B} = \mu_0 \vec{j}$$

The study of fluid flow in which the force $\vec{f}$ is important constitutes the subject of magnetogasdynamics.

The most direct way to generate a large electromagnetic force is to use very high levels of current. Because these high currents are most easily produced on a transient basis, electromagnetic thrusters generally operate in pulsed fashion, and their performance is an average over many pulses. It is implied in the following experimental and theoretical work that the results of investigating a single pulse will be relevant to a continually pulsed thruster.

The cylindrical linear pinch, which is investigated in the present experiments, is one of several discharge devices which invoke self-induced $\vec{j} \times \vec{B}$ forces to accelerate plasma. Six of the more prominent geometries, including the linear pinch, are shown in Fig. 1. In all of these devices, current flows

AP25-4158-66

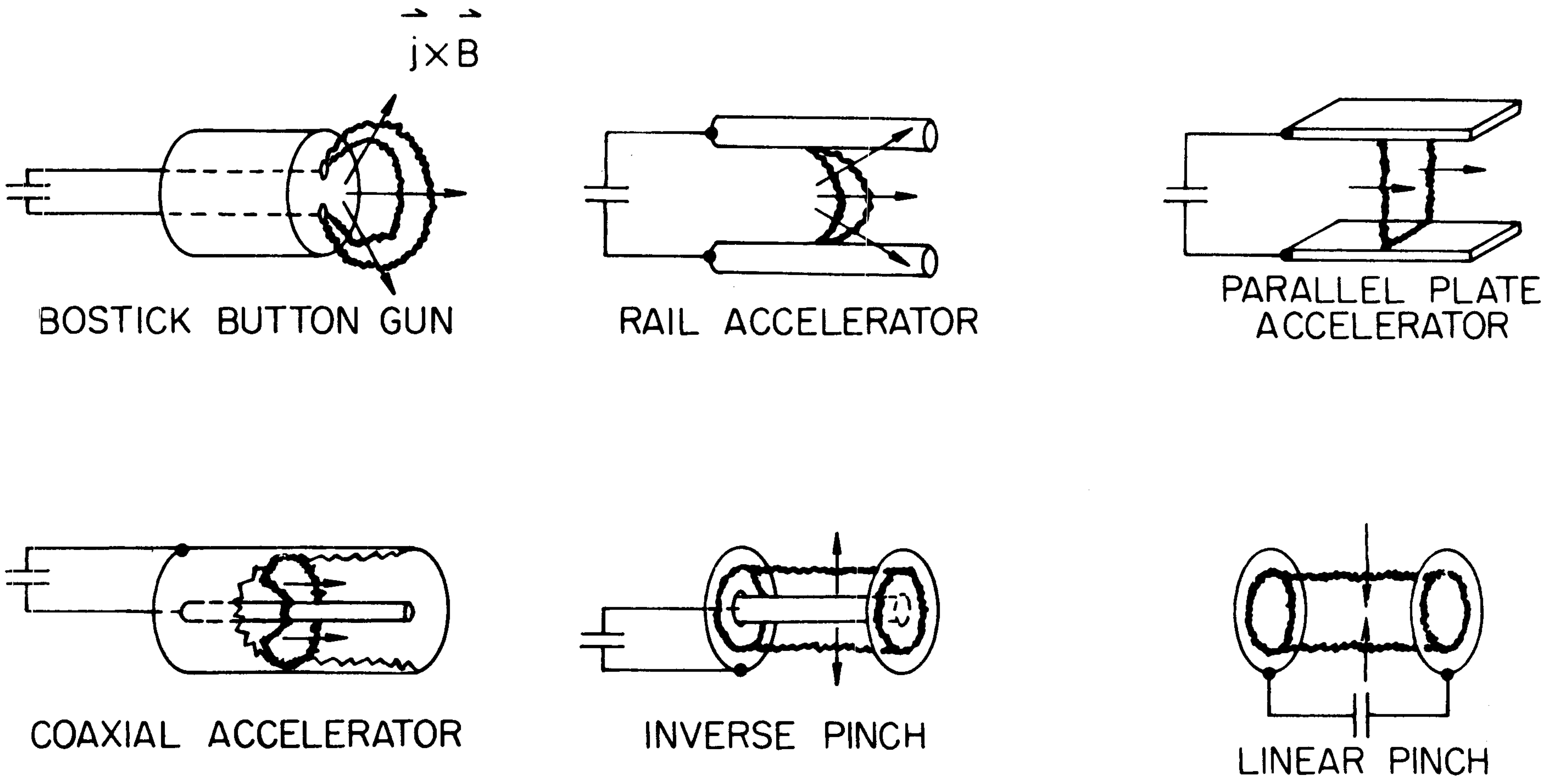

BOSTICK BUTTON GUN

RAIL ACCELERATOR

PARALLEL PLATE ACCELERATOR

COAXIAL ACCELERATOR

INVERSE PINCH

LINEAR PINCH

PULSED PLASMA ACCELERATOR GEOMETRIES

FIGURE 1

directly through a gas in contact with the electrodes. The Bostick button gun and the rail accelerator have the least propulsion application, because of strong three-dimensional effects, and will not be discussed further. The parallel plate accelerator, coaxial accelerator, inverse pinch, and linear pinch reduce the experimental problem to two dimensions, since all discharge properties are approximately constant along the magnetic field lines. The motion of the current sheet in these latter devices can even be described by one-dimensional dynamic models.

All of the discharge devices in Fig. 1 have in common a capacitor bank, a switch, two electrodes, and a test gas between the electrodes. Closing the switch connects the charged capacitor bank to the electrodes, and allows a large current to flow through the circuit when the test gas becomes sufficiently ionized. Current flowing through the test gas generates a $\vec{J} \times \vec{B}$ force, the direction of which is shown by the arrows. In the case of the linear pinch, $\vec{J} \times \vec{B}$ points radially inward, and the plasma which carries the current accelerates inward to form a thin central plasma column, constituting the "pinch effect."

The most striking similarity among the four discharge geometries is the initial formation and subsequent high velocity propagation of an intense uniform current sheet. This current sheet accelerates, with varying efficiency, the gas into which it propagates. Although the present experiments are conducted in a linear pinch, there is no reason why the resulting description of the physical mechanisms in the current sheet should not be applicable to the parallel plate, coaxial, and inverse pinch accelerators. It will thus be helpful to consider the results of the present study in the light of previous investigations in all four devices. The purpose of the following brief review of past work is to indicate that many contradictory results have been obtained, many different theories proposed, and that only a few conclusions have been reached.

The first theoretical prediction of the radial motion of the current sheet in a linear pinch was the snowplow model of Garwin and Rosenbluth.(1) An infinitesimally thin, cylindrical current sheet, driven by $\vec{J} \times \vec{B}$ force, was assumed to reflect particles as it propagated into a collisionless test gas, imparting to the test gas a radial velocity equal to twice the sheet velocity. A modification of this theory by Colgate(2) assumed that the sheet did not reflect, but absorbed the test gas in a thin layer on the sheet surface. Whereas Rosenbluth stipulated a constant applied voltage to the electrodes, Colgate pointed out that sheet motion, current, and voltage could be determined by the simultaneous solution of the coupled momentum and circuit equations. The solution of these equations is discussed in Appendix A.

In the present linear pinch investigation, the snowplow model of Colgate accurately describes the motion of the current sheet. Other theoretical models have also been proposed, and three of these have been summarized by Granet and Guman.(3) In the quasi-steady or hydrodynamic model, the current sheet is assumed to act as a magnetic piston, driving a gasdynamic shock ahead of it. Uniform conditions are assumed between the shock and the piston, and this model is therefore applicable to a parallel plate accelerator. In the slug model, it is assumed that all of the test gas is accelerated by $\vec{j} \times \vec{B}$ force uniformly at time zero, and that no additional mass is entrained by the moving current sheet. This simple model is useful for predicting current sheet motion in metal film discharges, and in certain accelerators using pulsed injection of the test gas.

A more sophisticated gasdynamic model, particularly applicable to cylindrical geometries, assumes that a magnetic piston propels a gasdynamic shock into the test gas, and that an unsteady flow field exists between the shock and the piston. Rowell has applied this model to the linear pinch,(4) and presents solutions of the piston trajectory for various assumed shock trajectories.

It is important to note that many references on high current discharges, theoretical and experimental, refer to shocks and shock waves, or otherwise imply that gasdynamic shocks are being driven by the current sheet. However, no experiments have yet conclusively established from density measurements that a shock can propagate ahead of a magnetic piston. For instance, Jensen and co-workers measured luminous front trajectories in a parallel plate accelerator, and assumed that the luminosity represented a pressure wave.(5) Allen based a theory of the linear pinch on a strong shock wave model.(6) The existence of a gasdynamic shock was presumed, but in fact never proven, in numerous other references.

The search for a pressure discontinuity has been hampered to date by the lack of a good diagnostic technique. The need for a fast rise time pressure transducer has been partially solved by the thin piezoelectric crystal transducer, which can rather easily respond to the arrival of a pressure front with a one microsecond risetime. Work by York at Princeton has raised the possibility of an order of magnitude improvement in transducer response, but more development is needed. In 1962, piezoelectric transducers developed at the California Institute of Technology were used by Vlases to measure arrival times of pressure fronts in an inverse pinch.(7) Vlases found a pressure front slightly ahead of the current sheet in helium, and coincident with or trailing the current sheet in argon. More recently, some doubt was cast on the Vlases results by Sorrell, working in the same laboratory.(8) New results indicated that in all cases the pressure front in the inverse pinch trailed the current sheet, and that the separation increased with increasing molecular weight of the test gas.

Although the infinitesimally thin sheet snowplow model proves serviceable in several discharges in predicting current sheet trajectories, more complex descriptions are needed to explain the observed current sheet structure, and the mechanisms of particle acceleration and current conduction. Burkhardt and Lovberg investigated a coaxial gun, in which a radial current sheet accelerated deuterium plasma in the axial direction.(9) Using magnetic probes, the current sheet was found to be planar, and about 1 cm. thick. By means of a specially developed electric field probe, an electrostatic potential difference was observed between the front and back edge of the moving sheet. At radii near the negative central cathode, this potential was sufficient to accelerate deuterium ions to sheet velocity. The potential difference across the sheet decreased as $1/r^2$, and near the anode was equal to one-third the cathode value. Burkhardt and Lovberg concluded that because of the small potential near the anode, the current sheet did not act as a snowplow but rather as a strong shock wave, imparting some momentum to the plasma. They also postulated that collisionless electrons moved toward the anode in $E_z \times B_\theta$ drift, and thereby conducted the current in the sheet.

Similar experiments by Lovberg performed in argon, and reported in a later paper,(10) showed a potential energy drop across the sheet of only 46 volts, compared to the argon ion energy relative to the sheet of 4600 volts. The current sheet thus only weakly accelerated the plasma, in the manner of a weak shock wave. As in the previous work in deuterium, it was assumed by Lovberg that the electrons carried the current.

Johansson, working with argon and hydrogen in an inverse pinch, concluded that the current was not carried by electrons, but by ions.(11) Unlike the Vlases' results, Johansson found an outward moving current sheet which was not planar, but tilted as much as 50°, as illustrated below.

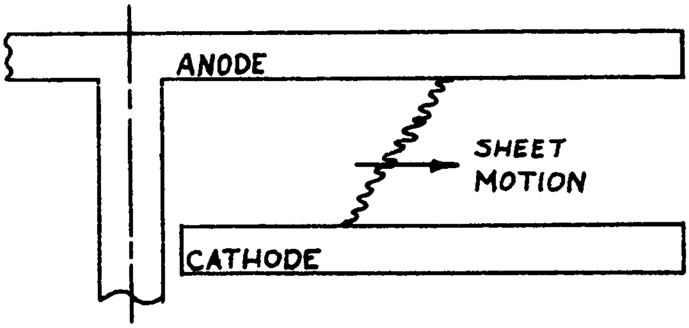

Using magnetic probes, an axial component of $\vec{j} \times \vec{B}$ force was found, as expected from the tilt of the current sheet. This force was found to be sufficient to drive ions toward the cathode, accounting for the conduction of current. Although the significance of an electric field in the current sheet was not clearly discussed, the inadequacies of a planar sheet model were clearly demonstrated.

Further evidence for conduction of current by ions was provided by Lovberg, investigating a parallel plate accelerator in hydrogen and nitrogen.(12) An anomalously low electrostatic potential was found across the current sheet in hydrogen, insufficient to accelerate the ions, and too low to provide electron current by $\vec{E} \times \vec{B}$ drift. It was hypothesized that the hydrogen ions were able to gyrate in the sheet without colliding, resulting in a net displacement current parallel to the sheet, and proportional to the rate at which ion-electron pairs entered the sheet. Strictly speaking, this current was conducted by the ions, whose Larmor radius was much larger than that of the electrons. After replacing the hydrogen by nitrogen, the ion Larmor radius became large compared to the sheet thickness, and ion current was greatly reduced. As expected, an electric field sufficient to accelerate nitrogen ions was once again observed, and accounted for electron current by $\vec{E} \times \vec{B}$ drift in the heavier gas.

As further evidence of the experimental contradictions in current sheet studies, various results have been reported on the effect of changing electrode polarity in a coaxial accelerator. It was mentioned above that Lovberg found a planar current sheet in a coaxial accelerator using deuterium, and a negative central electrode. Keck, using argon and a negative center electrode, found similar results.(13) Keck then found that reversing the electrode polarity destroyed the planarity of the sheet, which assumed a paraboloidal shape. In Keck's experiment, the anode current led the cathode current, as was found by Johansson.

In a more recent investigation using hydrogen, Lovberg observed a paraboloidal current sheet by schlieren photography.(14) It was found that the current sheet shape was independent of electrode polarity, in contradiction both to Keck's work, and to Burkhardt and Lovberg's previous observations of a planar sheet.

By no means have all the current sheet phenomena been discussed. The effects of electrical and thermal conductivity, viscosity, insulator heating, degree of ionization, type and pressure of test gas, etc. have been mentioned in the literature.(2)(15)(16) However, the contradictory experimental results, and multitude of proposed models, indicate that the physical mechanisms in the current sheet are not yet understood.

Chapter II

APPARATUS AND DIAGNOSTICS

A. DESCRIPTION OF THE DISCHARGE APPARATUS

The purpose of this chapter is to discuss the plasma pinch apparatus, and the application to it of various diagnostic techniques. Included in the discussion will be the mechanical design, construction, and operation of the closed chamber discharge, a description of each diagnostic tool, and the theoretical application of that tool in the plasma environment.

The main components of the discharge apparatus, called the 5" pinch (Figs. 2 and 3), are a pinch chamber, a gas-triggered switch, a coaxial transmission line, and a capacitor bank. The cylindrical pinch chamber measures 5" in diameter and 2" between the electrodes. The plane circular electrodes are aluminum, and the cylindrical insulator is pyrex, 1/4" thick. Two O-ring seals are mounted between the pyrex insulator and the electrodes. A pumping port in the center of the outer electrode (anode) holds a metal plug which sits flush with the electrode. Several .201" holes in the anode permit axial probing in the chamber, and are plugged when not in use.

The anode, which serves as electrical ground, is bolted to the outer conductor of the tubular transmission line. Two

JPR 2245

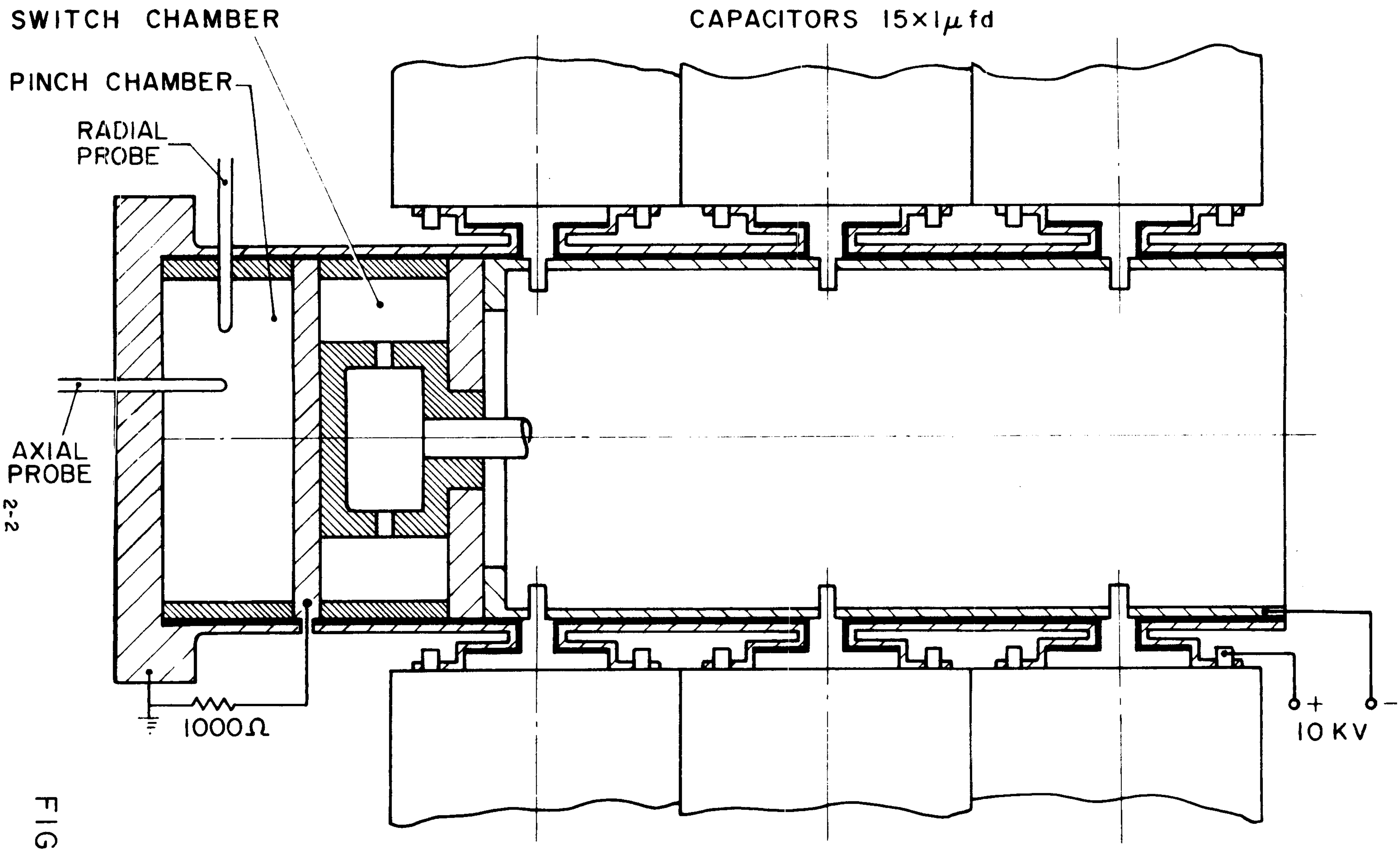

5" PLASMA PINCH APPARATUS (SCHEMATIC)

FIGURE 2

AP25-P38-66

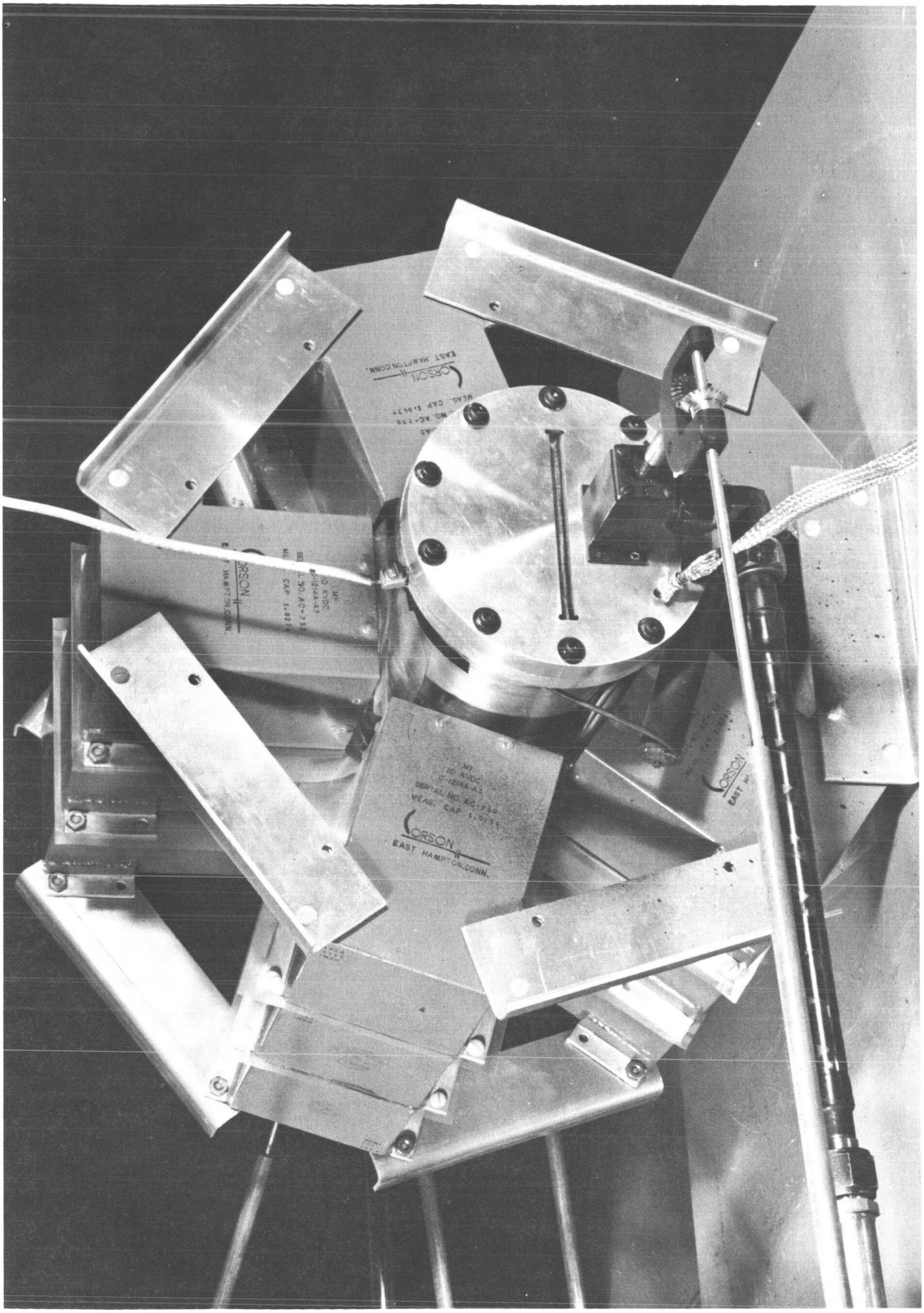

5" PINCH DISCHARGE MACHINE

FIGURE 3

holes in the outer conductor, 5/8" in diameter, permit radial probing in the chamber midway between the electrode. Another hole, 1-3/8" in diameter, admits a voltage tap to the cathode, and is insulated against 10,000 volts to ground. The total capacitance of the 15 unit capacitor bank is 15.7 μfd., and energy stored is 785 joules at 10,000 volts. The capacitor units are oil filled, measure 4-1/2" x 4-1/2" x 7", and were made by the Corson Electric Manufacturing Corporation. The ringing frequency of a shorted capacitor is 8×10^5 cps, corresponding to an inductance for each unit of 3.8×10^{-8} henries.

The gas-triggered switch, adjacent to the pinch chamber, is itself a pinch discharge of low inductance.(17) The annular switch electrodes, 14 cm. diameter by 2.5 cm. wide, are separated by 4 cm. The switch chamber is initially evacuated below the Paschen limit, to less than 10^{-3} mm Hg, and is triggered by the injection of argon. The discharge conducts the peak current of 3×10^5 amps with a resistance of about 3×10^{-3} ohms, and an inductance of about 3×10^{-9} henries. The high current discharge in the switch is similar to the discharge in the main chamber, except that a central plexiglas insulator prevents the inward pinching of the switch plasma. This switch will sustain about 500 discharges before it is unable to hold off 10,000 volts, and must be cleaned.

Figure 4 is a schematic sketch showing the distribution of inductance, capacitance, and resistance in the circuit. Comparison of total current with that predicted by the

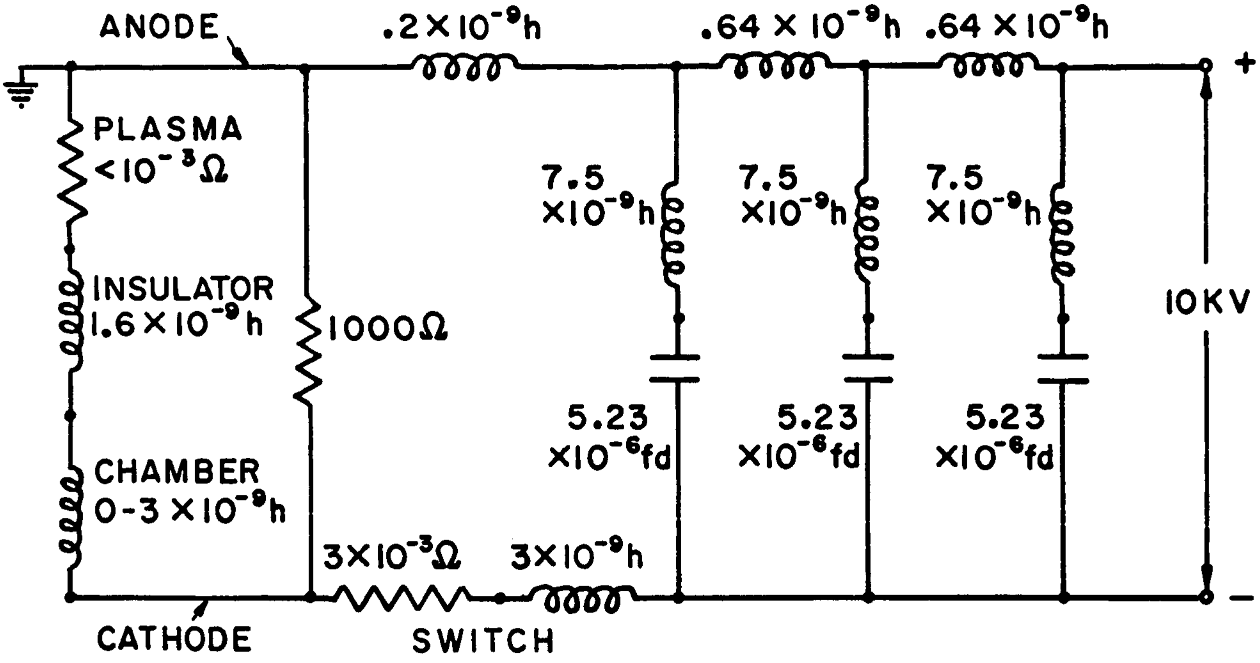

DISTRIBUTION OF ELECTRICAL CIRCUIT PARAMETERS IN THE 5" PINCH

FIGURE 4

snowplow theory (Appendix A) indicates that the total circuit resistance is about 5.5×10^{-3} ohms. The inductance of the circuit external to the chamber is approximately 7.7×10^{-9} henries.

Figure 5 shows the arrangement of the vacuum, gas filling, and switch triggering system. Vacuum is maintained by a Welch Duo Seal rotary vane mechanical pump, model 1397, which has a pumping speed of 15 ft.^{3}/min. down to 10^{-2} mm Hg, and an ultimate pressure of 10^{-4} mm Hg. The pinch chamber can be pumped down to 1 μ Hg in 30 seconds, through 3/4" vacuum lines. A refrigerated baffle and nitrogen cold trap are installed between the pump and the chamber, but were not used in these experiments.

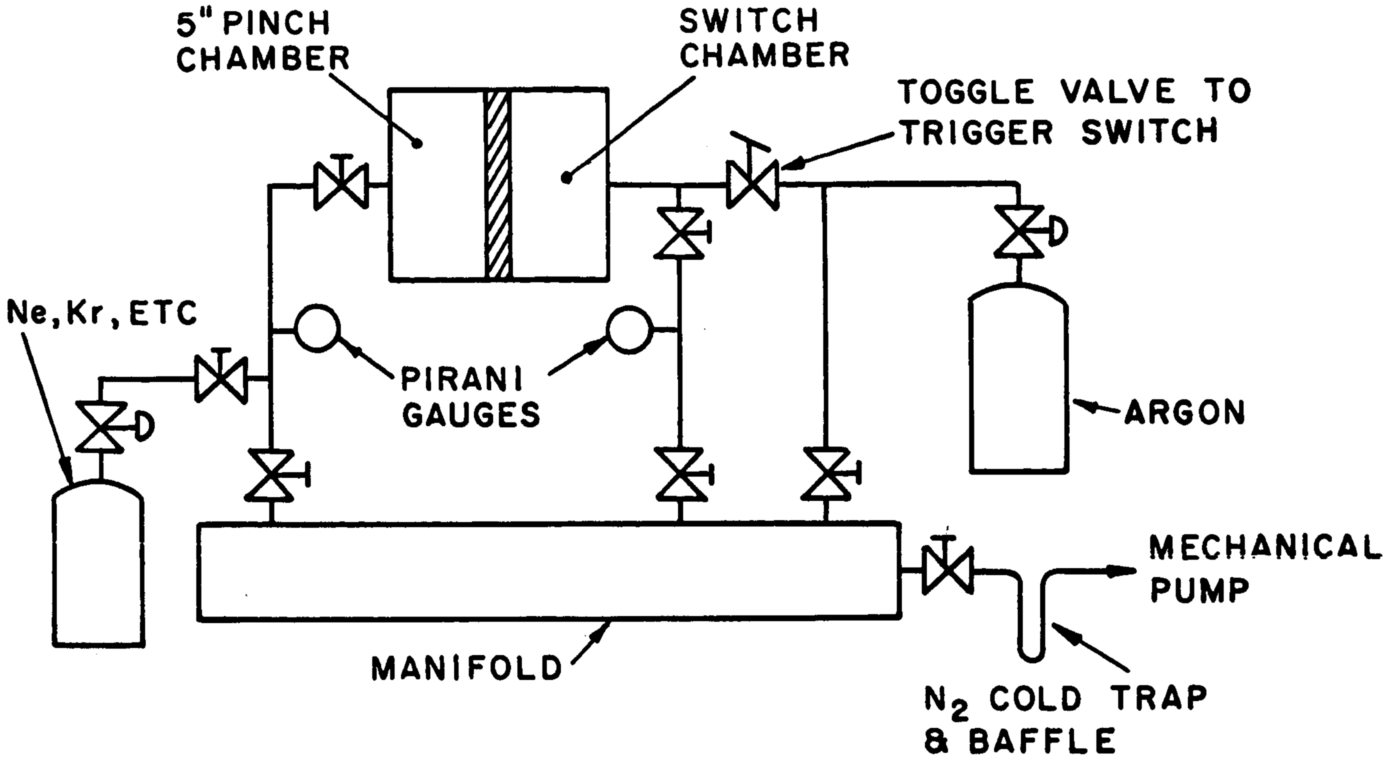

VACUUM, FILLING, & SWITCH TRIGGERING SYSTEMS FOR 5" PINCH

FIGURE 5

The argon supply is a 2,500 p.s.i. tank of commercial grade argon, purchased from the Liquid Carbonic Division, General Dynamics. The impurity level is approximately 50 parts per million (ppm). The gas pressure drops to 15 psi through a two-stage regulator, and is then fed to the switch and the pinch chamber through valves.

Test gas pressure in the range 1-2000 μ Hg is measured with a Pirani gauge, purchased from Consolidated Vacuum Corporation. The Pirani gauge measures the resistance change with gas pressure of a heated tungsten wire, which is cooled by the gas being measured. Heated sensing wires are located in the gas lines to the chamber and the switch, and the gauges are calibrated for each gas against a McLeod gauge. Readings taken several months apart indicated that the Pirani gauge is reproducible to 2 percent.

A D-C, 20 kV power supply, made by Sorensen and Company, Inc., charges the capacitor bank to 10,000 volts in about 20 seconds. The charging current is controlled through a Powerstat variable transformer, made by Superior Electric Co. The bank voltage is measured on a Triplett milliammeter, connected in series to the power supply with a 10 megohm resistor.

A 1,000 ohm resistor, shown in Fig. 2, connects the anode and cathode. This resistor insures that the cathode is at ground potential before the switch is fired. After the switch is fired, the cathode assumes a potential 10,000 volts below ground, and thus 0.1 amperes flow through the resistor and switch until the main chamber breaks down. The 1,000 Ω resistor also bleeds the charge of the capacitor bank if the main chamber refuses to fire. A shorting bar is used to short circuit the bank at low voltages.

The most efficient pinch machine design is that which delivers the largest fraction of the capacitor bank energy to the discharge chamber. This is achieved by increasing the ratio of pinch chamber inductance to total circuit inductance. In the laboratory's first two designs, the inductance of the pinch chamber was about 10 percent of the total circuit inductance, and the voltage across the electrodes was never more than 1,000 volts. In the 5" pinch the total circuit inductance was reduced by a factor of four, to about 11×10^{-9} henries, while average chamber inductance remained at $3x10^{-9}$ henries. The maximum voltage across the chamber electrodes was thus raised to 2,700 volts, and an integrated power measurement showed that 45 percent of the bank energy was delivered to the chamber (Fig. 17). The bulk of the reduction in circuit inductance is achieved by the use of low inductance capacitors and connections.

Unless special precautions are taken, arcing will occur across bolted connections in the discharge circuit. To prevent arcing, soft indium gaskets are squeezed between the two connecting parts. No arcing was observed in the connections of the 5" pinch using this method.

Although many impurities were present in the test gas and on the chamber electrodes, they did not measurably affect the experiments. The impurity level of the test gas was 50 ppm, and to this must be added an unknown (but small) amount of pump oil vapor, air, water vapor, vacuum grease vapor, and other trace impurities which are emitted from the chamber walls. The reproducibility of the magnetic probe data was insensitive to any attempt to lower the impurity level. Thus cleaning and polishing the chamber walls, pumping on the chamber for long periods of time, using liquid nitrogen in the cold traps, and flushing the chamber with argon, had no measurable effect on the dynamics of the pinch.

The effect of impurities was noticed somewhat in the early breakdown phase of the discharge. If enough deposits formed on the switch electrodes, the switch would not stand off 10,000 volts when evacuated, and had to be cleaned. A black layer, mostly carbon, was found on the electrodes in the switch and in the pinch chamber. Also contributing to early breakdown was the pitting of the electrodes, which created local ionizing electric fields. These pits were removed periodically.

B. THE GROUND PLANE, SCREEN ROOM, AND OSCILLOSCOPE

The bulk of the noise in high current transient discharges comes from two sources, both troublesome at high frequencies. In the first type of noise, discharge oscillations of sufficiently high frequency may develop voltages along the ground connection between the discharge and the oscilloscope, due to the nonzero inductance of the ground circuit. This voltage may in turn drive a current through a probe, or may appear as a voltage on a deflection plate in the oscilloscope. The problem is eliminated by connecting the oscilloscope to the discharge with a wide, low inductance, copper ground plane. In general, the inductance of the ground plane can be made low enough by making the width of the copper sheet exceed one-fifth of the length.

The second source of noise may be radiated radio frequency signals from the high voltage leads on the apparatus. This noise can sometimes be reduced by moving the oscilloscope far from the source, but a more direct method, used in these experiments, is to employ a screen room. The oscilloscope was completely enclosed within a Faraday Cage made of ordinary copper window screen, through which the R.F. noise could not penetrate. The signals from the probes were passed through a copper bulkhead in the side of the screen room on BNC cable connectors. The 117 V, 60 cycle power to the oscilloscopes was filtered outside the screen room by a Filtron R.F. interference filter, made by the Filtron Co., Inc. This filter will not pass a current with a frequency greater than 400 cycles per second.

The 5" pinch electrical circuit was grounded to the outside world in two ways. The oscilloscope was grounded through its power line to the laboratory electrical service, and for safety the 5" pinch was grounded by #8 wire to a pipe, imbedded 20 feet into the earth outside the laboratory. Both of these grounds had much higher inductance than the ground plane between the 5" pinch and the screen room.

All probe signals were fed to the screen room bulkhead, and thence to a 555 Dual-Beam oscilloscope, made by Tektronix, Inc. Tektronix Type L plug-in units were used to preamplify the signal. The traces were photographed on Polaroid Type 47 black and white film, and photographically enlarged to 8½"x11" for data reduction. The oscilloscope camera was a Model 196A, made by Hewlett-Packard. In some of the experiments, a Hewlett-Packard Pulse Generator was used to blank each beam of the oscilloscope simultaneously. This blanking pulse technique allowed accurate time correlation between the two recorded traces on the oscilloscope.

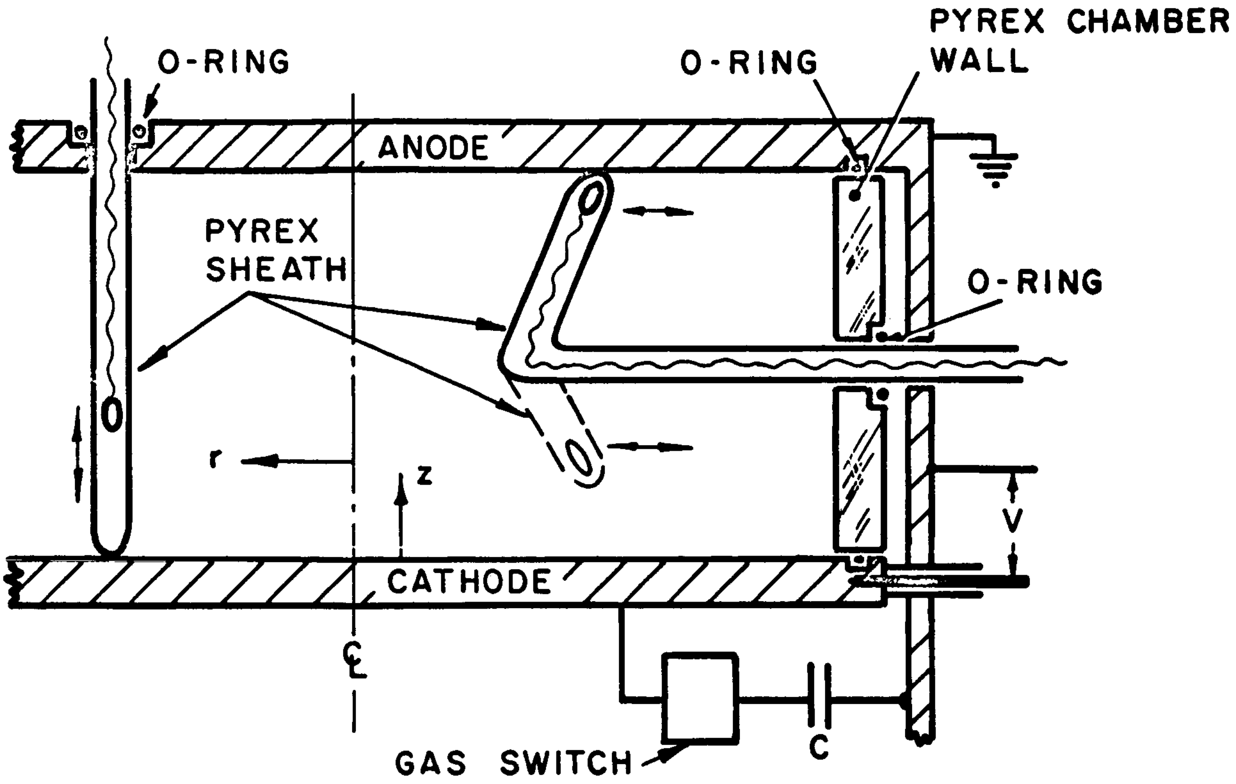

RADIAL & AXIAL PROBES IN 5" PINCH CHAMBER

FIGURE 6

C. MAGNETIC PROBE DESIGN

Small multi-turn inductive coils were used to measure the magnetic field distribution in the 5" pinch. The probe coils were five turns of #32 formvar covered wire, wound in a single layer on a #48 drill, 1.93 mm diameter. The coil leads were about 10 cm. long, tightly twisted to avoid inductive pickup, and were connected to 50 or 93 Ω coaxial cable. A protective pyrex sheath of 5 mm diameter completely surrounded the coil and leads, and extended either through the sidewall or through the anode (Fig. 6), sealed by an O-ring.

Rather than drill several holes at different positions in the sidewall, bent pyrex jackets (Fig. 6) were used to probe

AP25-4/33-66

near the electrodes. The jacket was bent more than 90°, so that the inward moving plasma sheet would impinge directly on the probe tip. These bent probes were employed in making radial surveys of magnetic field, while straight probes were employed in making the axial surveys. Under identical conditions, signals from the straight and bent probes agreed to within a few percent.

The possible pitfalls in using these probes are discussed by Lovberg,(19) who considers in some detail the perturbation of the plasma by the probe. The dominant effects, and their relative importance in the 5" pinch, are summarized in Table I:

Type of Perturbation	Effect in 5" Pinch
Plasma is cooled, striking probe	Measurable
Impurities from boiling probe surface	None
Probe alters pattern of discharge current	Measurable
Magnetic flux lines diffuse slowly out of plasma and into probe coil	Theoretically None

TABLE I

The first perturbation, the loss of plasma energy to the probe by particle convection, is strongly influenced by the thin Debye sheath which forms between the probe body and the plasma. Plasma electrons, which have small mass and high thermal velocity, strike the probe more frequently than heavy ions, and the probe surface acquires a negative charge. The insulating probe surface cannot conduct current; hence the electron sheath must repel enough electrons to satisfy the condition of equal ion and electron flux to the probe. Since the transport of heat in thermal plasmas is dependent on the particle thermal flux, the thermal conduction to the probe is greatly reduced by the negatively charged sheath. Following Lovberg's calculation of heat transfer by thermal flux to an insulated probe, it is assumed that argon plasma covers the entire probe surface, and that temperature and density are 5 e.v. and $10^{22}m^{-3}$. Neglecting the reduction of heat transfer by magnetic field, then the thermal energy transfer rate from argon is only about 10^4 watts. Power input to the plasma exceeds 10^8 watts, and hence thermal heating of the probe is negligible.

Kinetic energy loss to the probe is not negligible, especially when probing a short distance from the center of the chamber, since the probe jacket intercepts virtually all of the heavy ions streaming into it. The fractional kinetic energy loss to the probe is just probe area divided by current sheet area, which is typically only .05 for axial probes near the chamber wall. At the discharge center, however, the probe absorbs most of the energy of the stagnating plasma (350 joules), and as a result, shatters. For this reason very little probing was attempted in the very center of the pinch. When necessary, a nylon jacket protected the probe at the discharge center.

Furthermore, since the probe jacket absorbs most of the impinging heavy ions, no probing was attempted in the wake of another probe.

Impurities from the boiling probe surface are not a disturbing influence on the behavior of the discharge. All of the gases studied have a high molecular weight, and hence plasma density is not changed by small amounts of probe material of similar weight. Impurities are undoubtedly blasted off the probe by impinging ions, but these impurity particles are obstructed by the probe and cannot follow the current sheet. The probe probably contributes less impurity content to the plasma than does the insulating chamber wall, pump vapor, and other sources.

The local current distribution is severely modified by the presence of a probe, which effectively reduces the local electrical conductivity σ to that of the pyrex tube. The magnetic field will fringe inward into this zero conductivity region, reducing the $\vec{B}$ field gradient. As a result, the probe cannot detect large changes in $\vec{B}$ field which occur over a distance less than the probe radius. The smallest distance over which the $\vec{B}$ field rose from 10% to 90% of its maximum value was 7.5 mm, or 3 probe radii.

The effect of the probe on the $\vec{B}$ field became especially noticeable in one situation in the 5" pinch. If a straight probe was extended radially through the sidewall, a propagating current sheet was observed to double in thickness as it slid along the probe. It is suggested that the sheet was cooled by the probe as it moved away from the wall and slid along the pyrex sheath. Thus a nonconducting region encircled the probe, and grew with time to flatten the $\vec{B}$ field distribution. The problem was solved by minimizing the amount of pyrex over which the sheet had to travel to reach the coil. Axial straight probes and radial bent probes accomplished this satisfactorily.

$\vec{B}$ probes have no hope of working in a plasma with infinite conductivity, because the magnetic flux lines are tied to the plasma particles, which flow around the probe. With finite σ, the flux lines diffuse into the probe cylinder, of radius r_0, with a characteristic diffusion time:

$$t_d \sim \frac{1}{4}\mu_0 \sigma r_0^{4} \qquad [\mathrm{sec}]$$

Plugging in Spitzer's expression for σ,(20) calculated for an electron temperature of 5 e.v. and zero energy ions, the estimated diffusion time into a 2.5 mm radius cylinder is

$$t_d \sim 2 \times 10^{-8} \qquad [\mathrm{sec}]$$

This calculation is somewhat pessimistic, because it neglects plasma cooling near the probe, which lowers conductivity. The fastest risetime observed in the 5" pinch was 17×10^{-8} seconds, well within the expected probe response.

The probe output was integrated by a passive RC network shown below,

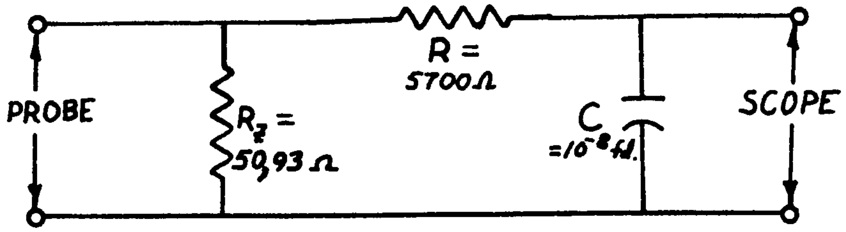

with a time constant RC = 57 usec. The total duration of the pinch experiment was only 1.6 usec, and integrator error is calculated to be less than 0.1% during the duration of the experiment. The probe output is proportional to $\frac{\partial B}{\partial t}$, which integrates to B on the oscilloscope face. A probe coil was calibrated by comparing its signal with the B_θ field measured by a calibrated Rogowski coil. For this calibration, the discharge chamber was opened to the atmosphere and shorted with a metal post, and the azimuthal B_θ field was calculated from Ampere's Law knowing the total current and the coil radial position:

$$B_\theta = \frac{\mu_0 I}{2\pi r_{\text{coil}}} \qquad [\text{weber/m}^2]$$

The method of calibrating the Rogowski coil to find total current is described in part (F) of this chapter.

D. ELECTRIC PROBE DIAGNOSTICS

The electric probe, first developed by Burkhardt and Lovberg,(9) is primarily a device to measure the difference in plasma potential between two points. Figure 7 shows the probe and pulse transformer used in the experiments, and indicates how the probe tip was constructed. The essential components of the system, shown in Fig. 8, are: 1) a ring and ball electrode pair, separated along the ring axis by 2 mm of epoxy insulator; 2) a parallel resistor R, which controls the current drawn through the plasma; and 3) an isolation-step down transformer to protect the oscilloscope from the plasma potential of several kilovolts. The probe leads are insulated by a 5 mm diameter pyrex sheath covering the outer coaxial conductor. The total angle of the conical probe tip is 35°.

The tip electrode of the probe is a hemisphere of copper, 0.3 mm diameter, having a surface area of 0.14 mm^2. The ring electrode is 2.8 mm in diameter, 0.15 mm wide, and has a surface area of 1.32 mm^2. Epoxy is used to vacuum-seal the probe tip, and to provide insulation between the two electrodes.

The coaxial probe leads, of 1/16" copper tubing and #26 copper wire, are connected to 3 feet of 50 ohm coaxial cable, in turn connected to the isolation-step down transformer (Fig. 7), the design of which is discussed in Appendix B. The transformer possesses a flat response between 1 and 16 megacycles, covering the range of interest for this experiment. To reduce parasitic inductance and improve frequency response, the 32 turn primary is wound tightly to the 1/2" diameter ferrite core, insulated from the core only by 1 mil teflon tape. The 4 turn secondary is wound on a 1-inch nylon bobbin, to reduce the capacitance between the secondary winding and the core. The

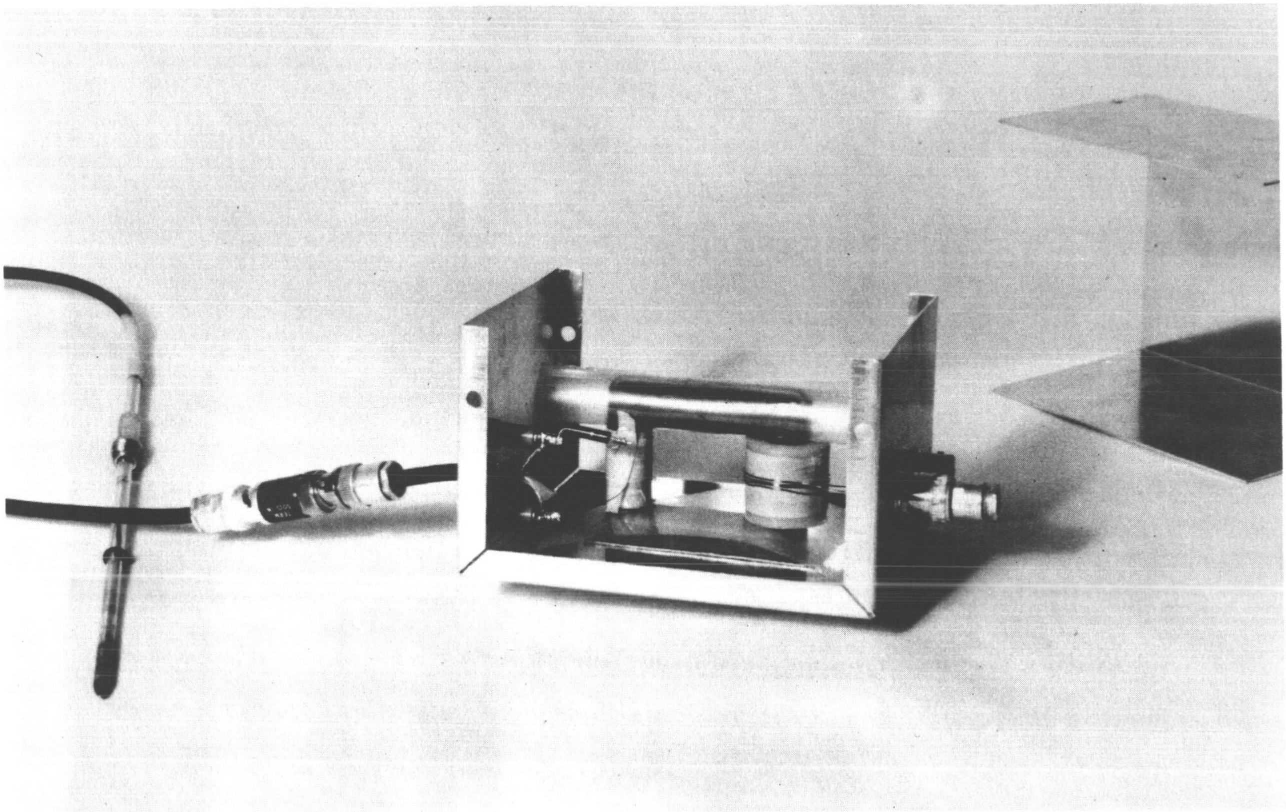

ISOLATION-STEP DOWN TRANSFORMER & ELECTRIC PROBE

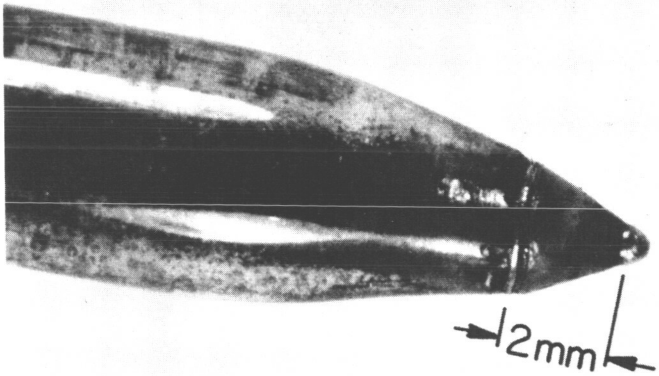

AD2S-PS03-66

RING & BALL ELECTRODES ON CONICAL PROBE TIP

FIGURE 7

AP25-4055-66

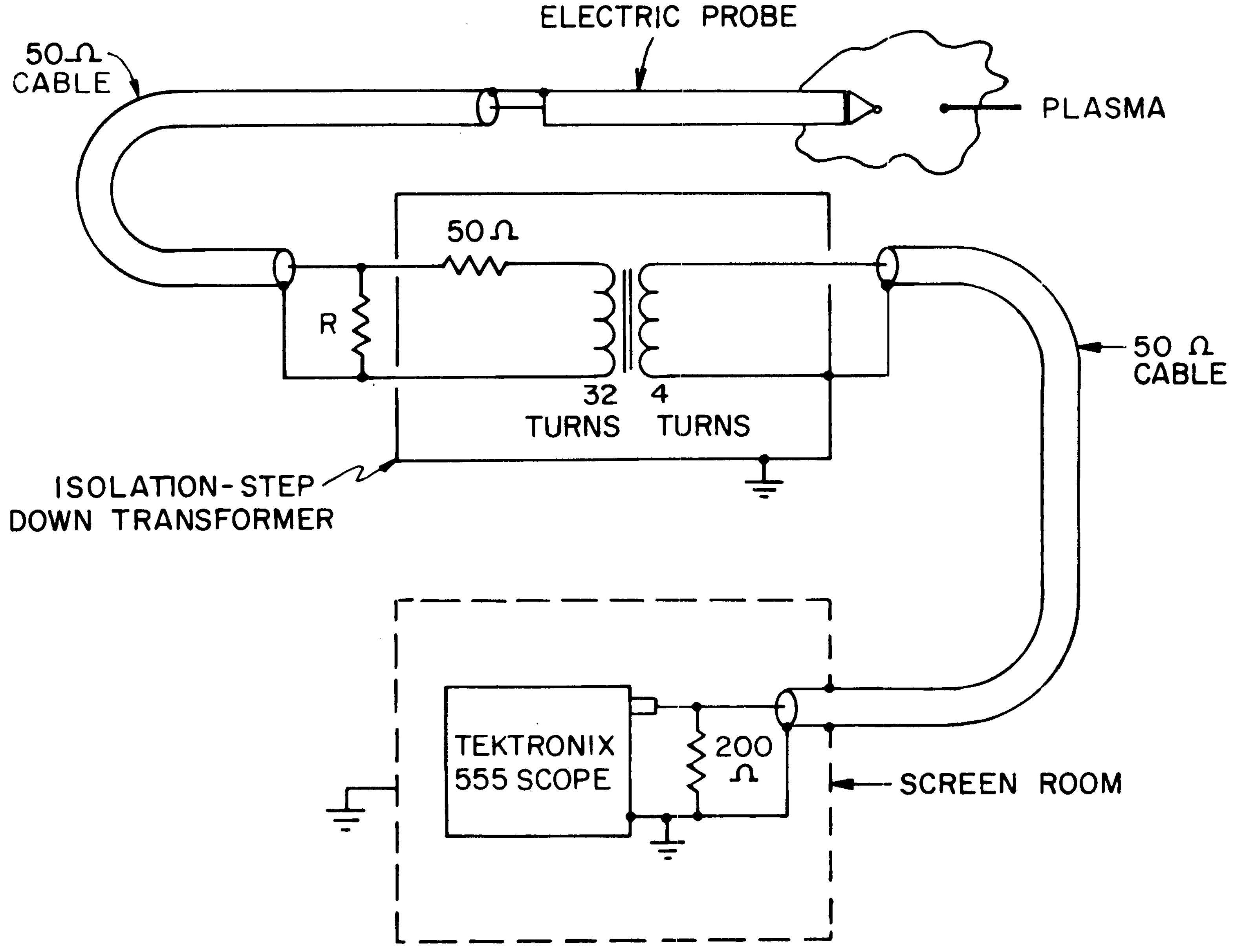

ELECTRIC PROBE CIRCUIT (SCHEMATIC)

FIGURE 8

core is type W-03 ferrite, purchased from the Allen-Bradley Co., and is bolted to an aluminum minibox. An indium gasket between the ferrite and the minibox is added to insure good electrical contact to ground.

The most difficult feature of the electric field experiment is that the transformer must successfully pass the electric probe differential signal, typically 75 volts, and must reject the common mode signal, typically 1500 volts. The probe system was tested for common mode response by shorting the electrodes with conducting silver paint, and observing a signal from the discharge of less than 0.8 volts. This low common mode response was achieved by decreasing the effect of interwinding capacitance three ways: 1) using a ferrite core, with a resistivity of 10^8 times copper; 2) reducing the capacitance between the secondary winding and the ferrite; and 3) increasing the capacitance from each winding to the grounded aluminum box. As was mentioned above, the primary winding could only be spaced far from the ferrite at the sacrifice of good response at high frequencies. During the experiment the transformer sat on the ground plane, adjacent to the screen room.

While the electric probe circuit measures the difference in floating potential between two points in the plasma, the difference in plasma potential is actually the desired experimental measurement. The potential distribution between two floating probe electrodes of an electric probe is shown in

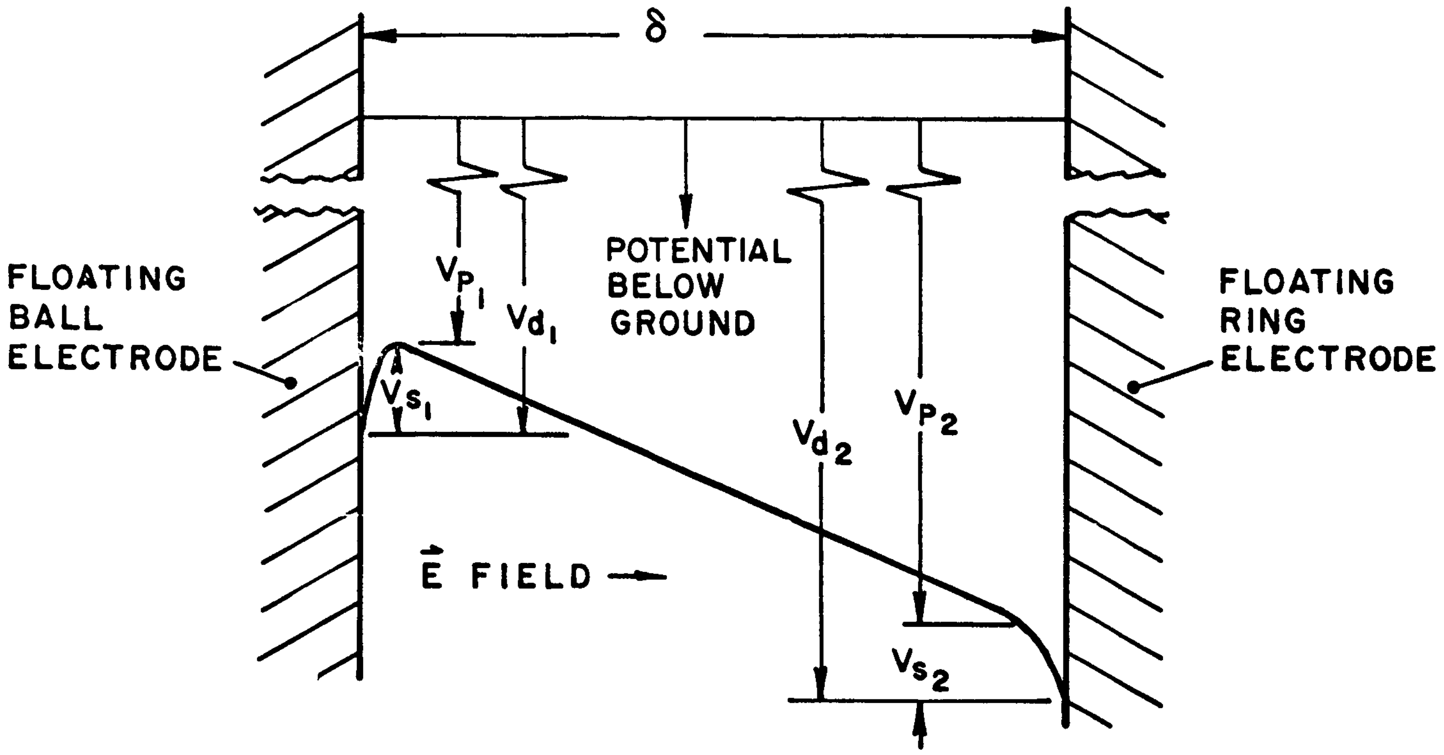

POTENTIAL DISTRIBUTION BETWEEN TWO FLOATING PROBE ELECTRODES

FIGURE 9

Fig. 9. The voltage difference $V_{d_2} - V_{d_1}$, which is measured by the circuit, is equal to the difference in plasma potential between the electrodes, less the difference in sheath voltages on the two electrodes:

$$V_{d_2} - V_{d_1} = (V_{P_2} - V_{P_1}) + (V_{s_2} - V_{s_1}) \tag{1}$$

Thus the sheath drop term must be small if the probe is to respond accurately to plasma potential difference.

Consider a conical floating electric probe tip at zero angle of attack to a streaming, fully ionized plasma, typical of experimental conditions. The plasma electrons are characterized by a temperature of about 5 e.v., and a density

AP25-4135-66

of 10^{22} m^{-3}. The Debye length is 10^{-7} m. The ion density equals the electron density on a scale larger than the Debye length, and the ions have a kinetic energy of 400 e.v., assumed to be large compared to their temperature. One expects, in the absence of ion-ion collisions, that an ion far from the probe moves toward it in a straight line. In the vicinity of the probe tip the ion falls through the potential V_S , but if V_S is small enough compared to the ion kinetic energy, the ion will continue to travel in a straight line until it strikes the probe, and by assumption, is absorbed. Both ions and electrons cross the Debye sheath in times short compared to the time for the current sheath to convect past the probe, and the probe will thus always be in phase with the plasma potential.

This problem of collisionless ion flow over a cone has been defined and investigated by Lam and Greenblatt.(21) They consider only the case of highly negative body potential, so that the electron density is related to density far from the probe by the Boltzmann formula:

$$n_e = n_{e_\infty} \exp(e\Psi/kT_e)$$

where Ψ is the local electrostatic potential. Lam and Greenblatt show that in general the potential drop between the plasma and the body occurs in two regions. A drop V_C occurs in the flow field between infinity and the edge of the Debye sheath, and a further drop V_S occurs across the Debye sheath. If the half angle of the conical probe tip is θ_B ($\theta_B = 35^\circ$ in this case), then a condition for $V_c = 0$ exists between ion kinetic energy, electron temperature, and θ_B :

$$\theta_B \geq \arcsin\left(\frac{m_+ U_+^2}{k T_e}\right)^{-1/2} \equiv \theta_o \qquad (2)$$

In the flow field being measured, θ_o is about 4.4°, less than θ_B , and therefore an ion experiences no potential drop until it enters the Debye sheath.

Rearranging Eq. (2), satisfying the condition $\theta_B > \theta_o$ becomes equivalent to satisfying Bohm's criterion,(22) that ion velocity normal to the sheath exceed the ion-wave speed:

$$U_N = U \sin\theta_B \geq \left(\frac{k T_e}{m_+}\right)^{1/2}$$

Chen has shown(23) that the Bohm criterion guarantees a monotonic variation of potential $V(x)$ across the sheath.

Calculation of the ion-ion mean free path yields a mean free path of 0.3 mm near the probe tip, compared to a typical probe dimension of a millimeter (Fig. 7). An ion may collide a couple of times near the probe, but is deflected a small amount because ion streaming velocity is an order of magnitude larger than ion thermal velocity. Ion-electron collisions are ten times more frequent, but the momentum transferred is negligible. Ion Larmor radius at maximum magnetic field is 2 cm., a value large compared to probe dimensions. To a good approximation, the collisionless assumption and the Lam-Greenblatt theory may be used.

Having established that ion trajectories are straight

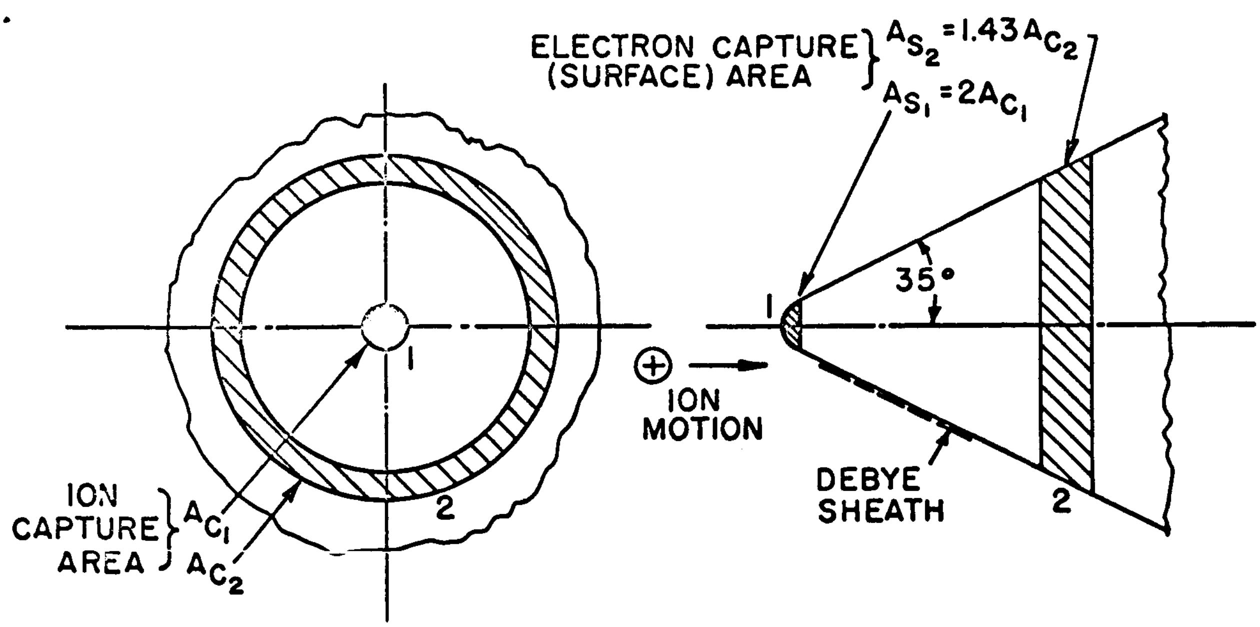

GEOMETRICAL RELATION BETWEEN ION AND ELECTRON CAPTURE AREAS ON ELECTRIC PROBE

FIGURE 10

lines, the ion capture areas for the two probe electrodes are simply related to probe geometry, as shown in Fig. 10. The angle of the hemispherical electrode is greater than at each point on the surface, so that the above results are applicable. The ion capture area for the electrodes is then just their projected frontal area, which for the hemispherical electrode is $A_1 = .07$ mm^2, and for the ring electrode is $A_2 = .92$ mm^2.

The flux of electrons to the probe due to their random thermal motion is determined by their density, temperature, and electrode surface area A_S, which is of course larger than ion capture area, as shown in Fig. 10. Assuming a Maxwellian distribution, the integration over those electrons in the high energy tail of the distribution which have sufficient energy to surmount the unfavorable sheath potential , yields

AP25-4130-66

the electron flux to the electrode of surface area A_S:

$$\phi_e = n_{e_\infty} A_s \left(\frac{kT_e}{2\pi m_e}\right)^{1/2} \exp\left(\frac{eV_s}{kT_e}\right)$$

Electron Larmor radius is on the order of 10^2 times Debye length, so magnetic field is neglected. The flux of singly charged ions is simply:

$$\phi_+ = n_{+_\infty} U A_c$$

The condition of zero net current to the electrode demands the equality of electron and ion flux, and noting that $n_{e_\infty} = n_{+_\infty}$, the sheath potential becomes:

$$V_s = \frac{-kT_e}{e} \ln\left(\frac{\left(\frac{kT_e}{2\pi m_e}\right)^{1/2} A_s}{U A_c}\right) \quad [\text{VOLTS}]$$

The logarithmic term will change very little between the two electrodes, despite changes in T_e and the area ratio. Assuming $A_c/A_s = 0.5$, $U = 5\times10^4$ m/sec, and $T_e = 5$ e.v.:

$$V_s \approx -2.7 \frac{kT_e}{e} \quad [\text{VOLTS}] \qquad (3)$$

The sheath drop is on the order of a few times the electron temperature.

The above derivation of sheath voltage has ignored the effect of magnetic field on the electron flux to the probe. If electrons are restricted to move along $\vec{B}$ lines, perpendicular to the probe axis, then the electrode capture area for electrons is still equal to the surface area. If the electrons are assumed to possess a Maxwellian distribution along the lines, then the electrode averaged normal velocity component of the electron is lower than the zero $\vec{B}$ case, and the sheath drop is slightly reduced. This result increases electric probe accuracy. Derivation of the sheath drop in the case of axial probing yields a result of the same order as for the radial probing just described. The only different consideration is the ion capture area, since ions stream perpendicularly to an axial probe. The effect on the sheath voltage is no more than 15 percent.

Having estimated the magnitude of the sheath voltage, Eq. (1) can now be evaluated to estimate the probe error. Assuming that the plasma potential gradient is constant over the electrode separation δ, substituting Eq. (3) for the sheath voltage:

$$-\nabla V = E \approx \frac{V_{d_2} - V_{d_1}}{\delta} - \frac{2.7k}{e}\,\frac{T_{e_2} - T_{e_1}}{\delta} \quad [\text{VOLTS/m}]$$

The electric field is given accurately by this equation if δ is small compared to a sheet width, and if the second term on the right is negligible when compared with the first. In the center of the sheet where the maximum temperature gradient exists, the electron temperature is no more than several electron volts, and the voltage difference $V_{d_2} - V_{d_1}$ will be 50-80 volts. Thus the error due to temperature gradient is small, and the probe will accurately measure the plasma potential difference. For the probe used in the experiments, δ is 15 percent of the sheet width, and the probe output signal is directly interpreted as an electric field measurement.

The electric probe electrodes conduct zero current in theory, but not in practice. The net current drawn by the isolated probe as a whole is zero, but current does flow between the electrodes and through the impedance R , of amount

$$I_d = \frac{V_{d_2} - V_{d_1}}{R} \qquad [\text{AMPERES}]$$

Since saturation current in the probe circuit is limited by the ion current to the negative electrode, I_d must be small compared to this current, which places a requirement on the impedance R :

$$R > R_{SAT} = \frac{V_{d_2} - V_{d_1}}{e n U A_+}$$

R_{SAT} is the largest when A_- is the tip electrode, which is the case when E_r points radially outward. Then:

$$R_{SAT} \approx 1.3 \qquad [\text{ohms}]$$

For most of the experiments the resistor R (Fig. 8) was 50 ohms, allowing about 30 percent of the maximum theoretical saturation current to flow, and also terminating the probe cable. This value of R was sufficiently large for radial probing, since increasing R did not change the probe output. In axial probing, however, large electric fields exist in the

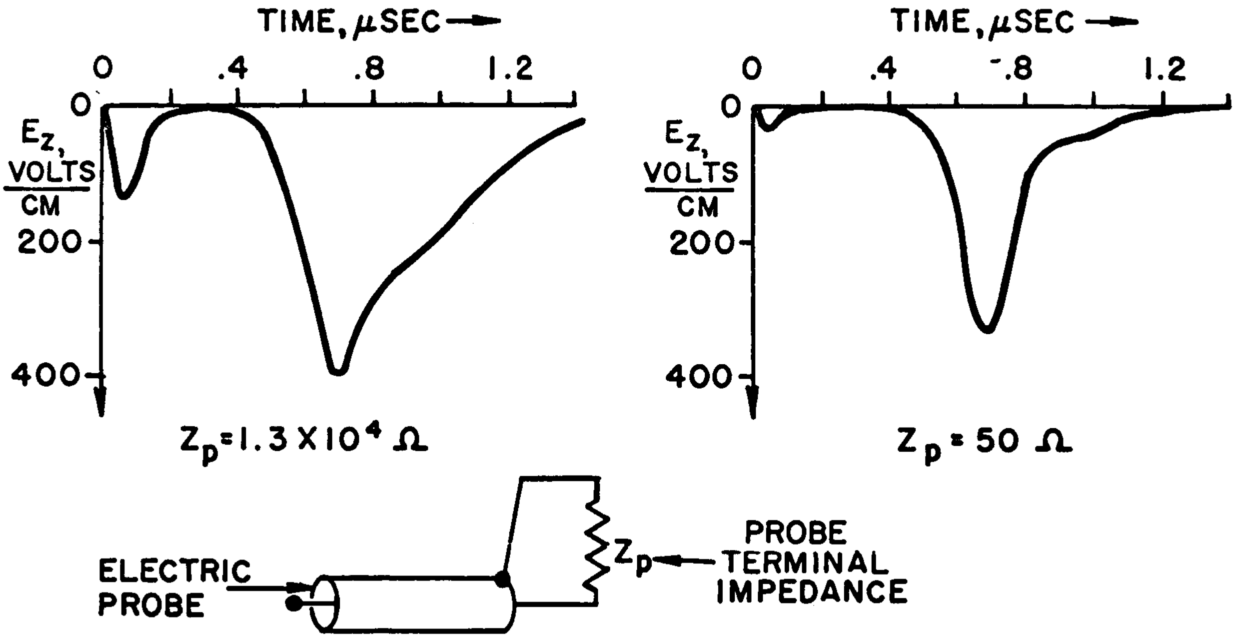

SATURATION OF E_z ELECTRIC PROBE
AT LOW TERMINAL IMPEDANCE, $R/R_0 = .66$

FIGURE 11

region far behind the sheet where electron density is low, and it was found that the 50 Ω resistor allowed saturation current to flow in the probe. This effect is displayed in Fig. 11, showing the signal decaying at times long after the sheet has passed. Thus the resistor R was removed entirely for axial probing, and a current well below the saturation level was driven directly through the transformer primary winding impedance of about 1.3×10^4 ohms. For radial probing, R = 50 Ω was satisfactory behind the sheet, because radial electric field was small.

E. EXTERNAL AND INNER VOLTAGE PROBES

The voltage between ground and a point on the inner electrode was measured with a Tektronix P6013 High-Voltage

AP25-4154-66

Probe. The input resistance of the probe was 10^8 ohms, and the voltage was attenuated by 10^3 times before being displayed. The probe cable passed through a small slot in the screen room door, thence to the 555 oscilloscope. One probe lead was clipped to ground, and the probe tip was connected to a high voltage tap from the cathode.

Two types of voltage taps were used, and were distinguished by their position in the chamber. One type, previously mentioned, extended radially from the edge of the cathode, and out through a 1-3/8" insulated hole in the outer tubular conductor. The voltage measured on this tap with the H-V probe is contributed by the resistive drop in the plasma, plus the changing magnetic flux in the chamber and insulator:

$$V = \frac{d}{dt}\left(\phi_{CHAMBER} + \phi_{INSULATOR}\right) + IR_{PLASMA} \qquad (4)$$

The other voltage tap, called an inner voltage divider, extended axially through the anode at a constant radius, and made contact with the cathode. The inner voltage divider was electrically insulated from the plasma, except at the tip contact point. The voltage measurement by the H-V probe from the inner voltage divider is shown in Fig. 12 at a given time in the chamber. By Faraday's Law, for a closed path fixed in the laboratory:

$$\oint \vec{E}\cdot\vec{dl} = -\frac{\partial\phi}{\partial t} \qquad [\text{VOLTS}]$$

The inner voltage divider carries no current, so the electric field inside it is zero. Also, the electric field inside the

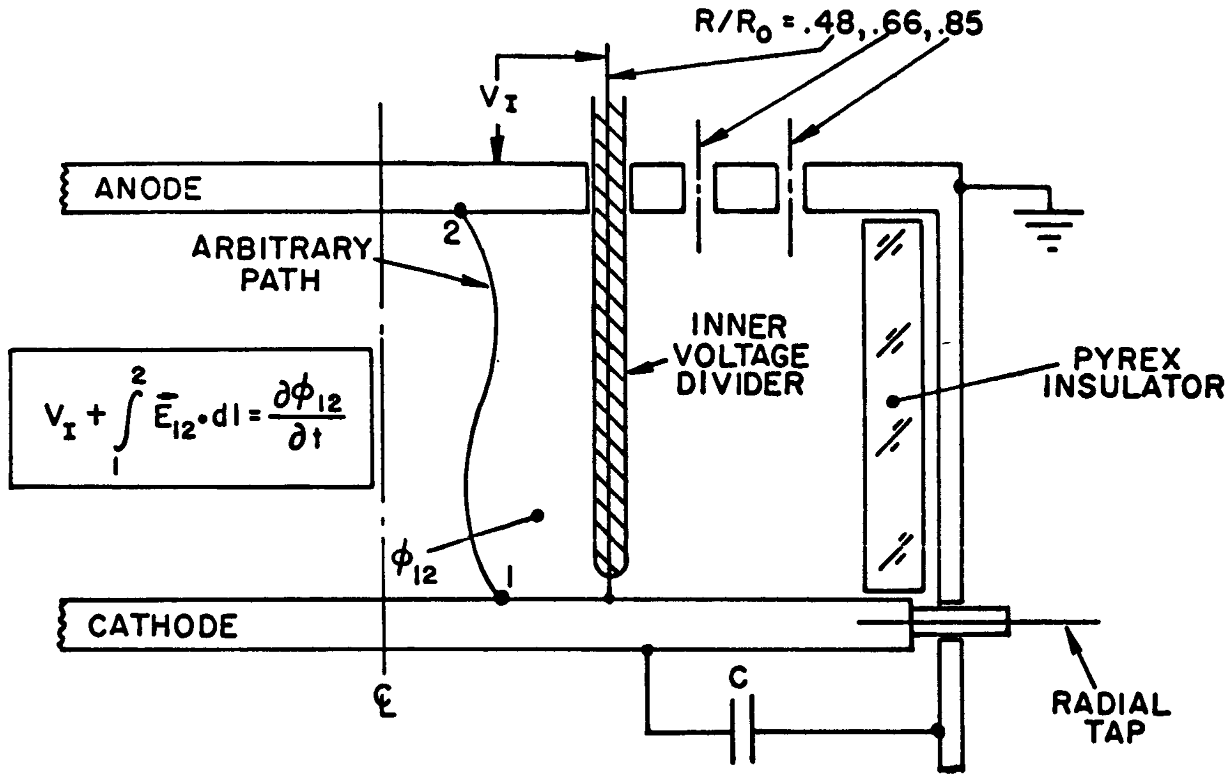

INNER VOLTAGE DIVIDER MEASUREMENT IN THE 5" PINCH CHAMBER

FIGURE 12

high conductivity electrodes is zero. Thus if 1-2 is some arbitrary path from inner to outer electrode, if ϕ_{12} is the flux enclosed between 1-2 and the inner voltage divider, and if V_I is the inner divider voltage below ground, then:

$$V_I + \int_1^2 \vec{E}_{12}\cdot\vec{dl} = -\frac{\partial\phi_{12}}{\partial t}$$

Note that V_I is independent of the choice of path 1-2, so that a relation is defined between E_{12} and ϕ_{12}. Also, if 1-2 is chosen so that ϕ_{12} is zero or constant in time, then:

$$V_I = -\int_1^2 \vec{E}_{12}\cdot\vec{dl}$$

AP25-4/53-66

Thus, where ϕ_{12} is constant the integral from 1 to 2 is independent of the path, and is nonzero because of the resistivity of the plasma:

$$V_I = -\int_1^2 \vec{E}_{12} \cdot \vec{dl} = I R_{PLASMA}$$

Hence plasma resistive voltage drop is determined with the inner voltage divider, ahead of the sheet. Assuming that the plasma resistance remains constant in time, Eq. (4) can be solved for the flux change contribution to the chamber voltage.

F. ROGOWSKI COIL

The Rogowski coil is a double layer of copper wire wound on a toroidal dielectric form as shown below:

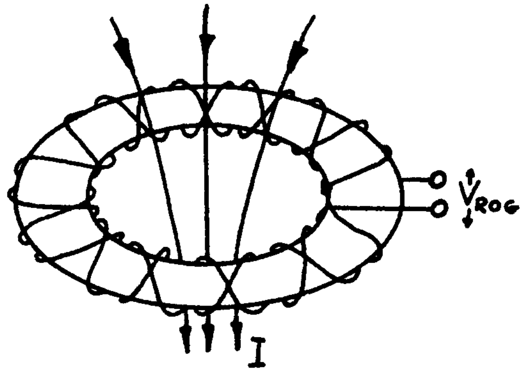

and is designed to respond to the total current, regardless of distribution, passing through the toroid. In this experiment the current was found to be evenly distributed on a cylindrical sheet, making B_θ azimuthally symmetric. From Ampere's Law, for a closed path encircling a current distribution j, the magnetic field $\vec{B}$ is related to current by:

$$\oint \vec{B} \cdot \vec{dl} = \mu_0 \int_S \vec{J} \cdot \hat{n} \, dA = \mu_0 I \qquad \text{[mks]}$$

The line integral thus depends only on total current I, and for a circular path enclosing I, of diameter D :

$$\oint \vec{B} \cdot \vec{dl} = \pi D B_\theta = \mu_0 I$$

The voltage generated in the Rogowski coil is the number of turns times the rate of change of flux in one turn:

$$V_{ROG} = n A \frac{\partial \overline{B_\theta}}{\partial t} = \frac{\mu_0 n A}{\pi D} \frac{\partial I}{\partial t}$$

where $\overline{B_\theta} A$ equals flux in the coil.

This voltage is integrated by RC network, yielding a signal proportional to the enclosed current:

$$\int V_{ROG} \, dt = \frac{\mu_0 n A}{\pi D} I \qquad \text{[volt-sec]}$$

The Rogowski coil in the 5" pinch is about 14 cm in diameter, and has 16 turns wound on a 2 mm^2 form. The unintegrated voltage is about 100 volts, and the coil must be well insulated to prevent arcing.

The current flow in the 5" pinch was cylindrically symmetric, enabling the current waveform to be conveniently displayed by a single B_θ probe coil placed in the chamber insulator.

The Rogowski coil was calibrated by discharging the capacitor bank through a resistor, and equating the time integral of the integrated Rogowski coil voltage, multiplied by a calibration factor, to the known charge on the bank. The resistor was made of .001" stainless steel shim stock, and produced enough damping to eliminate ringing of the current. The resistor was destroyed by heating after five shots.

G. KERR CELL PHOTOGRAPHY

Kerr Cell photographs of the discharge were taken on a Crown Graphic 4"x5" recording camera, equipped with a Polaroid back. A Kerr Cell type shutter, made by Electro Optical Systems, Inc. exposed the Polaroid film for .05 microseconds, sufficiently stopping the plasma motion. Radial view photographs of the discharge were taken through the open end of a special horseshoe-shaped conductor (Fig. 13), which permitted viewing of the entire chamber. An aluminum screen was placed in the optical path to reduce the effect of radial leakage of magnetic field, but no quantitative change in the discharge, due to preventing this leakage, was observed.

H. DISCHARGE SPECTRUM MEASUREMENTS

To estimate the amount of ionization and the electron temperature in the chamber, spectrograms of the discharge were taken with a Bausch and Lomb 1.5 Meter Spectrograph,

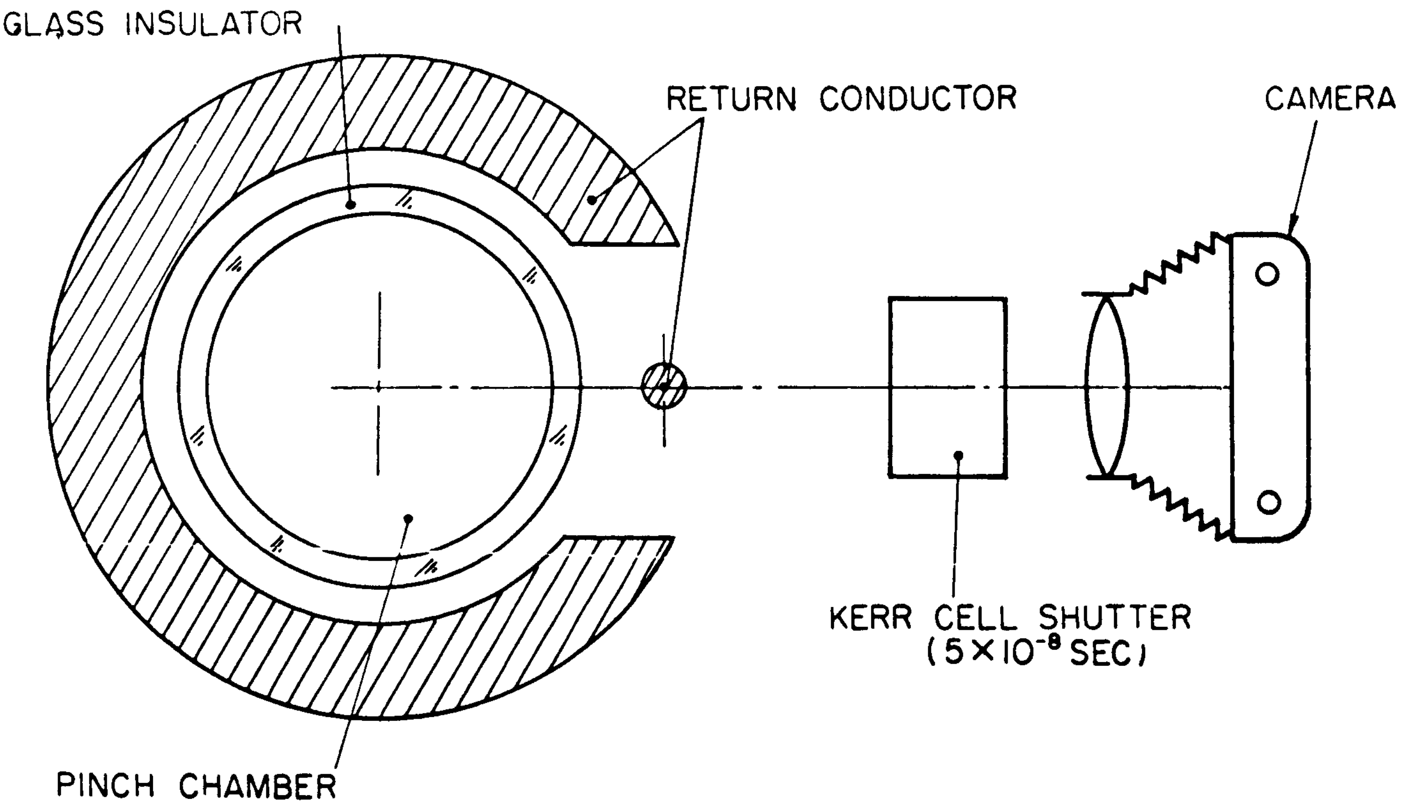

APPARATUS FOR SIDE VIEW PHOTOGRAPHS

FIGURE 13

equipped with 10, 30, and 60 μ slits, and providing a dispersion of 16 Å/mm in the first order. The discharge was viewed through a radial slit in the anode of the 5" pinch, extending from the insulator to the discharge center. A small lens focused the anode slit onto the spectrograph slit. An argon reference spectrum from a Geissler tube was taken before each exposure, made on Royal X Pan film. The spectrograms were not time resolved.

AP25-4149-66

Chapter III

EXPERIMENTS, DATA, AND RESULTS

A. TOTAL CURRENT AND VOLTAGE IN THE CHAMBER

The bulk of the experiments were performed in the 5" pinch chamber with argon test gas at 120 μ Hg, and a capacitor bank voltage of 10,000 V. It was previously observed(27) that a pressure of 120 μ Hg in argon gave a reproducible discharge, desirable for shot-by-shot surveys. In the 5" pinch, furthermore, preliminary $\dot{B}$ probe studies indicated that self-induced magnetic fields acted on the current sheet all the way to the chamber center, and streak photographs showed that the sheet propagated inward at nearly constant velocity. Finally, the sheet trajectory agreed well with that predicted by the snowplow model, indicating that the current sheet was sweeping up and accelerating most of the argon into which it propagated.

The total circuit current, as measured by a calibrated integrated Rogowski coil signal, closely resembles a damped sinusoid (Fig. 14). Deviation from the damped sinusoid waveform is caused by the pinching current sheet, which increases chamber inductance. Times at which magnetic and electric field distributions are calculated are indicated by circles on the waveform. The maximum current rise rate is 1.1×10^{12} amp sec^{-1}, and a maximum of 3×10^{5} amperes flow in the circuit at 0.44 μsec after chamber breakdown. The current then decreases nearly linearly,

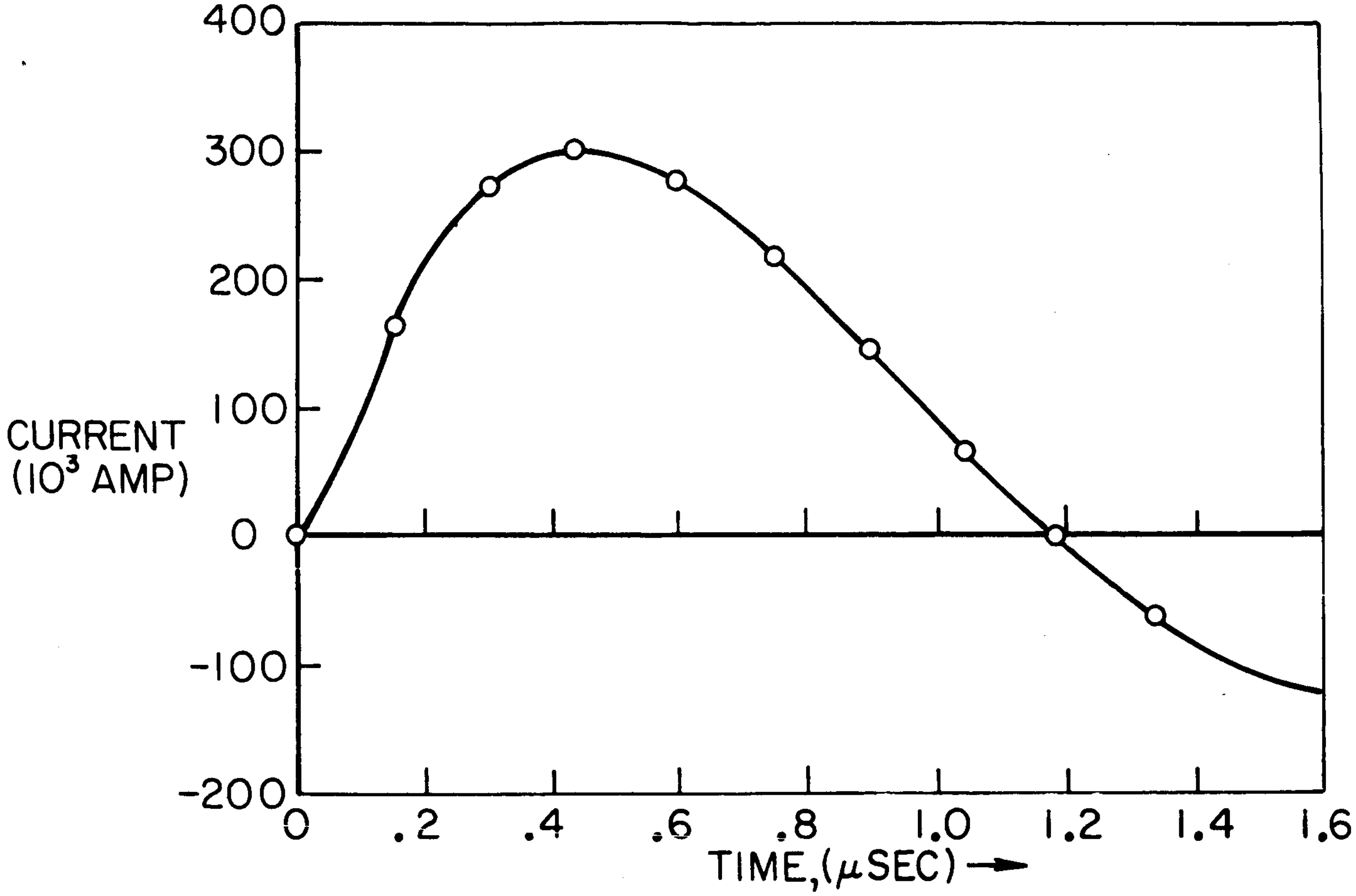

TOTAL CURRENT BETWEEN ELECTRODES
5" CHAMBER, 10 KV, 120μ ARGON

FIG. 14

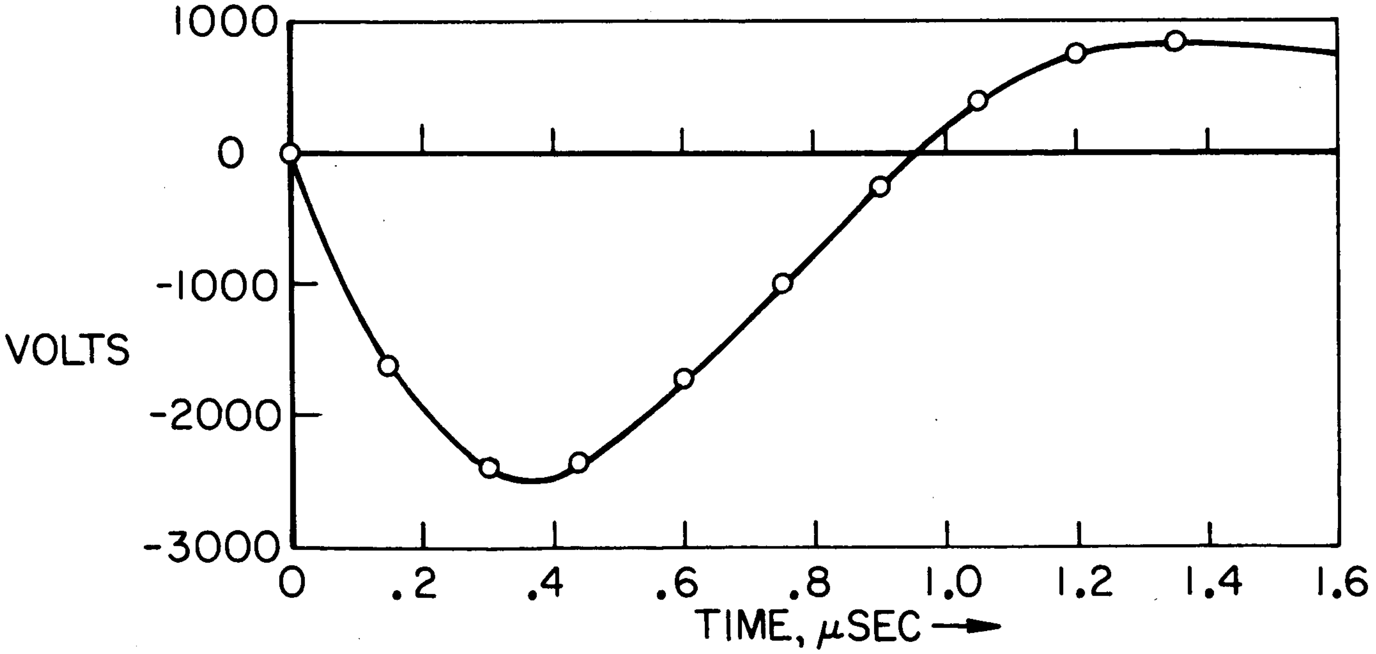

VOLTAGE BETWEEN ELECTRODES, R/Ro=1.0
5" CHAMBER, 10 KV, 120μ ARGON

FIG. 15

AP25-4142-66

falling to zero at 1.20 μsec. At this time, the leading edge of the current sheet has propagated to the center of the chamber. Finally, the diameter of the luminous column reaches a minimum at 1.60 μsec.

Voltage between the chamber electrodes is measured with a radial voltage tap to the cathode, corrected for the voltage contributed by changing flux in the insulator (Fig. 15):

$$V_{\text{chamber}} = V_{\text{probe}} - \frac{\partial I}{\partial t} L_{\text{insulator}}$$

where the insulator inductance is 1.6×10^{-9} henries. As discussed in Chapter II, the line integral of electric field between the electrodes depends on the electric field induced by the magnetic field, and hence, on the path taken for the line integral. Thus, inter-electrode voltage is a function of radius for paths parallel to the chamber axis. The chamber voltage is defined as the voltage at a radius $R/R_0 = 1.0$; i.e. a path adjacent to the insulator.

The chamber voltage reaches a maximum of -2500 V at 0.37 μsec, prior to the maximum in total current. Voltage then falls to zero at .95 μsec, finally reaching +850 V at pinch time. Noise on the traces in the first .1 μsec precluded any voltage measurements during the highly resistive breakdown phase, as voltage decreases rapidly from -10,000 V to an intermediate value as conductivity increases in the plasma.

Power input to the chamber, or total circuit current times chamber voltage, is shown in Fig. 16. Maximum input power is

AP25-4/48-66

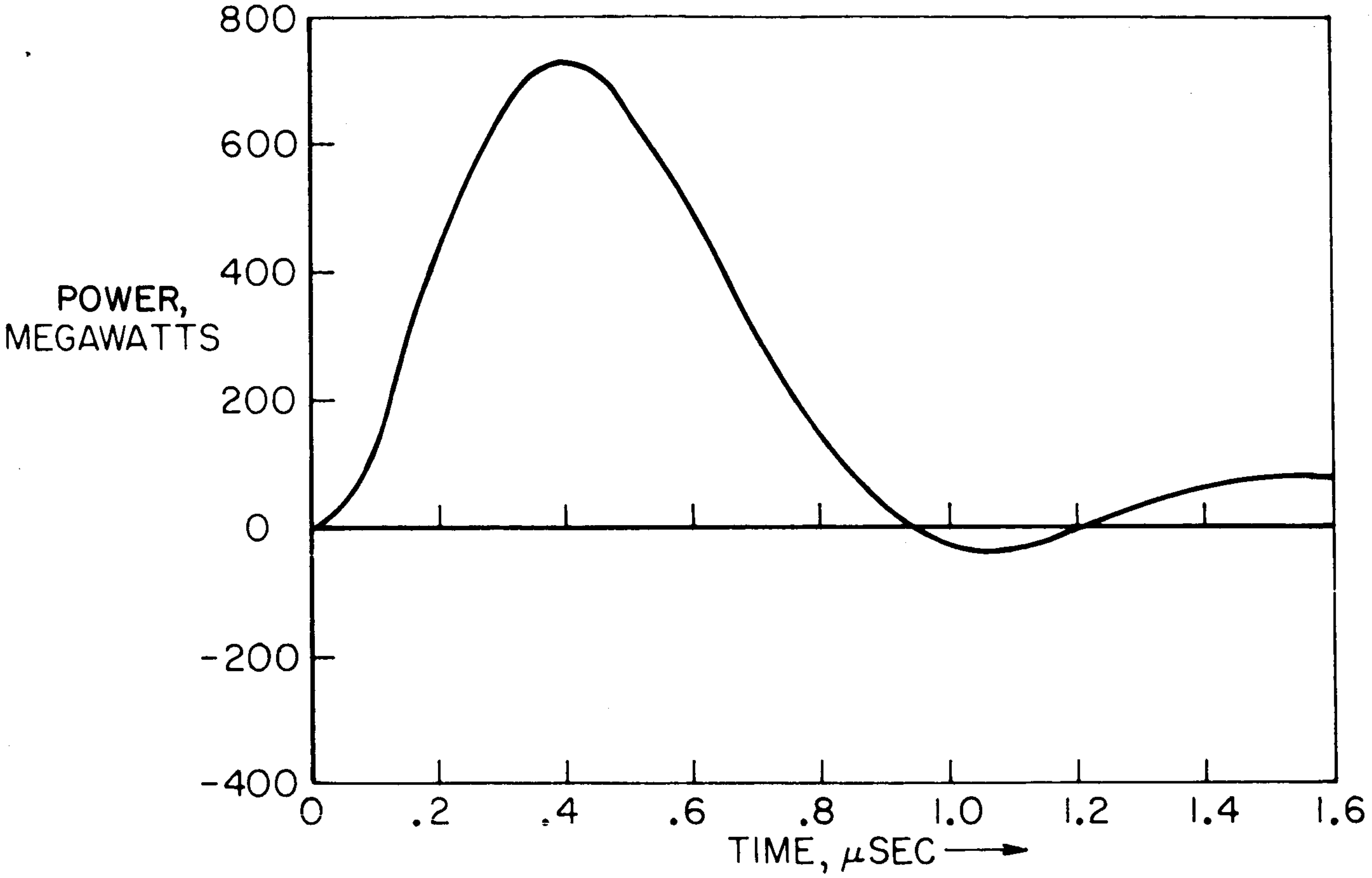

5" CHAMBER INPUT POWER
10 KV, 120μ ARGON

FIG.16

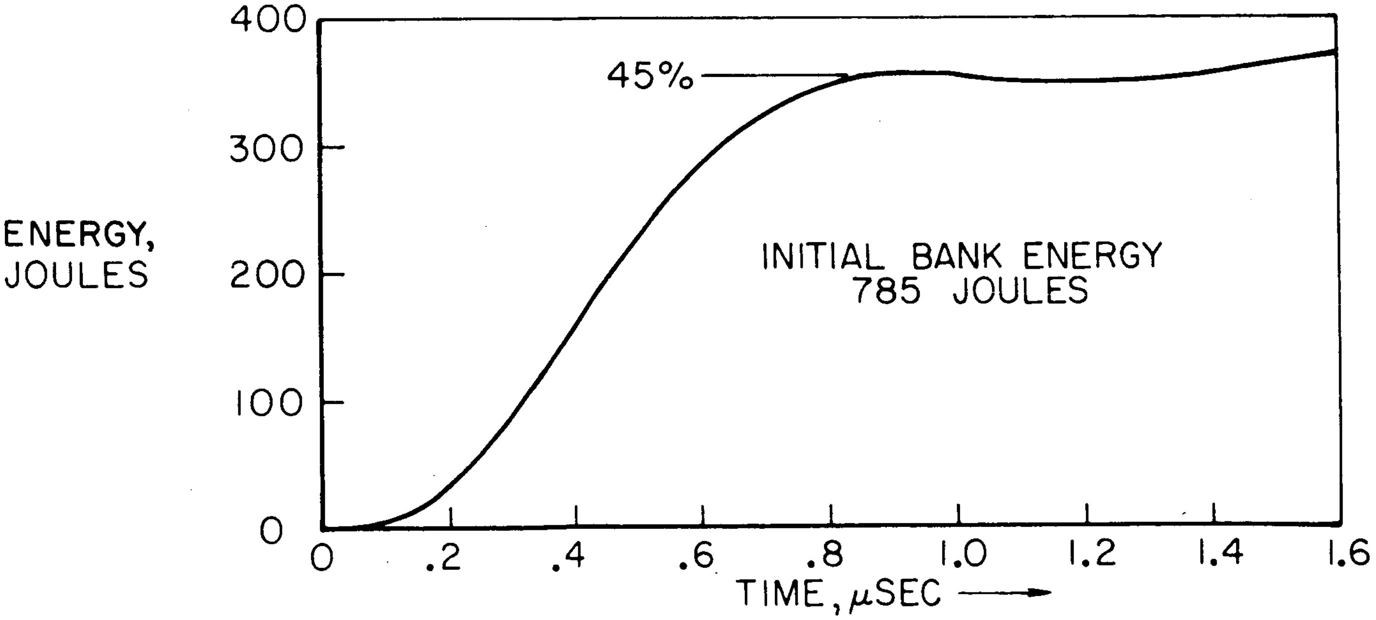

5" CHAMBER INPUT ENERGY
10 KV, 120μ ARGON

FIG. 17

730 megawatts at 0.4 usec. Power flows out of the chamber from .95 to 1.20 μsec, between which times the chamber voltage has reversed but the current has not, and power then flows into the chamber at a low level at later times.

The energy input to the chamber, or the integrated power input, reaches 45 percent of the capacitor bank energy at .95 μsec, and exceeds 50 percent as the current damps out to zero (Fig. 17). Assuming that the remaining 50 percent of the energy is lost in I^2R heating outside the chamber, the average external circuit resistance for the complete current ringdown can be calculated:

$$\bar{R} = 6.7\text{x}10^{-3} \quad [\text{OHMS}]$$

This resistance is only 22 percent higher than the circuit resistance predicted by the snowplow model (Appendix A).

All of the above circuit measurements of current, voltage, power, and energy agree well with the snowplow model discussed in Appendix A.

B. KERR CELL PHOTOGRAPHY

Photographs taken with the Kerr Cell, viewing radially into the chamber (Fig. 18), show that a cylindrical luminous front, moving at constant velocity, pinches to an intense plasma column at the chamber center. During the dynamic phase of the pinch this luminous front can be described as five distinct regions, depending on axial and radial position.

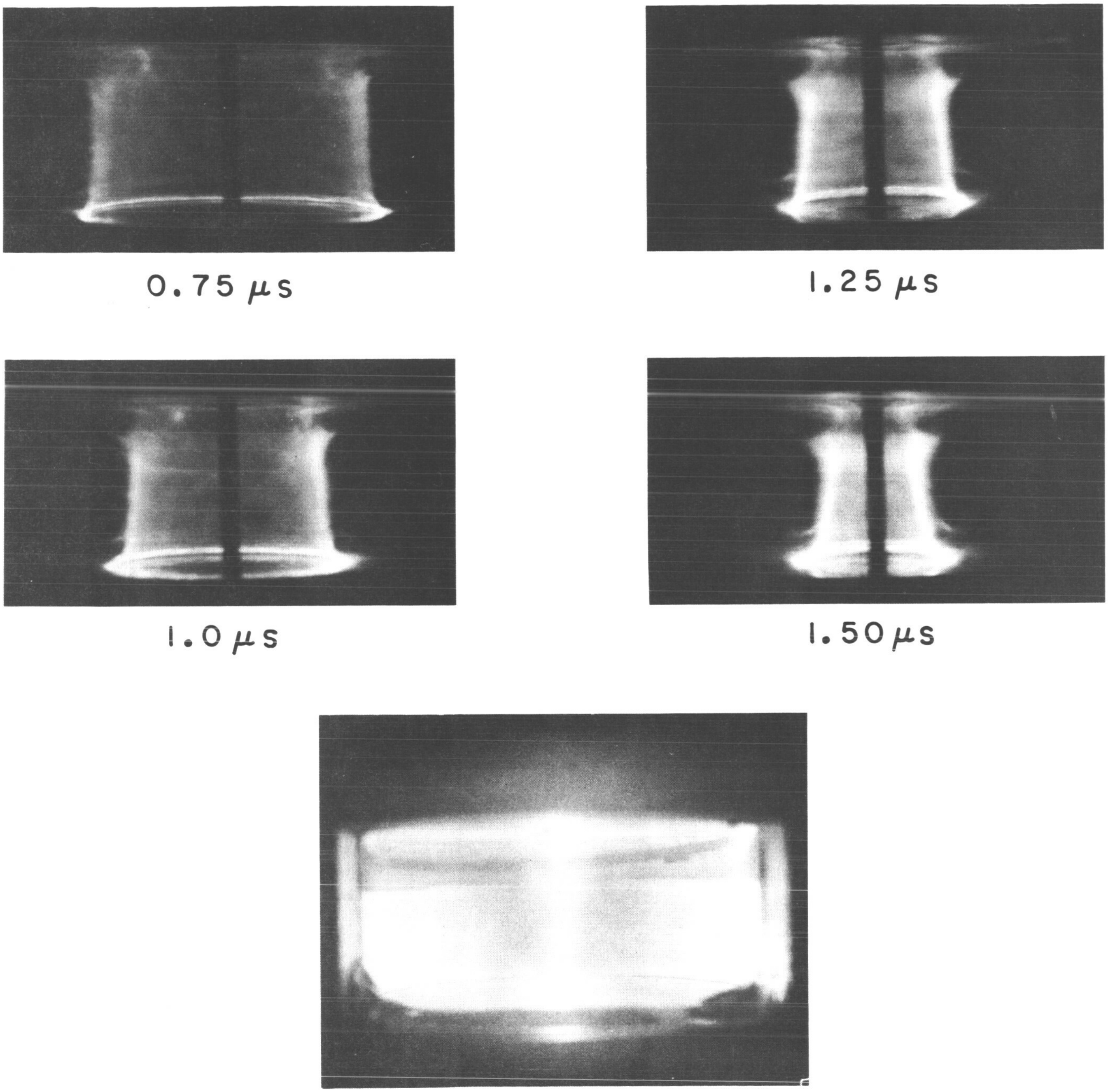

0.75 μs

1.25 μs

1.0 μs

1.50 μs

1.8 μs

SIDE VIEW OF DISCHARGE IN 120μ ARGON

5" TUBULAR APPARATUS
PERIOD: 2.65 μs
TOP ELECTRODE: ANODE

AF25-P27-65

FIGURE 18

Referring to Fig. 18, a "foot" exists along the anode (top electrode in the photographs) in which the luminosity and current distribution are more diffuse than in the main part of the sheet. The radial position of the foot at the point of anode attachment is ahead of the main sheet, as is shown by measured trajectories (Fig. 19). However, the measured trajectories show that the velocity of the main sheet equals or slightly exceeds the velocity of the anode foot attachment point. This observation is consistent with magnetic probe measurements, which show that a lower radial force density exists along the anode than in the main sheet.

A dark toroidal region in the anode foot appears at the same radius as the main sheet. This anode dark region is bounded on the outside by a faintly luminous sheet, which appears as a pair of hooks, curving outward from the main sheet and upward toward the anode. The axial height of the dark region grows with time (Fig. 20), and approaches 1.5 cm just before pinch. No corresponding pattern was found in the current density which would explain the dark region.

The photographs at 1.25 and 1.50 μsec show a luminous cylindrical band, axially adjacent to the anode dark region. The hook patterns emanate from this luminous band, which is 1 cm wide, measured in the axial direction. In the 1.80 μsec photograph the bolt has been removed to expose the pinch column on the axis.

A uniform, thin, highly intense front exists in the

AP25-4155-66

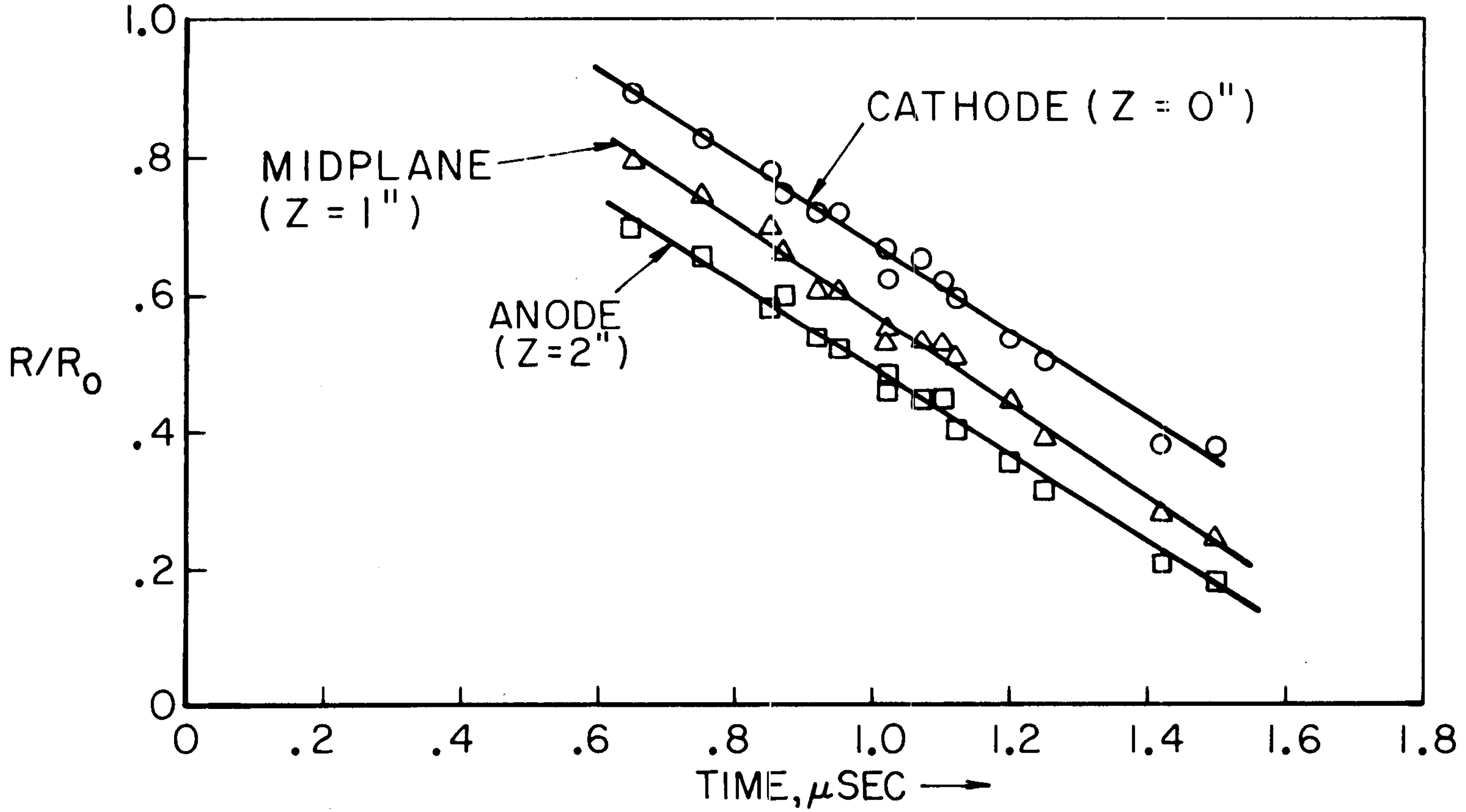

LUMINOUS FRONT TRAJECTORIES FROM RADIAL VIEW KERR CELL PHOTOGRAPHS
120μ ARGON, 10 KV

FIGURE 19

AP25-4156-66

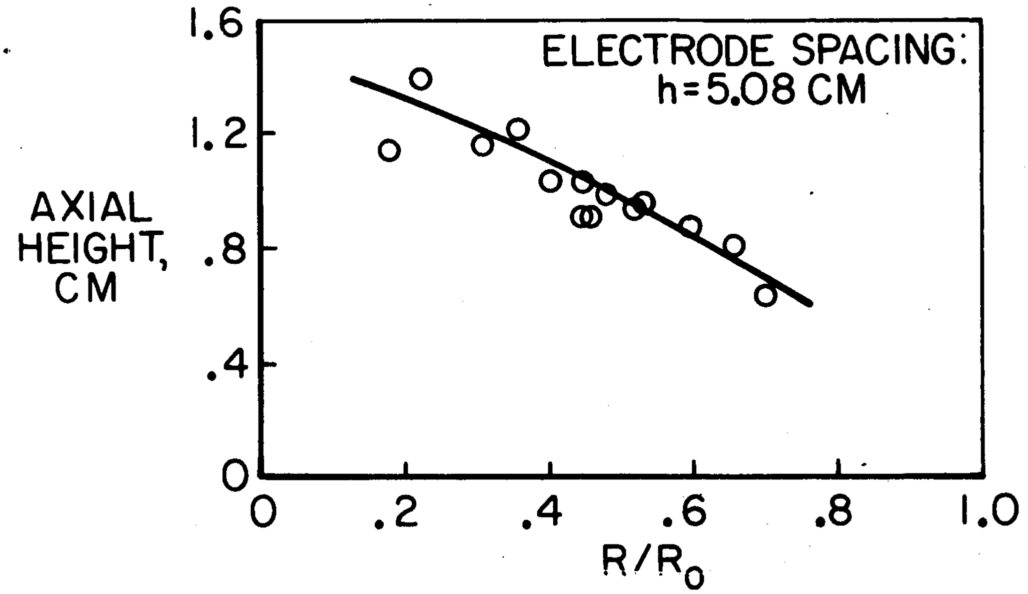

AXIAL HEIGHT OF ANODE DARK REGION
120μ ARGON, 10 KV

FIGURE 20

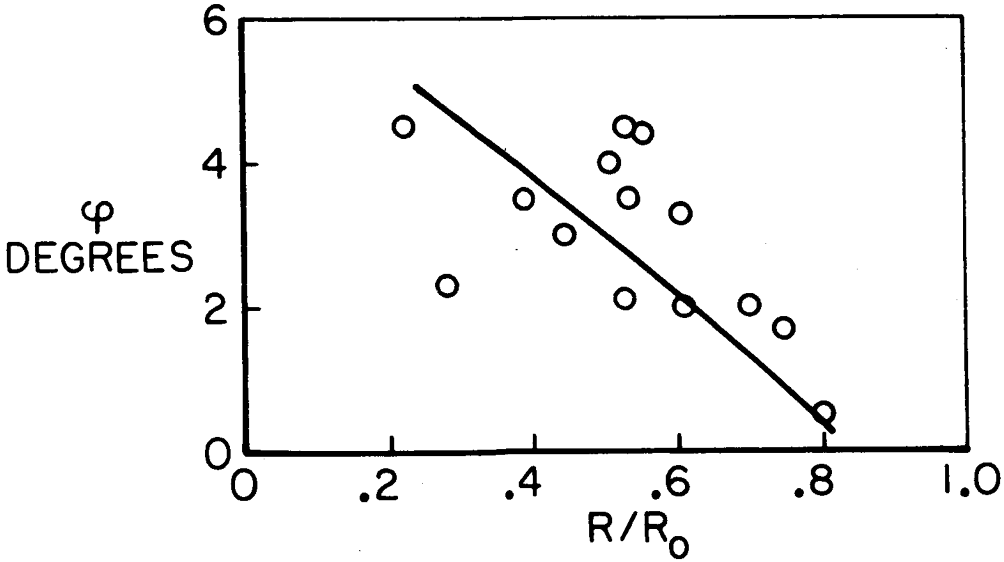

TILT ANGLE OF CURRENT SHEET
120μ ARGON, 10 KV, Z/h = 0.5

FIGURE 21

midplane region of the discharge, and coincides with the peak in current density. A magnetic probe placed in the discharge responds with a $\dot{B}_\theta$ peak at the time that the luminous sheet passes the probe coil, which is visible in the photograph (Fig. 22). The velocity of the luminous sheet is 4.3×10^4 m/sec, constant from $R/R_0 = 0.8$ to $R/R_0 = 0.2$.

The luminous sheet tilts slightly toward the anode at a small angle to the chamber axis. The tilt angle φ is near zero at a large radius, and approaches 6° near the axis of the chamber (Fig. 21). The increase in φ with time is possibly indicative of a "sausage" instability in the current sheet, but φ was so small that it was less accurately measurable with B probes than with the Kerr Cell photographs.

A foot exists on the cathode, trailing behind the main current sheet, but convecting at the same velocity (Fig. 19). The cathode attachment point is highly luminous, unlike the anode attachment, but the current density distribution in the cathode foot is diffuse, as is the case with the anode current. The axial height of the cathode foot increases with time, becoming about 4 mm near the axis of the discharge.

Two small pips are visible in Fig. 18, protruding radially outward from the discharge about 8 mm from the cathode. These pips belong to a luminous ring, which is faintly visible behind the discharge on the left side of the 0.75 μsec photograph. The ring has not been detected by other means, and remains unexplained.

AP25 P39 66

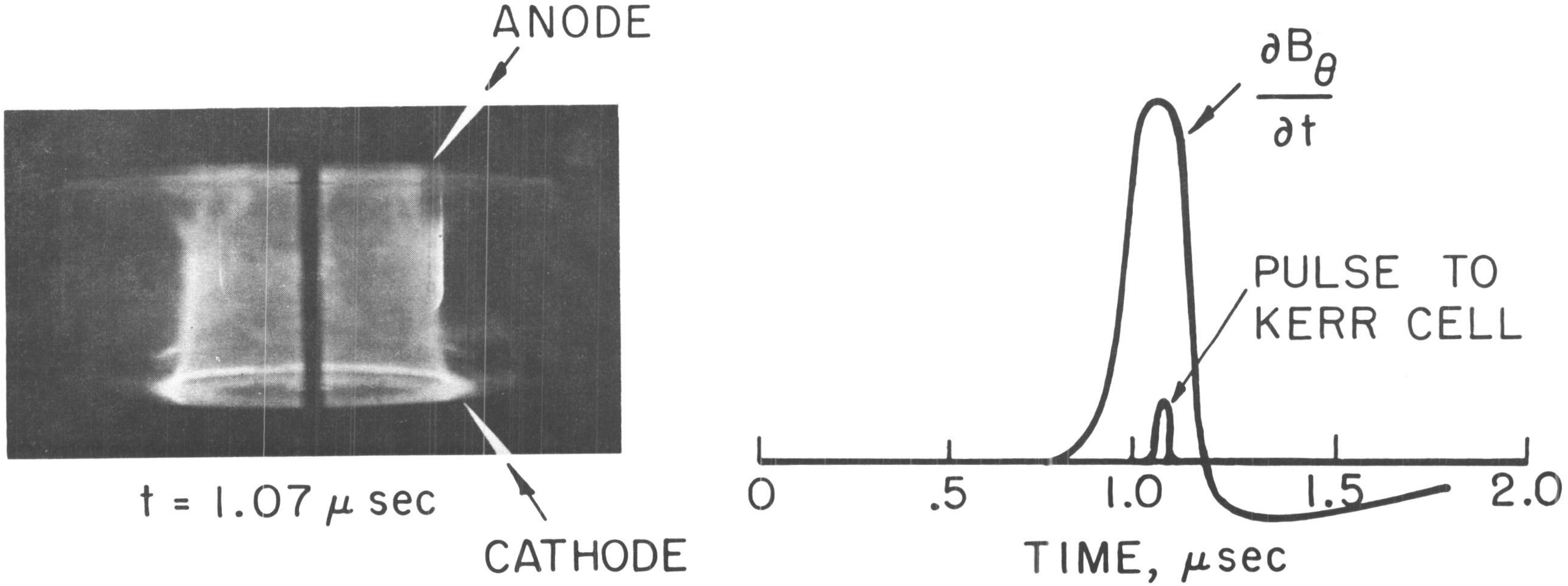

RELATIVE POSITION OF LUMINOUS FRONT AND MAGNETIC FIELD

5" CHAMBER, 120μ ARGON, 10KV

FIGURE 22

C. SPECTRUM OF THE DISCHARGE AND ESTIMATE OF ELECTRON TEMPERATURE

The spectrum of the discharge was photographed through a spectrometer between wavelengths 3250 and 6400 Å (Fig. 23). The lines which are bright at all chamber radii are radiated by the excited neutrals and singly and doubly charged ions of argon, carbon, and aluminum. Quite broad Balmer H_β and H_γ lines are present, and lines from AIII are visible at the center of the discharge. Continuum radiation is also brightest at the chamber axis.

On the basis of this spectral data the electron temperature in the plasma must at least be several electron volts. An analysis by Petschek and Byron showed that the ionization of atoms by low temperature electrons is a multistep process, in which an atom or ion is first raised to the first excitation level by electron collision, then is ionized by another or perhaps several, collisions.$^{(29)}$ The time to raise an average neutral argon atom to excitation by electron collision has been computed as a function of T_e (Appendix C), yielding the equation:

$$t_{ex} = \frac{2.14 \times 10^{15} \exp(\chi/T_e)}{n_e \sqrt{T_e}\,(\chi + 2T_e)} \quad [\mathrm{sec}] \qquad (5)$$

where n_e is in m^{-3}, T_e is in e.v., and for argon neutrals, $\chi = 11.5$ e.v. For the case where $n_e = 10^{22}\ m^{-3}$, Fig. 24 shows that electron temperature must exceed a couple of electron volts if most of the atoms are to be excited during the time of the experiment, on the order of a microsecond. The uniformity of

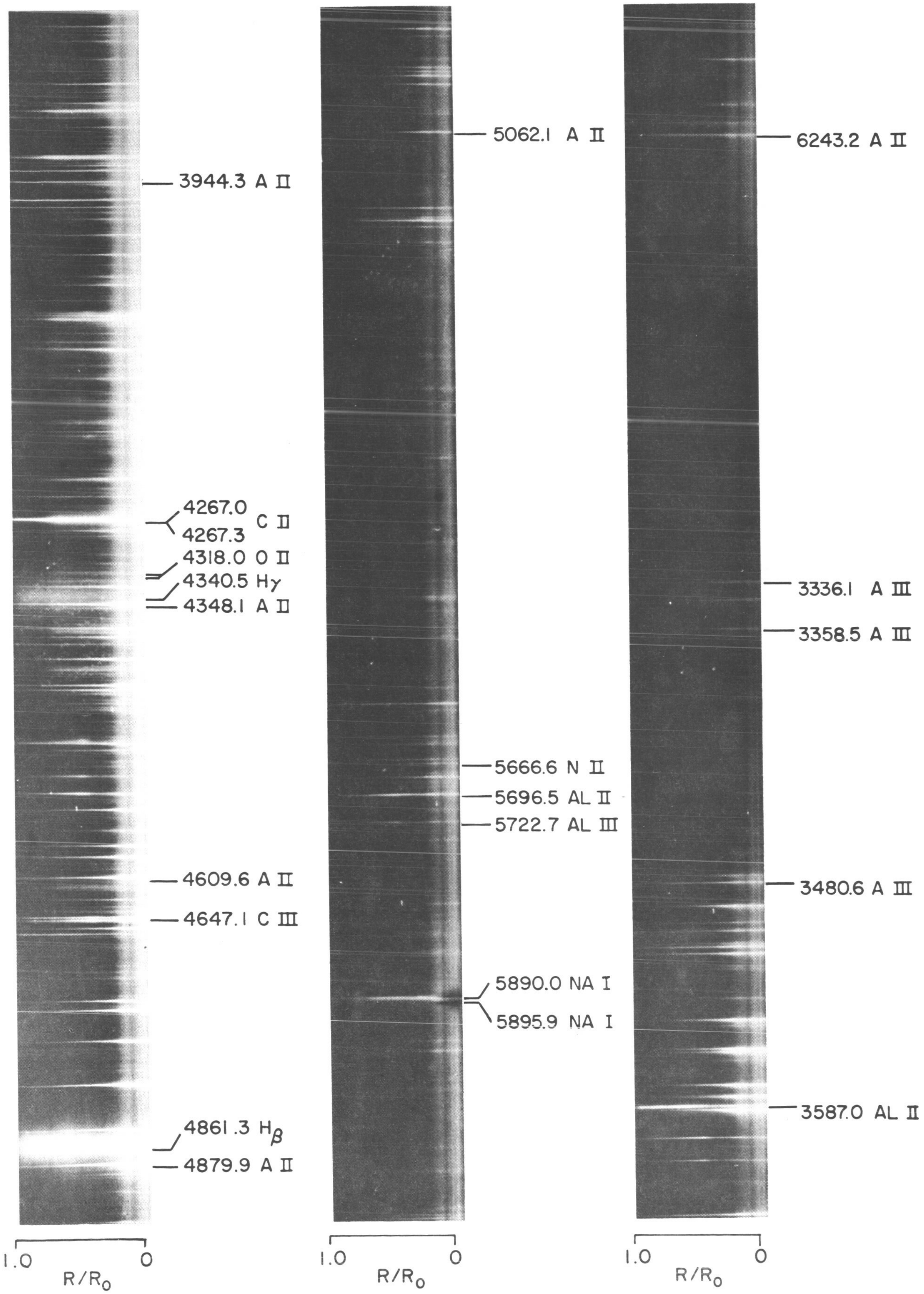

AP25-P528-66

SPECTRUM OF DISCHARGE IN ARGON
5" PINCH, 120μ ARGON, 10 KV, 32μ SLIT

FIGURE 23

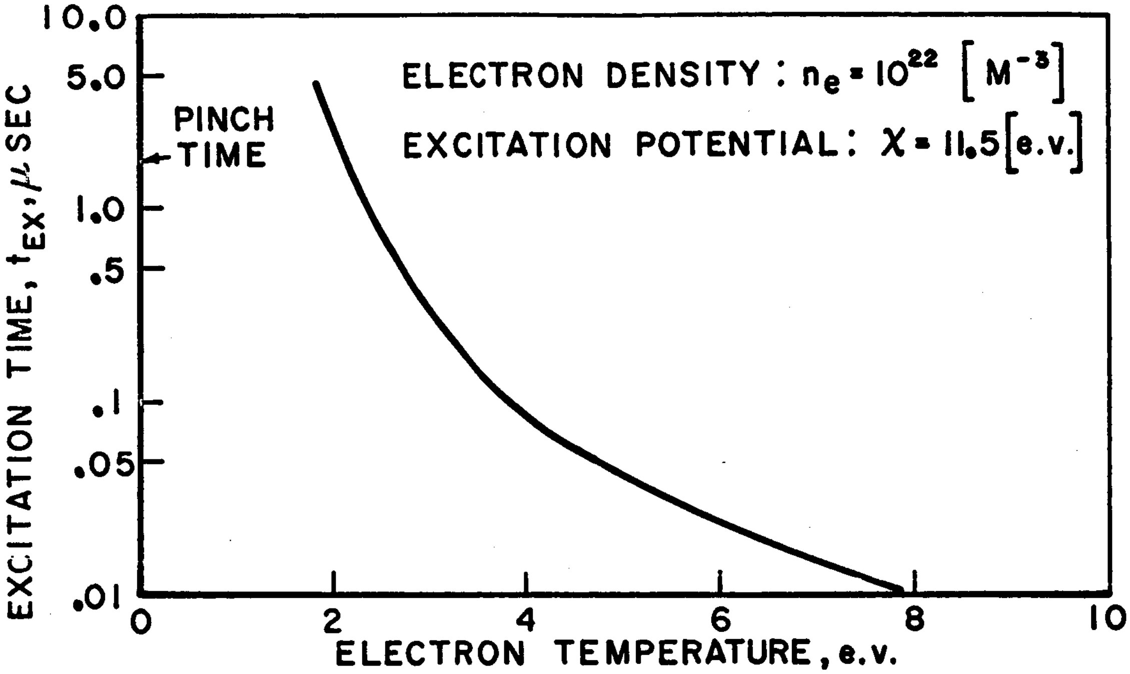

AVERAGE TIME t_{EX} TO EXCITE NEUTRAL ARGON BY ELECTRON COLLISION

FIGURE 24

the spectral lines in Fig. 23 perhaps indicates that the time to excite is less than the transit time for a heavy particle through the sheet, which in turn implies an electron temperature of 4 e.v. or larger.

An upper bound on the electron temperature may be estimated by constructing a model for the electron energy balance. The electron swarm will receive energy primarily from ohmic heating, and to a lesser extent, from any more energetic ions. The primary energy loss mechanisms are radiation, heat conduction, and inelastic ion collisions.

The power loss to radiation can at best be estimated, after looking at the spectra, as at most a few percent of

AP25-4137-66

black body radiation. Thus:

$$P_R \ll 2\pi r h \sigma T_e^4 \qquad \text{[watts]}$$

where σ is Stefan's constant: $\sigma = 5.7\text{x}10^{-8}$ watts/m^2 $^{\circ}$K^4. For a sheet at radius $r = .03$ m, and expressing T_e in e.v.:

$$P_R \ll T^4_{e\,[e.v.]} \times 10^7 \qquad \text{[watts]}$$

For T_e equal to several electron volts, the total radiation is small compared to 10^9 watts. Because the lines are far apart in the spectrum, and are relatively narrow, the radiation power loss is probably not higher than 10^7 watts, an amount small compared to the ohmic heating.

The heat lost by conduction from the center of the sheet may be estimated very roughly:

$$\frac{d}{dr}\left(\mathcal{K}\frac{dT}{dr}\right) \approx \mathcal{K}_{rr}\frac{T_e}{L^2} \qquad \text{[watts/m}^3\text{]}$$

where L is a characteristic length, the sheet width, and $\mathcal{K}_{rr}$ is the component of the heat conductivity tensor (Ref. 30):

$$\mathcal{K}_{rr} \approx 0.6\,\frac{T^{5/2}_{e\,[e.v.]}}{1+\Omega^2}$$

where Ω is the ratio of cyclotron frequency to collision frequency, called the Hall parameter, and the cutoff parameter

$\ln \Lambda$ has been taken as 6. For a 5 mm thick sheet:

$$\frac{d}{dr}\left(\mathcal{K}_{rr}\frac{dT}{dr}\right) \approx 3\times10^{8}\,\frac{T_{e\,[\text{e.v.}]}^{7/2}}{1+\Omega^{2}} \qquad [\text{watts/m}^3]$$

For T_e = 4 e.v. in the center of the sheet and a volume of 10^{-4} m^3, Ω is larger than unity in the current sheet, and the heat lost is less than 10^6 watts, again small compared to ohmic heating. At the front edge of the sheet however, ohmic heating is small, Ω is small, and heat conduction can effectively smooth out the temperature gradients.

The power loss by inelastic collisions with the neutrals may be calculated from Eq. (5), assuming that in each collision with an argon neutral the electron loses the excitation energy, χ :

$$P_e = n_e \chi\, t_{ex}^{-1} \qquad [\text{watts/m}^3]$$

Taking n_e = 10^{22} m^{-3}, excitation energy χ = 11.5 e.v., a plasma volume V = 10^{-4} m^3, and the previously calculated t_{ex} (Fig. 24), the net power lost by the electrons, $P_e V$, is calculated below for several values of T_e :

T_e , e.v.	$P_e V$, megawatts
3	5.2
5	45
7	115
9	234

Since the total energy transfer rate to the electrons is estimated to be about 100 megawatts (Chap. IV), the electron temperature is therefore probably 6 e.v. or lower.

Summarizing the proposed model of electron temperature, at the front edge of the sheet ohmic heating is small and heat conduction is efficient, so that the electron temperature will be spatially uniform, and on the order of an electron volt. In the center of the sheet ohmic heating is large, and heat conduction is low, so that the temperature adjusts to the rate at which ohmic heating balances the power loss by inelastic collisions. The center of the sheet radiates more strongly than other regions, because of the high temperature and density. At the back end of the sheet ohmic heating is again small, and the electron temperature decreases. Behind the sheet the electrons begin to equilibrate with the ions, although this is a slow process, requiring thousands of collisions.

D. INNER VOLTAGE DIVIDER MEASUREMENTS

The inner voltage divider was inserted axially across the chamber at radii $R/R_0 = .85$, .66, and .48, and voltage was measured with the high voltage probe. Figure 25 shows the rapid voltage rise as the current sheet passes the inner voltage divider at $R/R_0 = .66$ and .48. The lower trace in each oscillogram is total circuit current measured by the Rogowski coil, and provides a time correlation.

Once the resistive breakdown phase of the discharge is complete, the voltage on the inner divider drops to 100 volts

AP25: P51-66

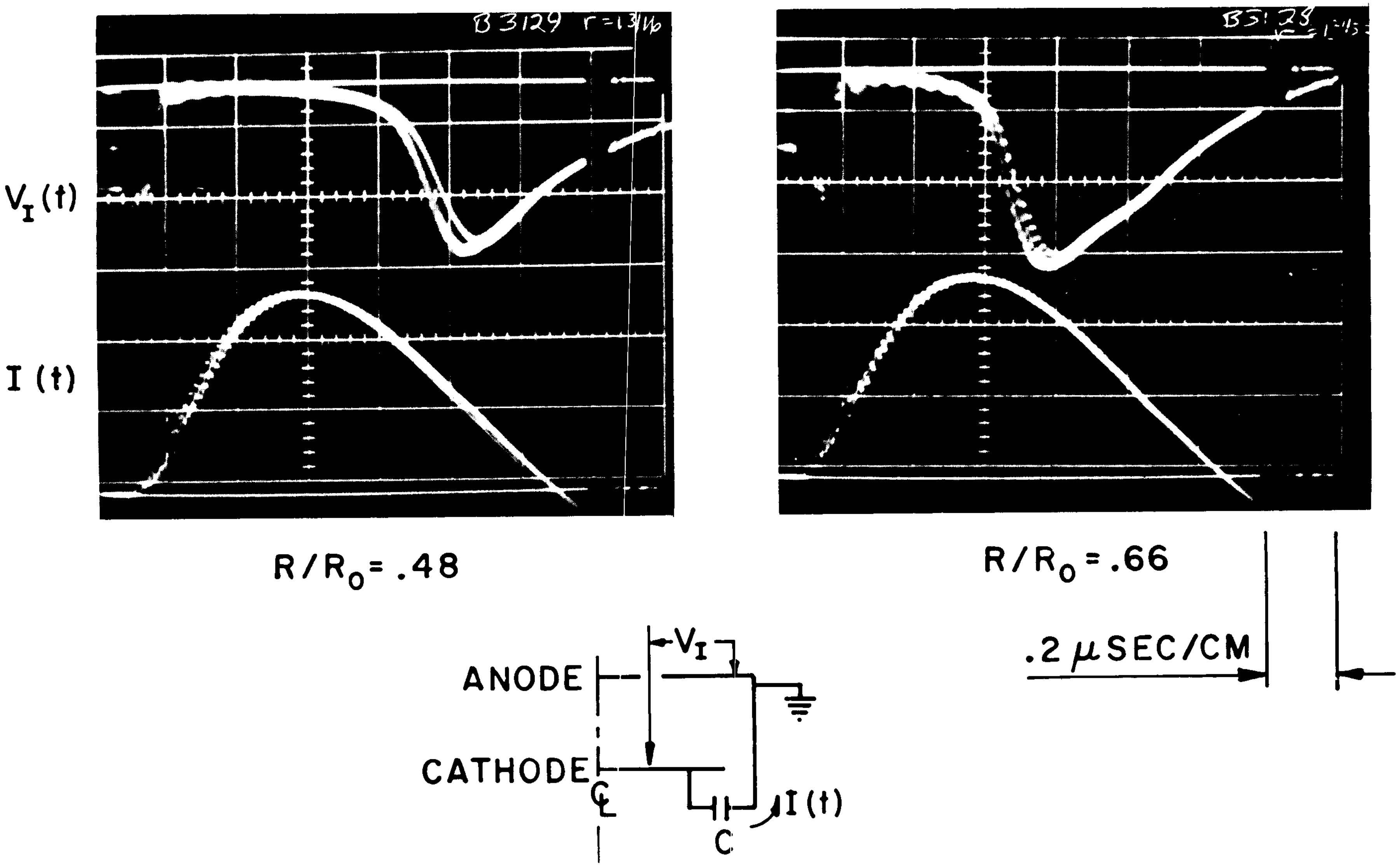

$R/R_0 = .48$

$R/R_0 = .66$

FIGURE 25

INNER VOLTAGE DIVIDER MEASUREMENT, 5" PINCH, 120μ ARGON, 10KV and remains constant until the current sheet arrives. At least 50 of the 100 volts is accounted for by the magnetic flux increase near the anode, found from magnetic probe measurements. Thus no more than 50 volts can be accounted for by resistive drop, much of which may exist in an anode sheath [12]. The small magnitude of this sheath drop precluded any measurements with the present diagnostic equipment, however. Knowing that total current is approximately 2×10^5 amps, by Ohm's Law:

$$R_{plasma} < 0.25\times10^{-3} \quad [\text{OHMS}]$$

Except for the small resistive drop, the voltage measured by the inner voltage divider is induced by changing flux between the probe and the chamber axis. Figure 25 shows that the voltage on the inner divider remains large after the sheet has passed, and does not go to zero along with the total circuit current. Even after 1.20 μsec, when the total current through the chamber has reversed sign, and chamber voltage has also reversed, the inner divider voltage has not reversed, showing that magnetic flux is still increasing between the divider and the chamber axis. The current sheet has decoupled from the external circuit, and two sheets of positive and negative current exist simultaneously in the chamber, so that each electrode acts as both anode and cathode. This phenomenon is more clearly illustrated by a detailed magnetic probe study.

E. MAGNETIC PROBE MEASUREMENTS

Magnetic probe coils inserted radially and axially into the discharge chamber were used to map B_θ as a function of radius, axial distance, and time, for 120 μ Hg argon, 10 kV. Data was taken at points 1/8" apart, and five shots were overlaid on the oscillogram at each probe position. The Rogowski coil signal was recorded on the second beam on every shot, to insure that the scope trigger and discharge were operating properly. The points taken in the surveys are indicated in Fig. 26, together with an oscillogram of the probe output. A survey along the midplane was taken, but not used, when it was found that the probe distorted the magnetic field for this survey, as discussed above.

In the data reduction, advantage was taken of the fact that the axial and radial surveys intersected at several points in the chamber, since at a given time the two measurements of B_θ field must agree. Another aid to data reduction was the known constant velocity propagation of the magnetic field, which implies that $B_\theta(t)$ at a given radius and $B_\theta(r)$ at a given time are related by a Galilean transformation. For short times, so that external current and convective velocity U across the probe are constant:

$$B_\theta(r) \approx B_\theta(r_o + Ut)$$

Knowing U, the B_θ spatial distribution can be quickly estimated from the integrated record of a single probe coil. In addition, smooth magnetic field distributions may be drawn

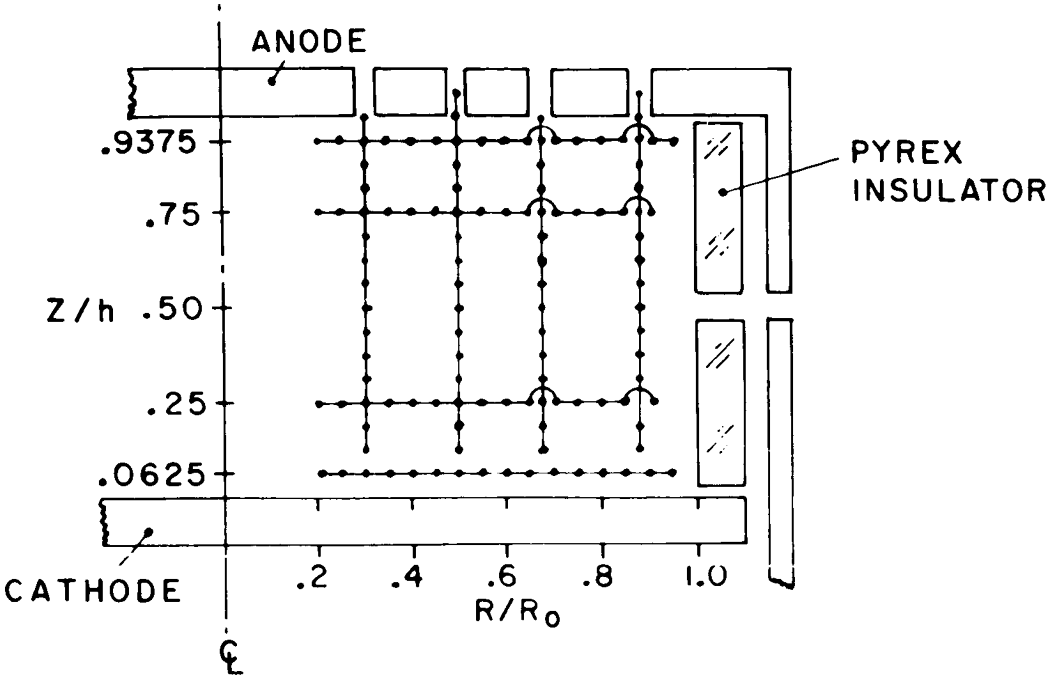

MEASURING POINTS OF MAGNETIC PROBE SURVEYS OF 5" PINCH CHAMBER
$R_0 = 2.5"$, $h = 2"$

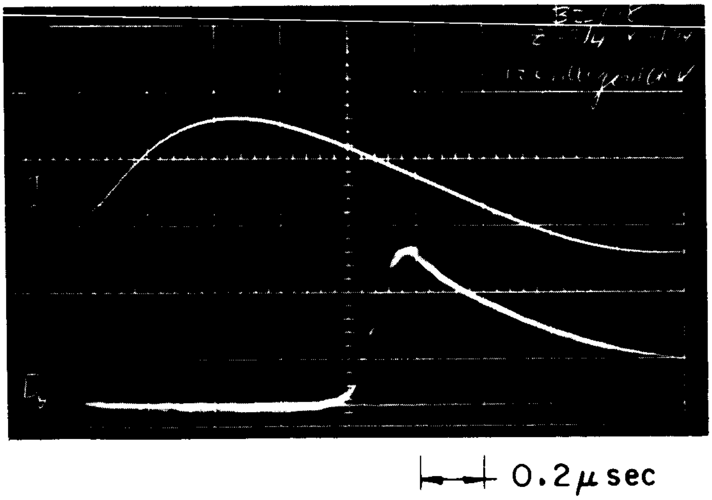

MAGNETIC PROBE RESPONSE, 5 SHOT OVERLAY
$R/R_0 = 0.5$, $Z/h = .375$

FIGURE 26

with confidence from the scattered and sometimes discontinuous appearance of the survey data. The data is "improved" by this method of forcing the data points to fit a predetermined waveform, and the assigning of error bars to the curves therefore becomes somewhat arbitrary. It is fair to say, however, that the error is certainly less than 15 percent.

The current density patterns, derived from spatial derivatives of B_θ, must also bear resemblance to the $\frac{\partial B_\theta}{\partial t}$ output of the magnetic probe. The axial current density is given by the z component of the curl of $\vec{B}$ from Maxwell's equation:

$$\mu_0 j_z = (\vec{\nabla} \times \vec{B})_z = \frac{\partial B_\theta}{\partial r} + \frac{B_\theta}{r}$$

Again assuming constant current and sheet velocity U :

$$\mu_0 j_z(r) \approx \frac{1}{U} \frac{\partial B_\theta(t)}{\partial t} + \frac{B_\theta(Ut)}{r} \qquad (5)$$

Thus the axial current profile is known to a good approximation from a single probe coil record, and Eq. (5) may be used to estimate the peak current density, or to compare peak density at different points in the chamber. As in the case of the $\mathbf{B}_\theta$ distribution, the error assigned to the j distribution is certainly less than 15 percent due to this technique.

The contours of enclosed current in the chamber are derived from the B_θ distributions by Ampere's Law:

$$I_{ENCLOSED} = 2\pi \mu_0^{-1} r B_\theta \qquad \text{[amperes]}$$

These lines of constant current have been plotted at times of .30, .60, .90, and 1.20 μsec. (Figs. 27 to 30). Most immediately striking is the conduction of current over the entire anode surface beginning at $t = 0$. The current density near the anode far ahead of the sheet is typically 10^6 amps/m^2, compared to 10^8 amps/m^2 in the main sheet, but the radial component is larger than the axial component, as can be seen by the angle of the current contour to the electrode.

Approximately 1.5 cm from the anode the current flows nearly axially, with only a slight tilt, and is uniform between z/h = 0.75 and 0.25. The line of maximum current density is shown on Fig. 31, and the small tilt angle in the central region implies that the radial component of the peak current is small compared to the axial component. After 0.90 μsec the region of radial current near the anode propagates inward and also toward the cathode, eventually reaching the midplane.

Negative current flows near the insulator wall after .75 μsec, but does not disturb the magnetic field patterns in the first sheet. This negative current is forced to remain at the wall, since $j_z B_\theta$ points radially outward in this region. The current in the main current sheet becomes larger than total circuit current as the pinch proceeds, as shown in Fig. 32. When circuit current is zero, at 1.20 μsec, 1.0x10^5 amperes still flow in the first sheet and $\vec{j} \times \vec{B}$ work is being done on the plasma. Thus, total external current does not imply zero magnetic energy in the discharge chamber, and the concept of a single overall inductance for the chamber is unserviceable.

AP25-4143-66

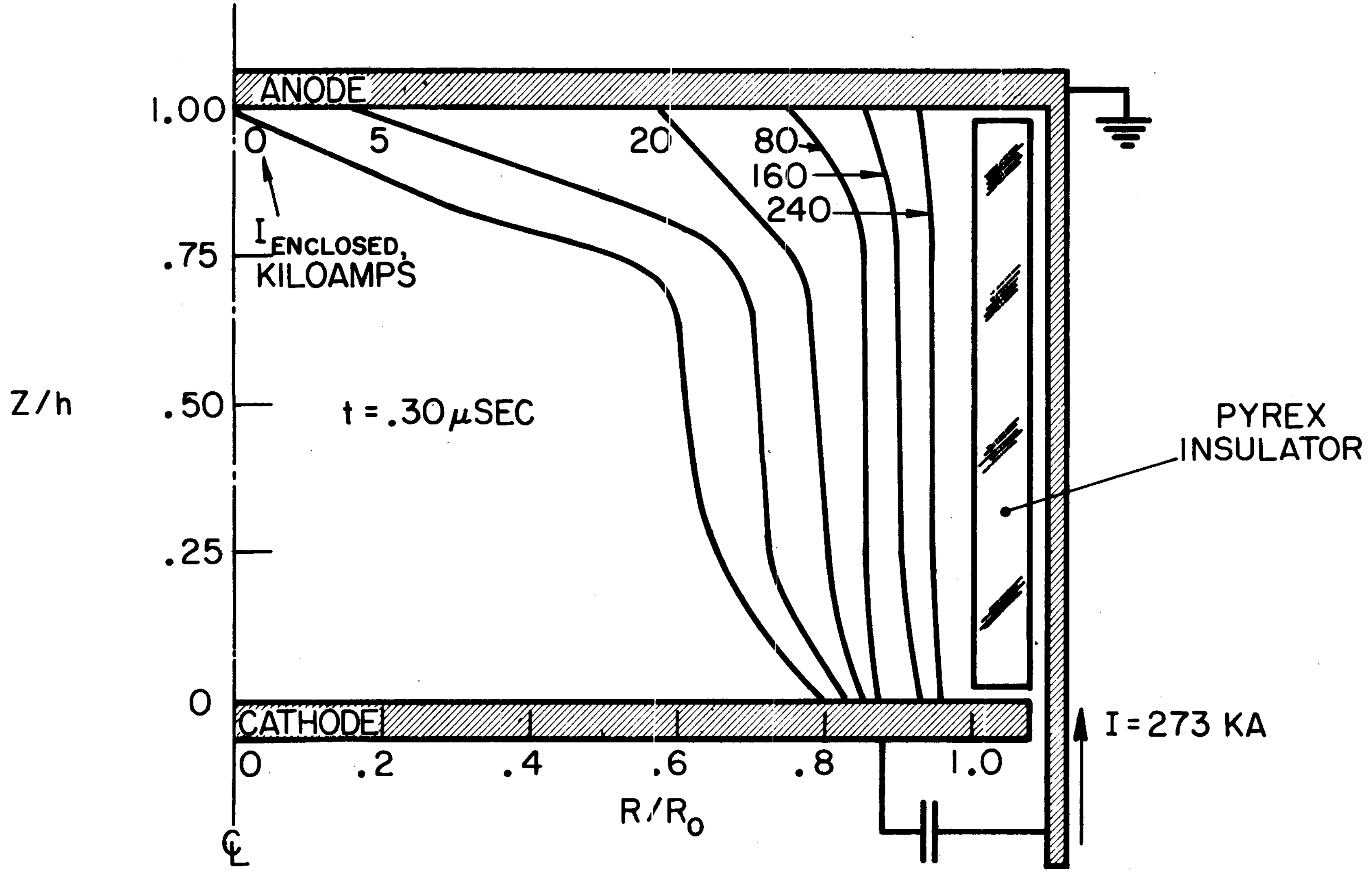

CONTOURS OF CONSTANT ENCLOSED CURRENT
5" PINCH, 120μ ARGON, 10KV

FIGURE 27

AP25-4146-66

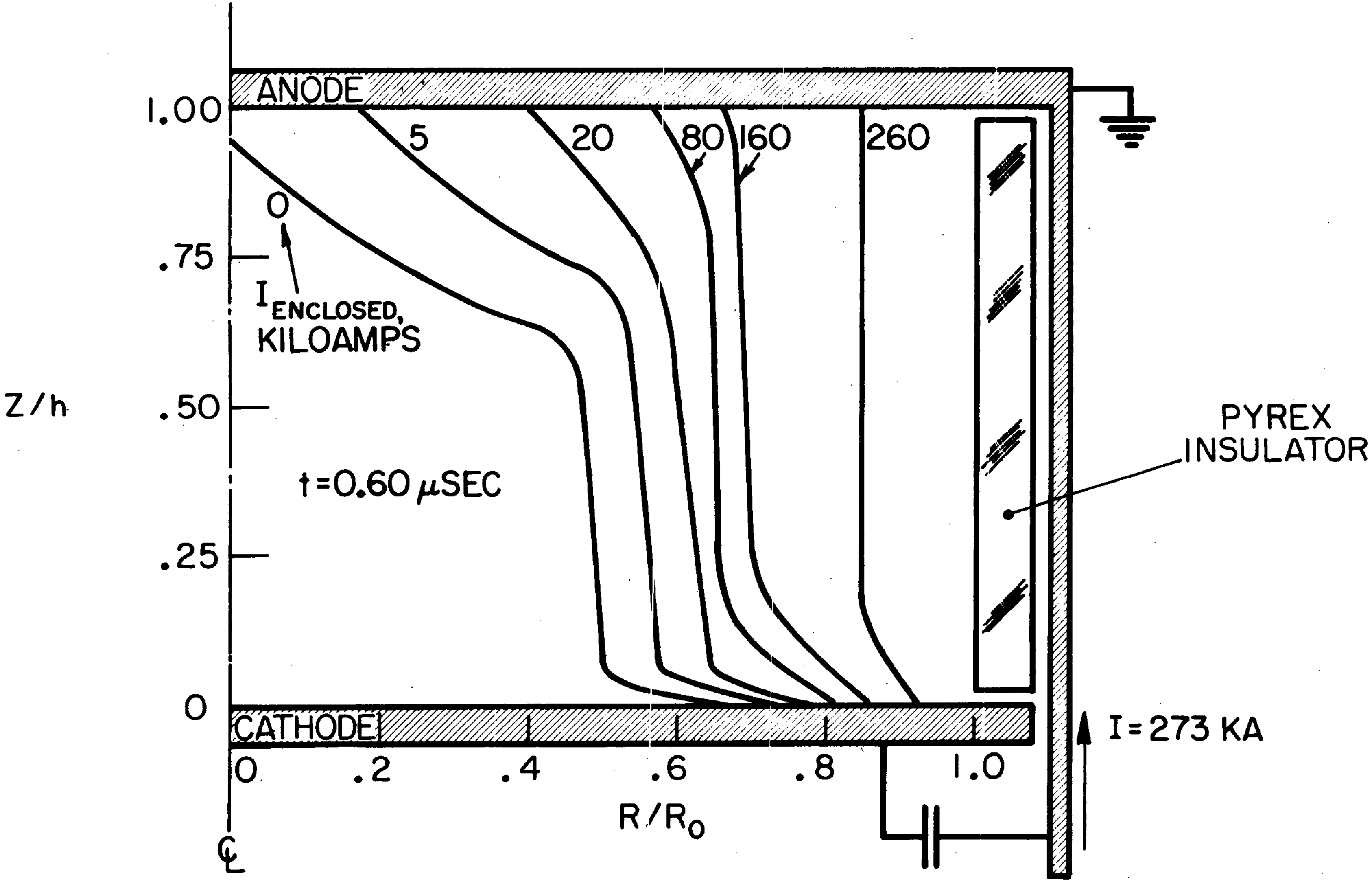

CONTOURS OF CONSTANT ENCLOSED CURRENT
5" PINCH, 120μ ARGON, 10KV

FIGURE 28

AP25-4145-66

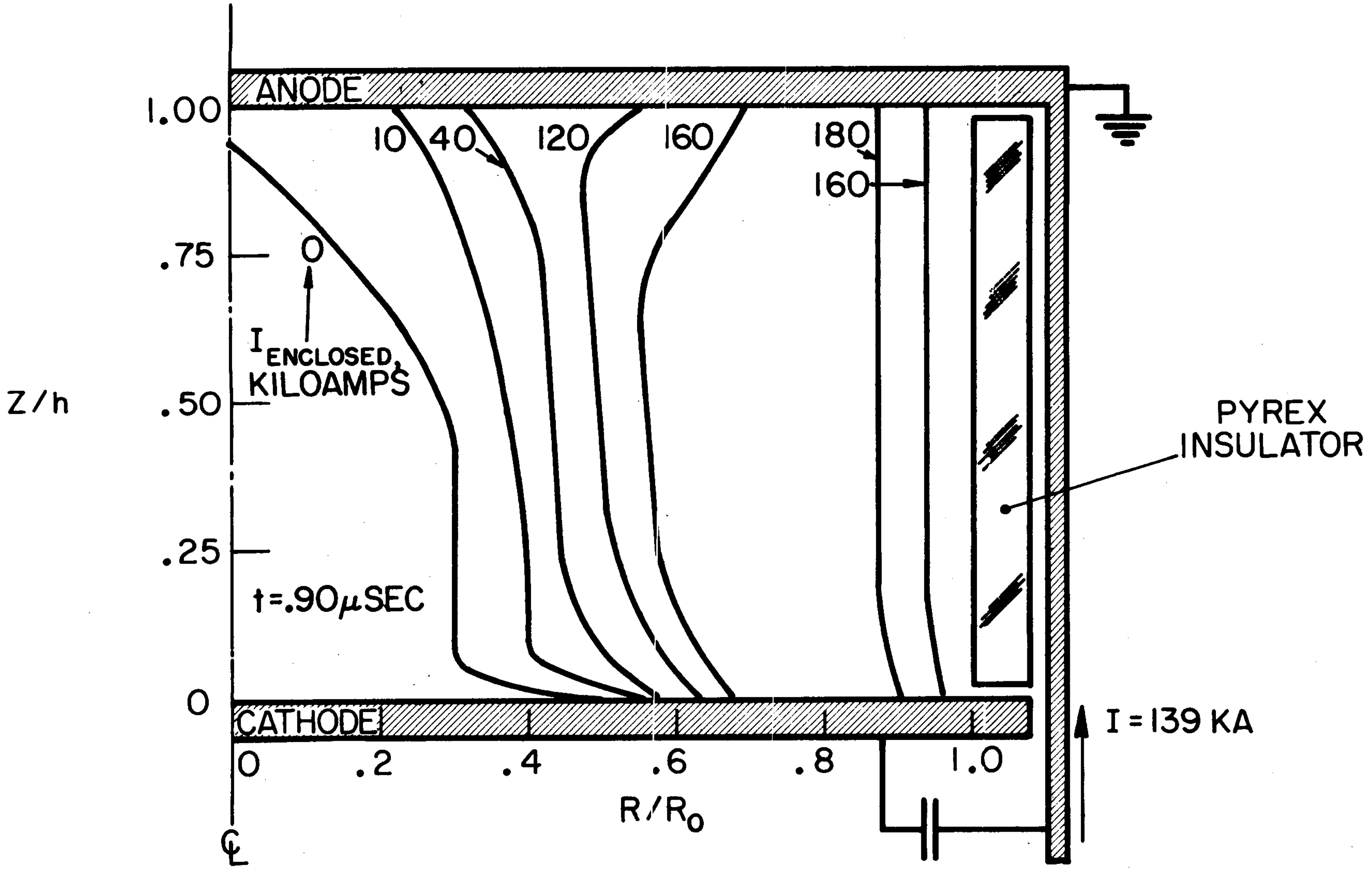

CONTOURS OF CONSTANT ENCLOSED CURRENT
5" PINCH, 120μ ARGON, 10KV

FIGURE 29

AP25-4144-66

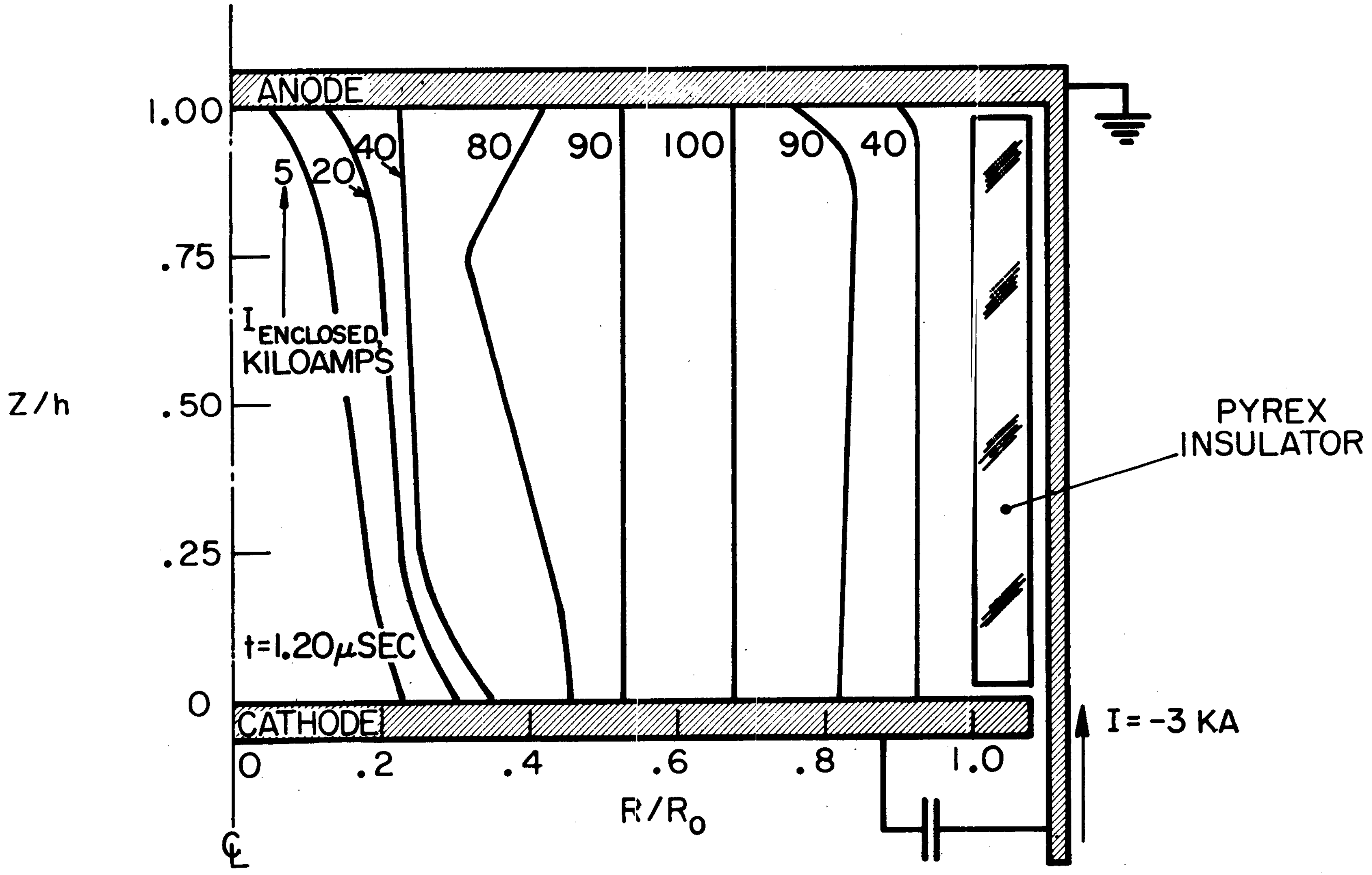

CONTOURS OF CONSTANT ENCLOSED CURRENT
5" PINCH, 120μ ARGON, 10KV

FIGURE 30

AP25-4063-66

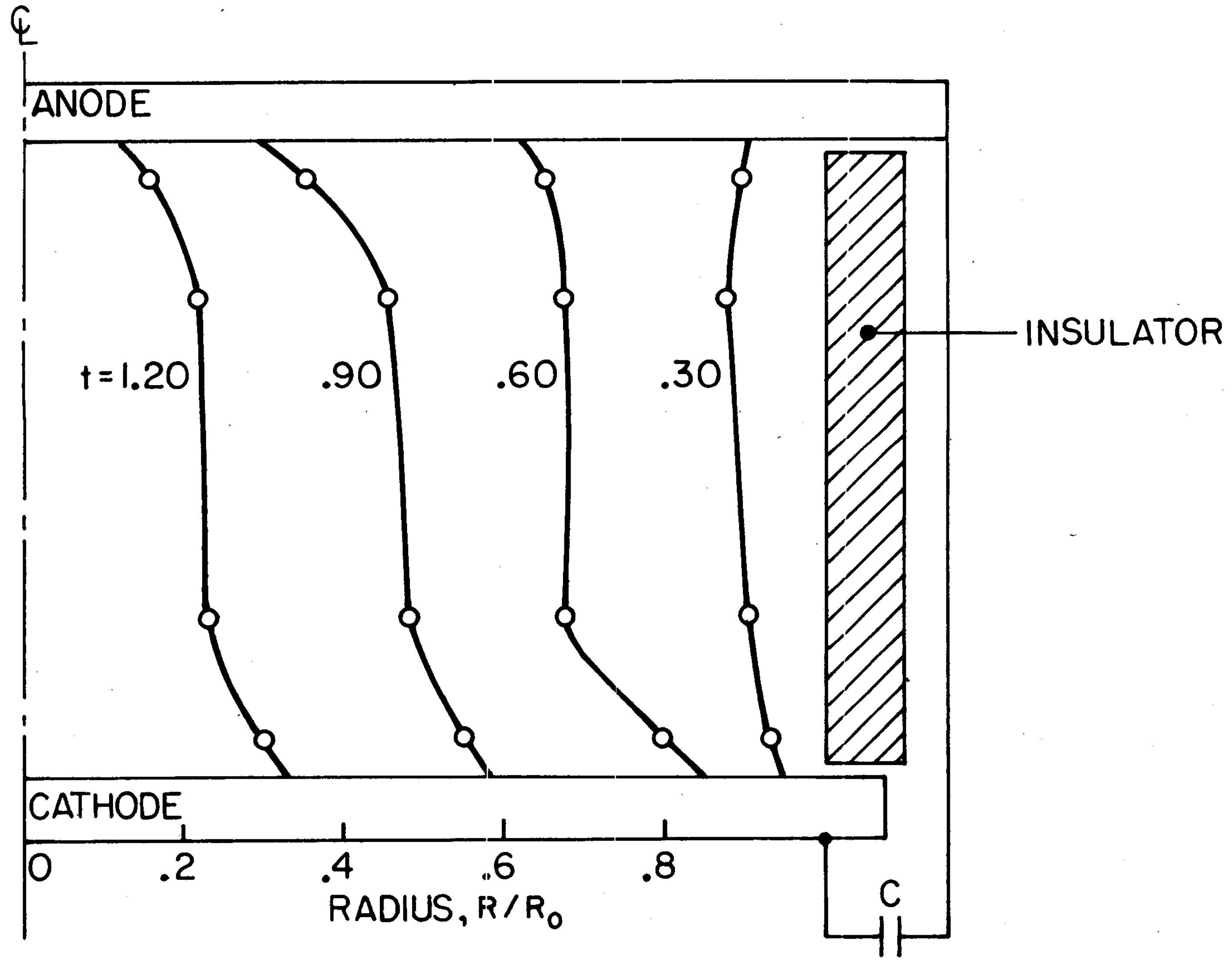

MAXIMA IN AXIAL CURRENT DENSITY, j_z
5" CHAMBER, 10 KV, 120μ ARGON

FIGURE 31

AP25-4141-66

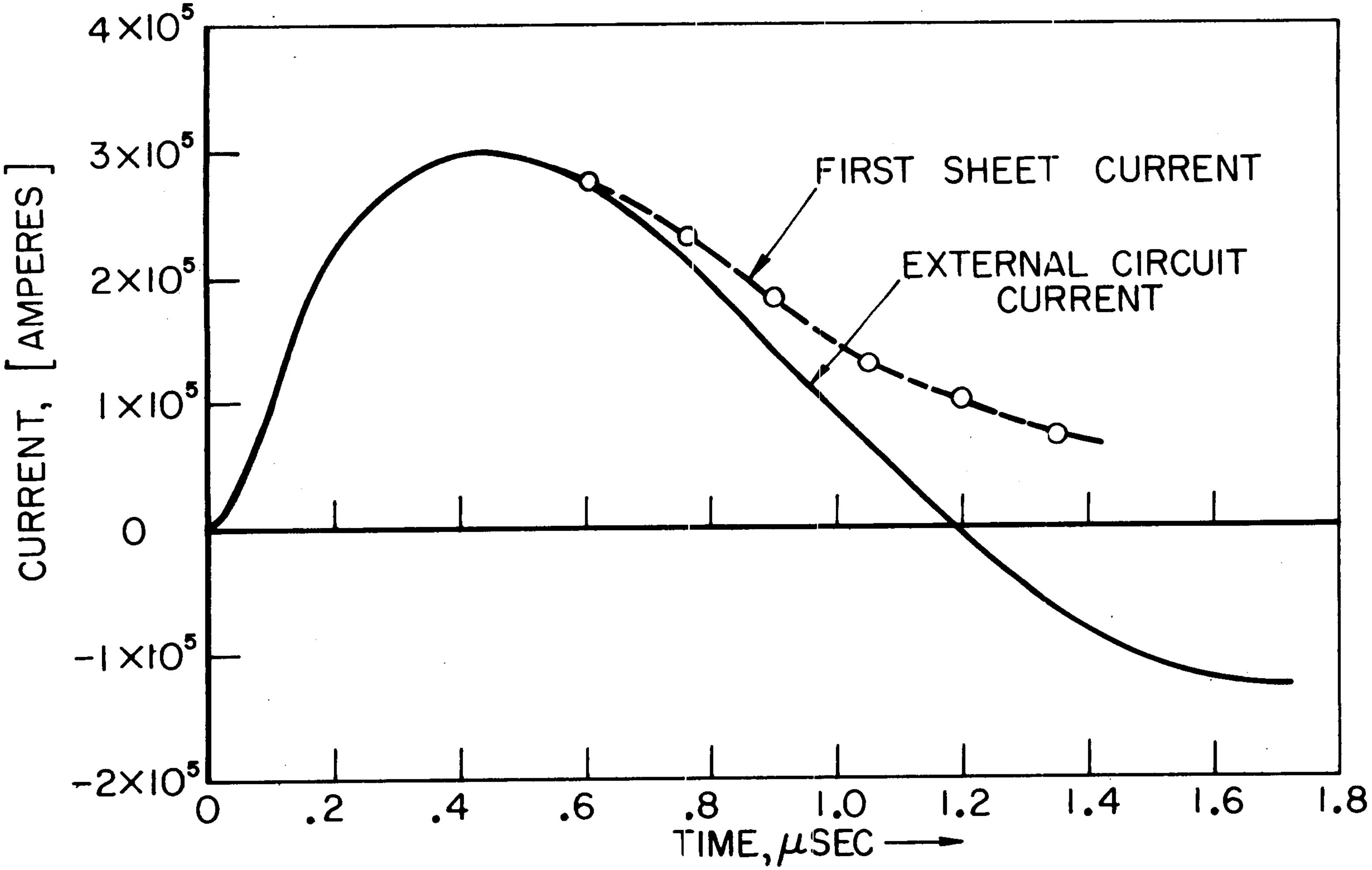

MEASURED CURRENT IN EXTERNAL CIRCUIT & FIRST CURRENT SHEET
5" PINCH, 120μ ARGON, 10 KV

FIGURE 32

Calculation of the current density from Maxwell's equation was simplified, since nowhere in the discharge chamber was a radial or axial component of $\vec{B}$ observed. Furthermore, the shot-to-shot reproducibility and the symmetry of Kerr Cell photographs make valid the assumption that azimuthal (θ) gradients are zero. Under these conditions only two components remain from Maxwell's equation for current density:

$$\mu_o \dot{j}_r = -\frac{\partial B_\theta}{\partial z}$$

$$\mu_o \dot{j}_z = \frac{1}{r}\frac{\partial r B_\theta}{\partial r}$$

Because the axial gradient in B_θ is always small compared to the radial gradient, except in the region of the anode foot, the electromagnetic acceleration is dominated by the inward radial $\dot{j}_z B_\theta$ term. Axial current $\dot{j}_z$ has been determined by graphical differentiation of the B_θ field according to the above equation, and the results are plotted for nine selected times, in Figs. 33 to 41. In each graph the r-z plane is horizontal, and $\dot{j}_z$ is plotted in the vertical direction. The axial position of the current density maxima is shown more clearly in Fig. 31.

Several important aspects of the current density distribution in Figs. 33 to 41 have been already mentioned. The current density pattern on the anode is broader than in the main sheet, and never exceeds $.8 \times 10^8$ amps/m^2. The anode current reaches the center of the discharge prior to the main sheet, which in turn pinches before the current to the cathode. The cathode current density peak is lower than the main sheet, and is typically $.9 \times 10^8$ amps/m^2.

The maximum current density observed in the main sheet

AP25-4087-66

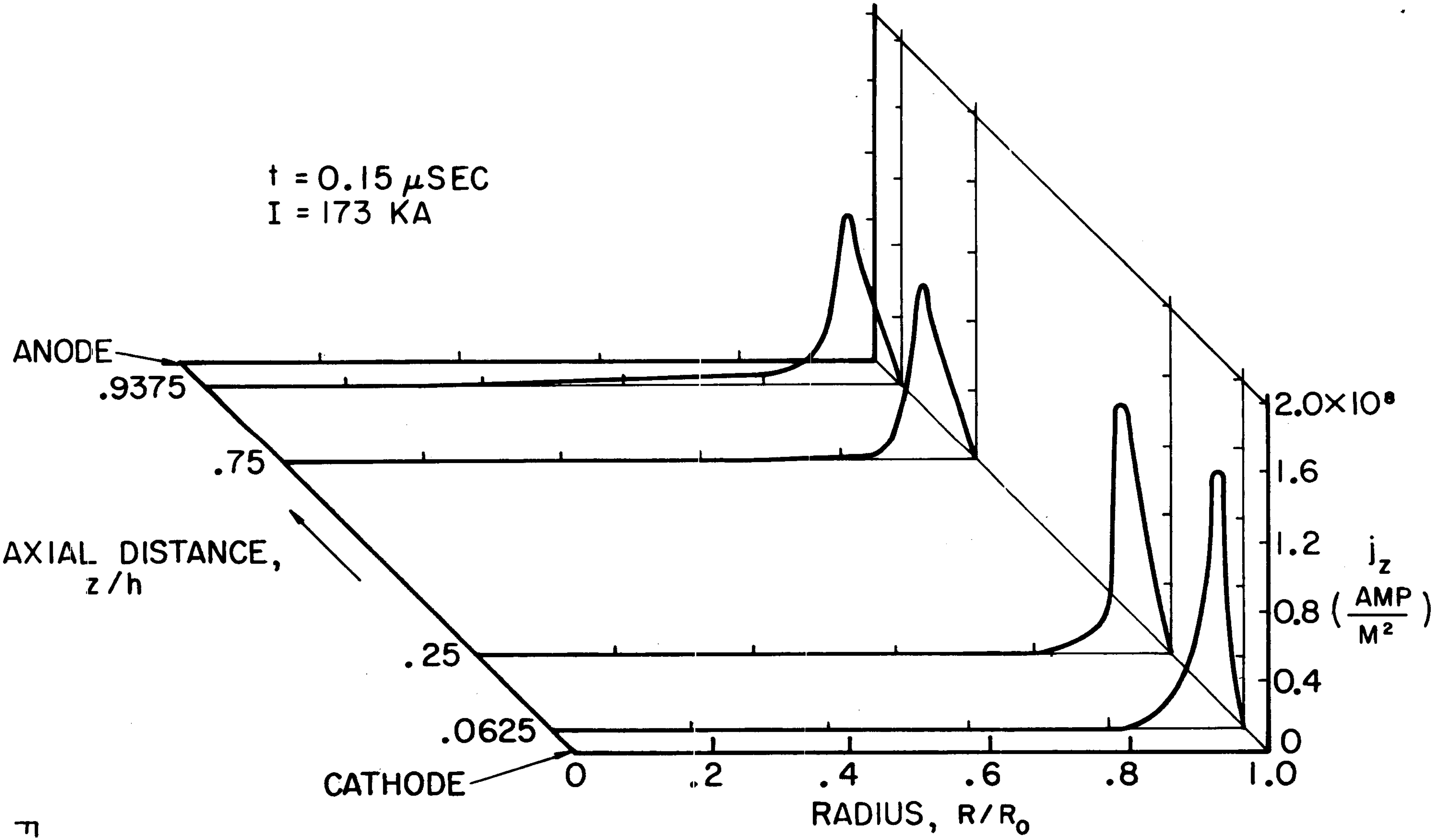

AXIAL CURRENT DENSITY DISTRIBUTION

5" CHAMBER, 120μ ARGON, 10 KV

FIGURE 33

AP25-R4070-66

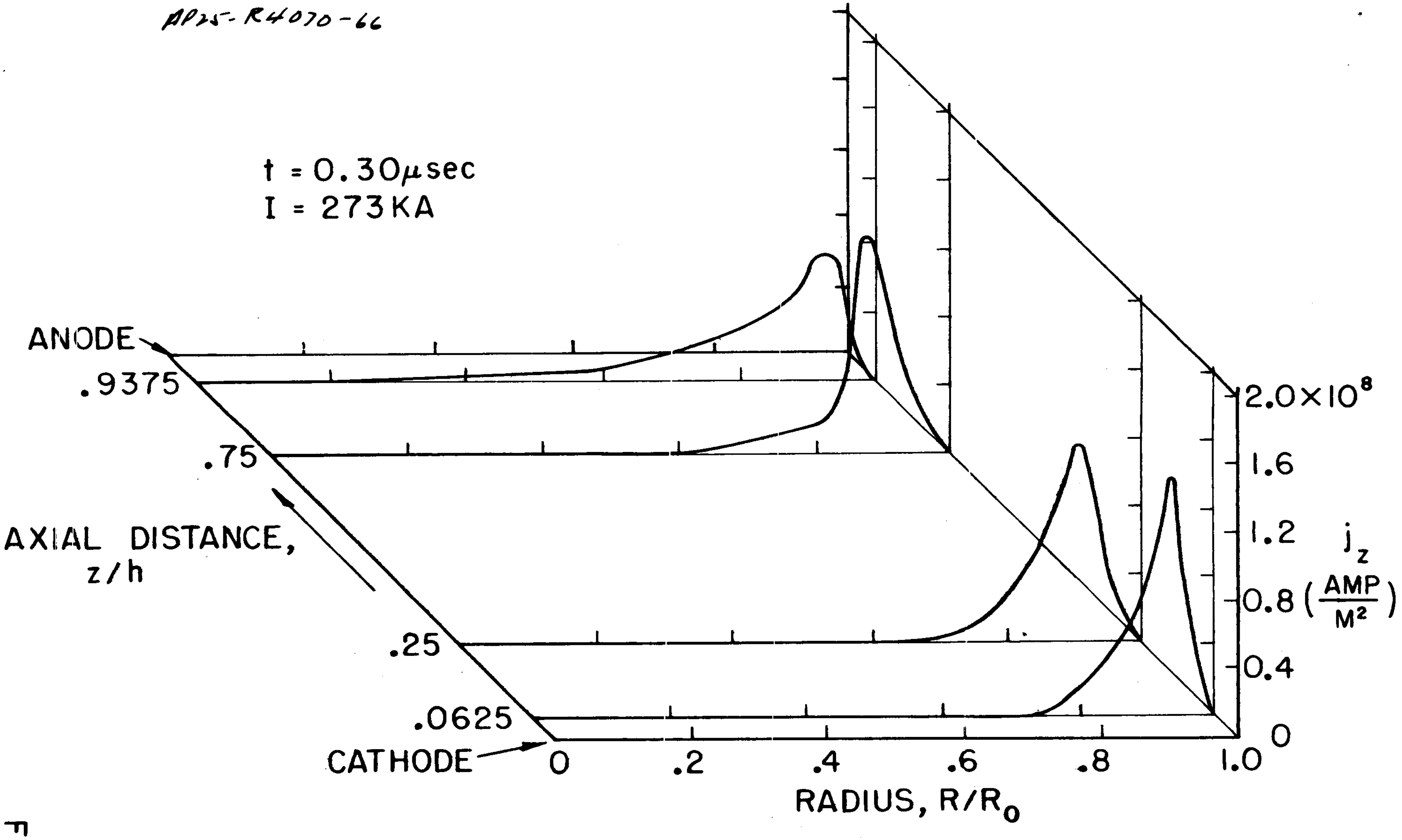

AXIAL CURRENT DENSITY DISTRIBUTION

5" CHAMBER, 120μ ARGON, 10KV

FIGURE 34

AP25-4083-66

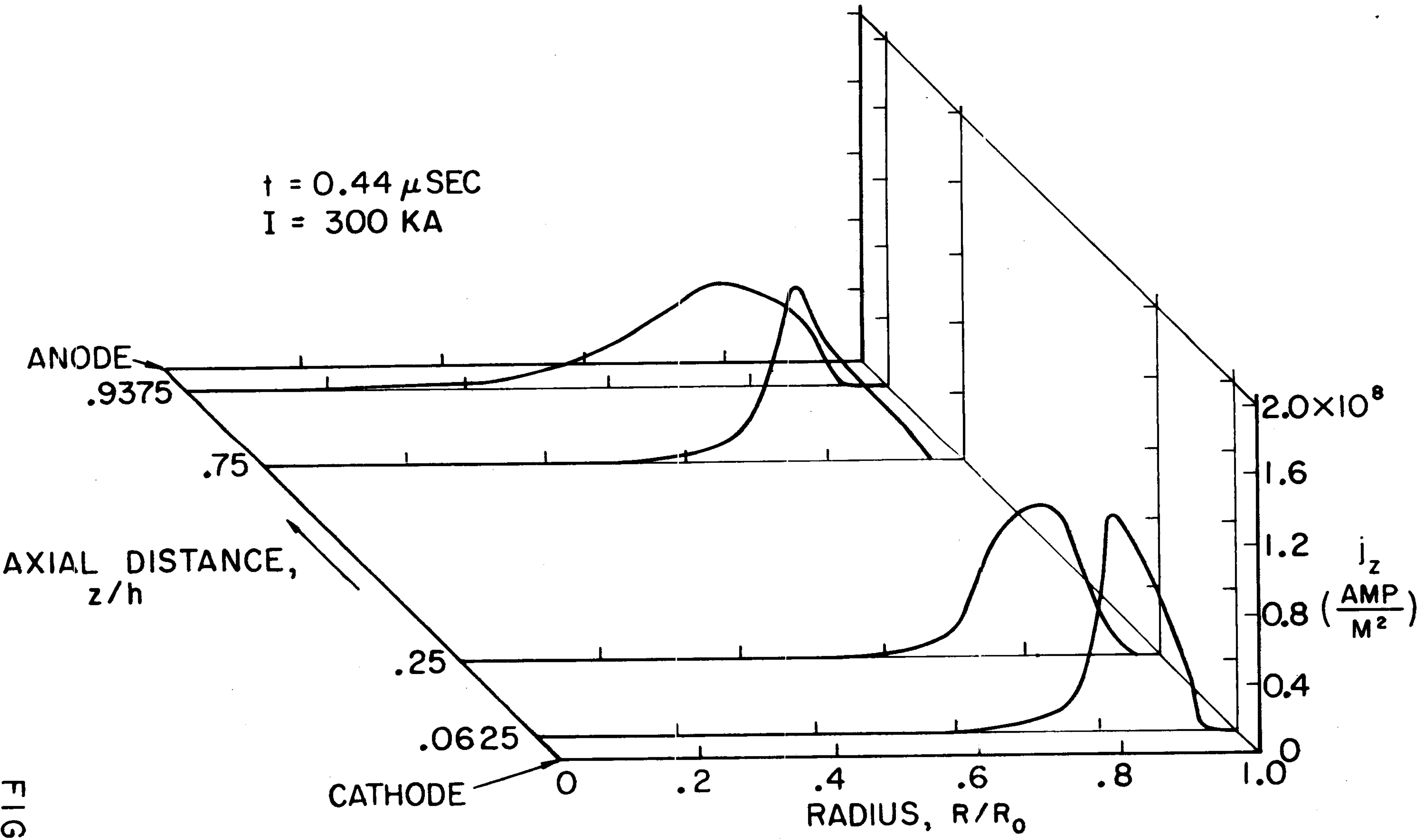

AXIAL CURRENT DENSITY DISTRIBUTION

5" CHAMBER, 120μ ARGON, 10 KV

FIGURE 35

AP25= RA071-66

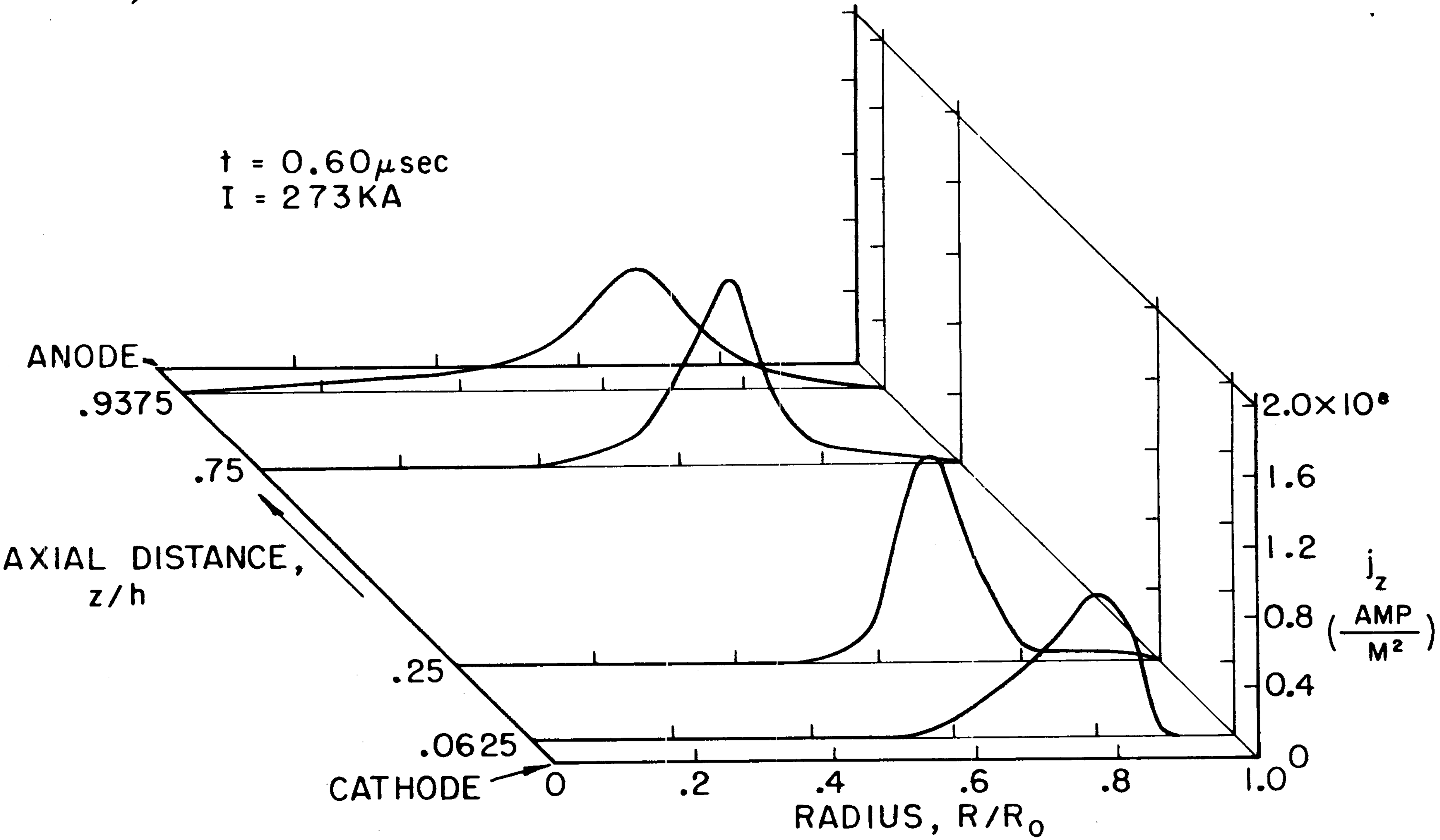

AXIAL CURRENT DENSITY DISTRIBUTION

5" CHAMBER, 120μ ARGON, 10KV

FIGURE 36

AP25-4086-66

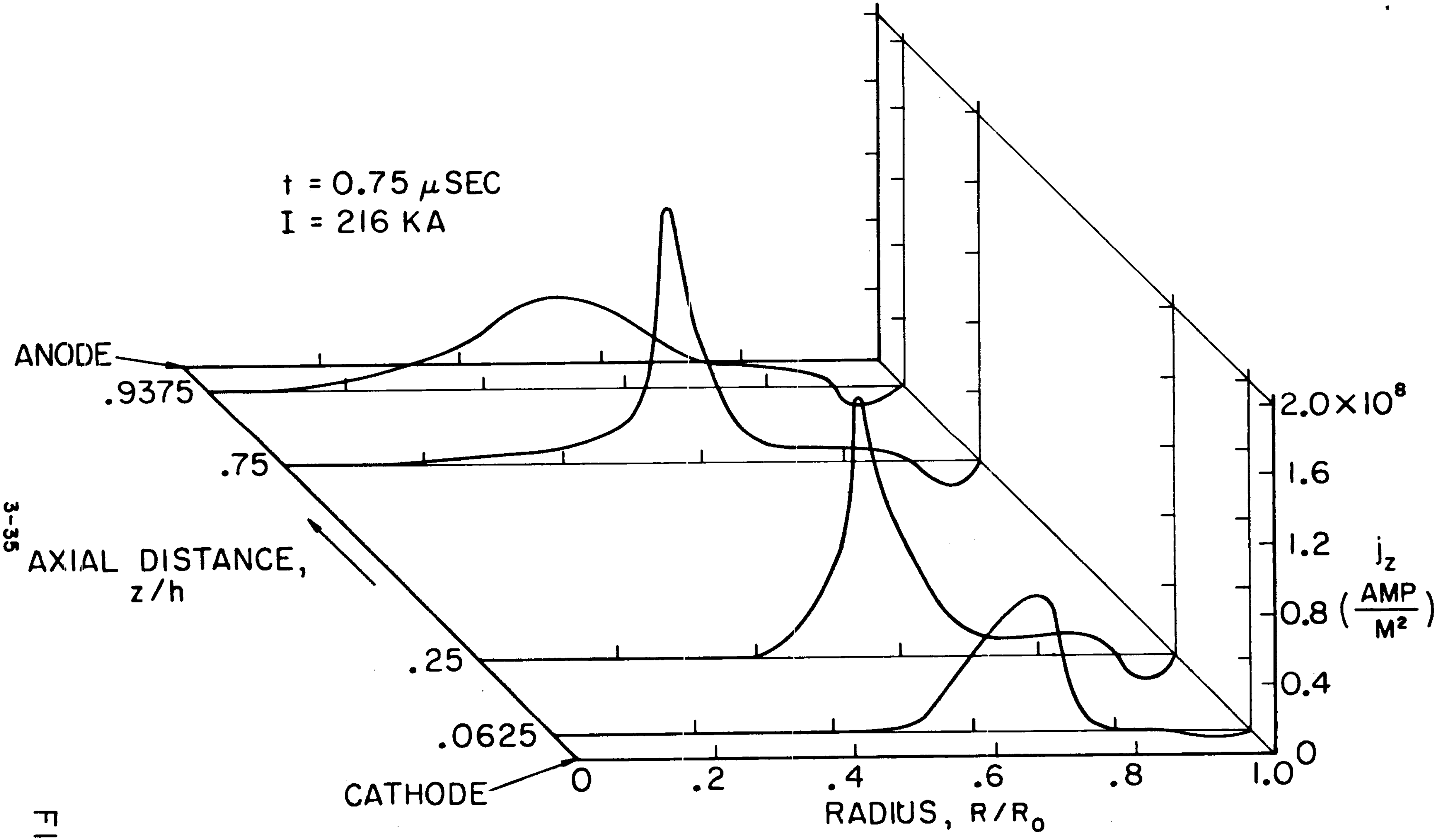

AXIAL CURRENT DENSITY DISTRIBUTION

5" CHAMBER, 120 μ ARGON, 10 KV

FIGURE 37

AP25-R4069-66

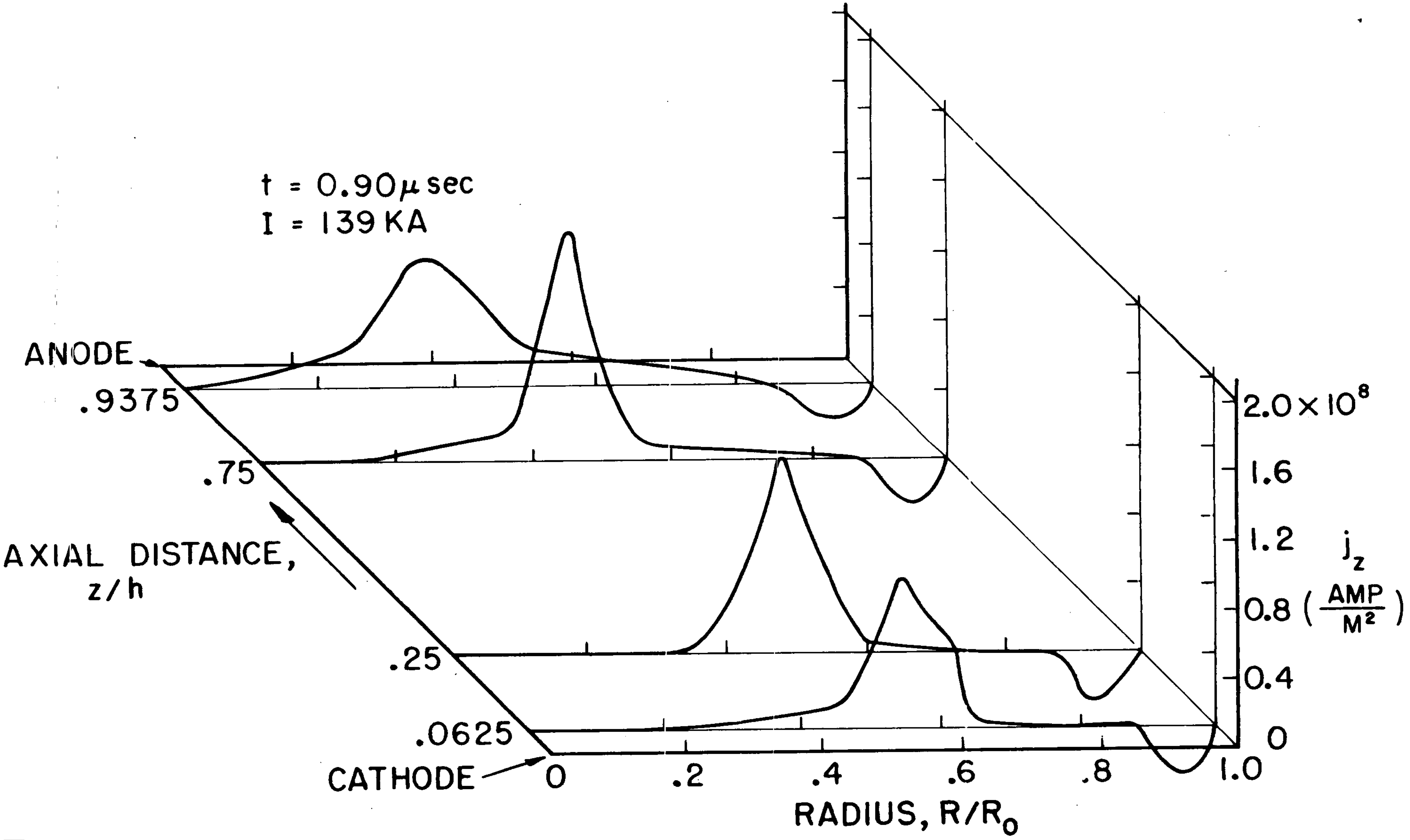

AXIAL CURRENT DENSITY DISTRIBUTION

5" CHAMBER, 120μ ARGON, 10KV

FIGURE 38

AP25-4085-66

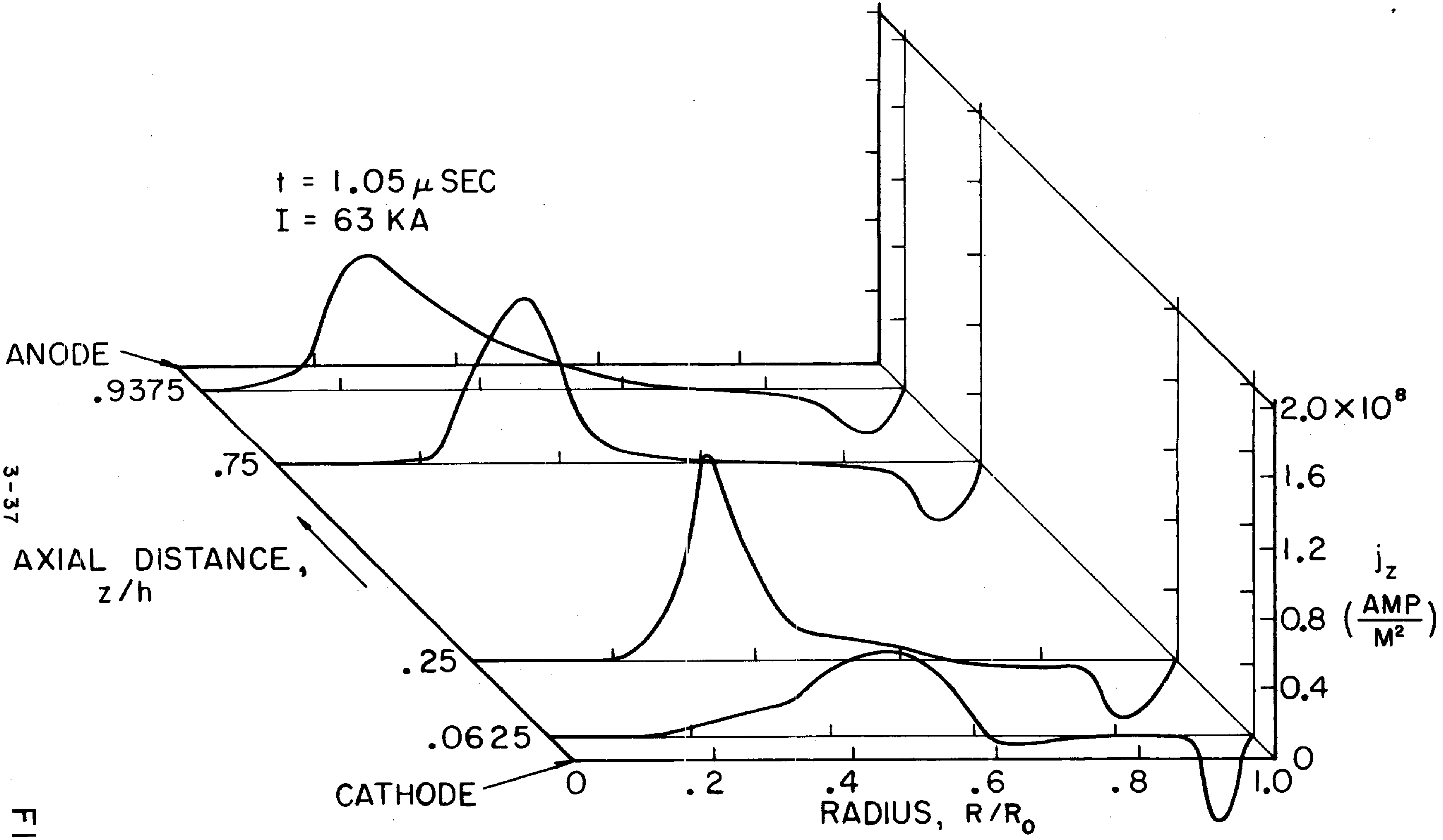

AXIAL CURRENT DENSITY DISTRIBUTION

5" CHAMBER, 120μ ARGON, 10 KV

FIGURE 39

AP25-R4072-66

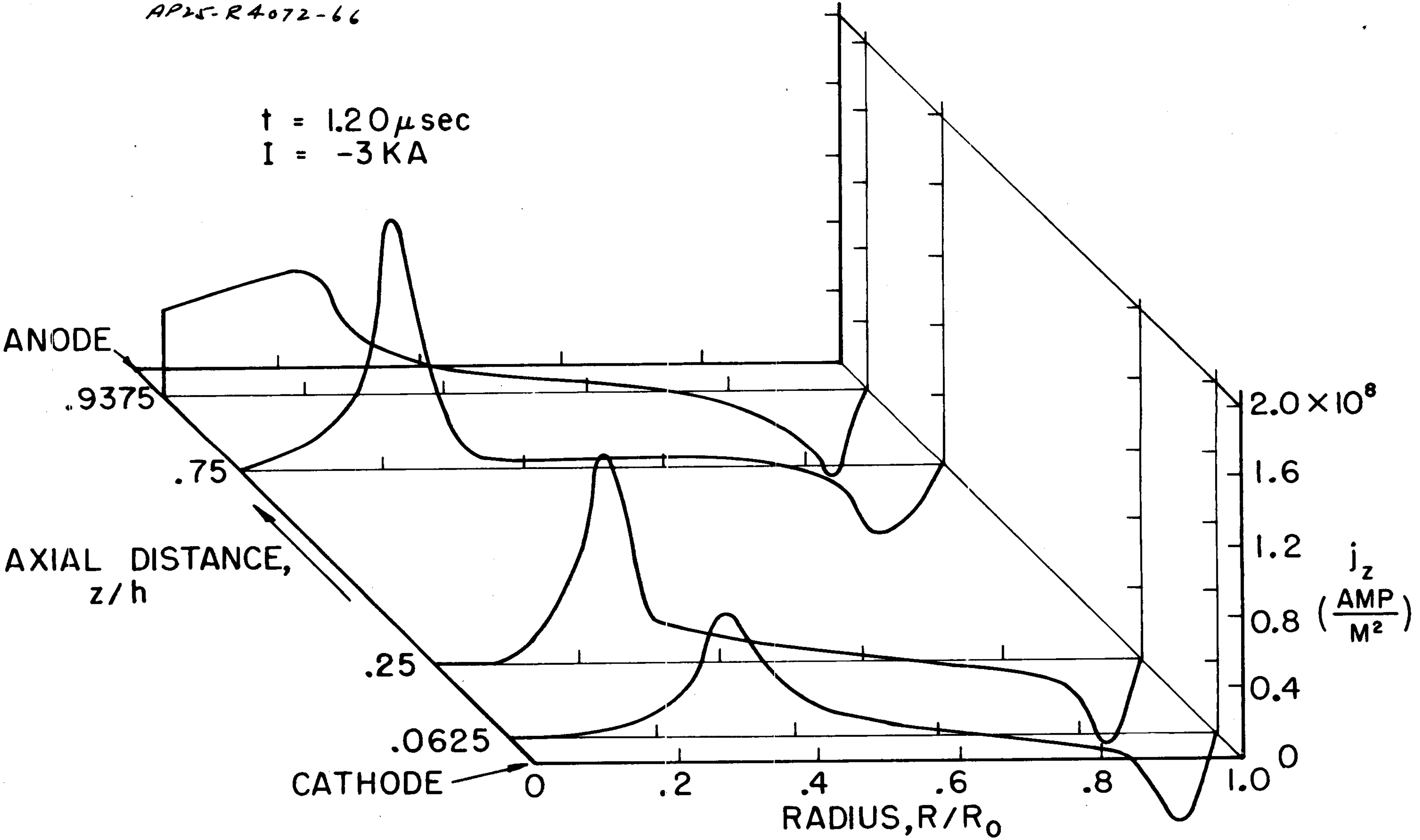

AXIAL CURRENT DENSITY DISTRIBUTION

5" CHAMBER, 120 μ ARGON, 10 KV

FIGURE 40

AP25-4084-66

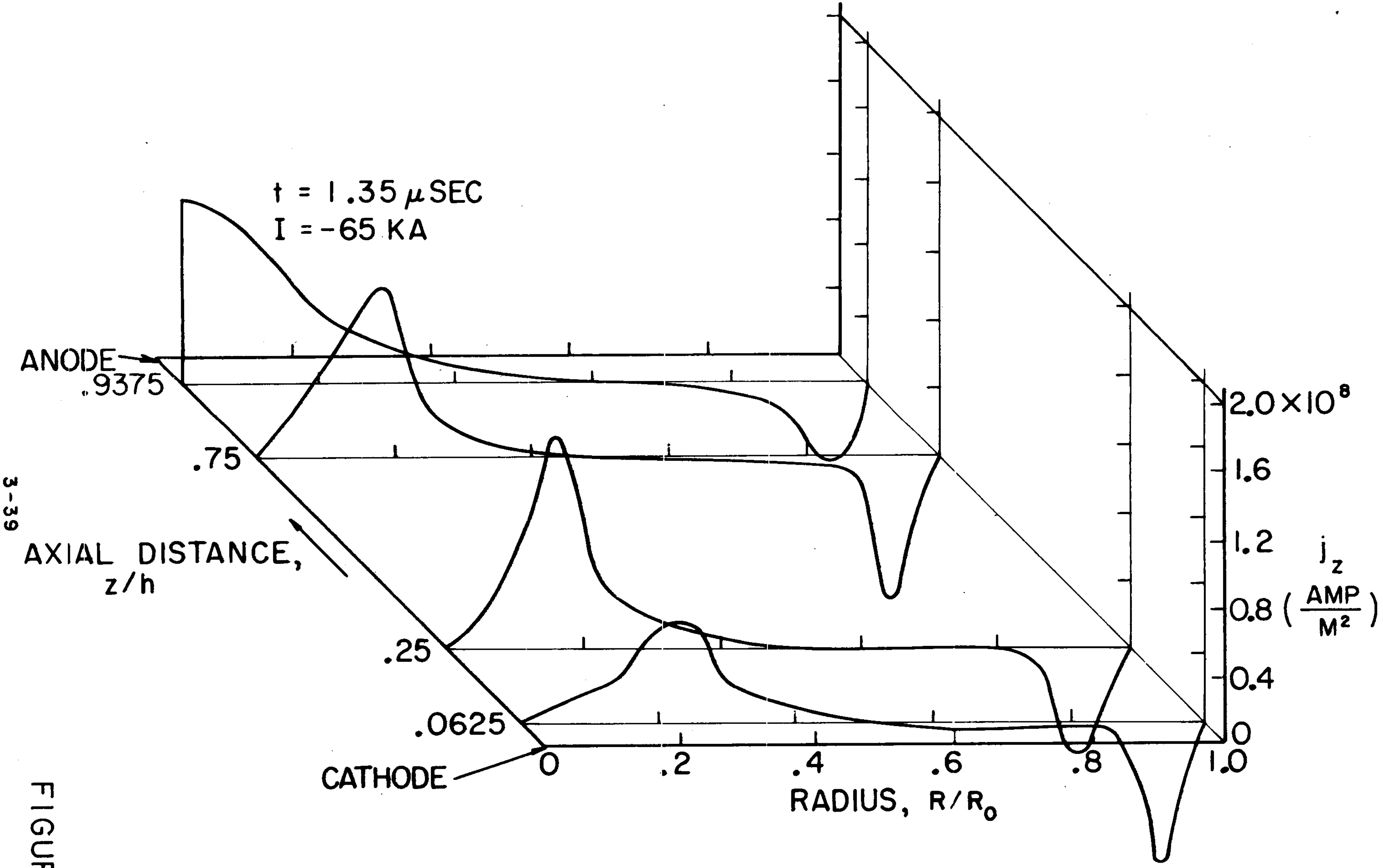

AXIAL CURRENT DENSITY DISTRIBUTION

5" CHAMBER, 120μ ARGON, 10 KV

FIGURE 41

is 1.4×10^8 amps/m^2. The radial width of the main current sheet varies by 20 percent, being greatest when the maximum circuit current is being conducted, but on the average is 8 mm. After 0.4 μsec, the sheet propagates at a nearly constant velocity of 4.3×10^4 m/sec, until pinch time.

Negative current, flowing in the opposite direction to current in the main sheet, is first observed near the wall at 0.75 μsec. Before circuit current reversal, this small negative current is unable to reverse the direction of B_θ, and so is pinned against the chamber wall by the locally outward force density. At 1.20 μsec the B_θ field reverses sign, directing $j_z B_\theta$ inward, and a second sheet is free to propagate. The second sheet moves into a plasma with unknown varying properties; it's structure is not investigated.

The distribution of $j_z B_\theta$ force density displays the same feature as the axial current distribution. A typical $j_z B_\theta$ distribution is compared with j_z in Fig. 42, showing that $j_z B_\theta$ peaks at a larger radius than j_z. The average peak value of $j_z B_\theta$ is $.5 \times 10^8$ newtons/m^3 as the main sheet propagates inward.

Although measurements show that $j_z B_\theta$ decreases near the electrodes, similar axial variations in the integrated force $2\pi\int_0^r j_z B_\theta r\,dr$ do not exist. Near the anode the current sheet is relatively thick, and the $j_z B_\theta$ force density acts over a larger volume, so that integrated force along the anode is comparable to that in the main sheet. Figure 43 is a plot of the axial distribution of radial force

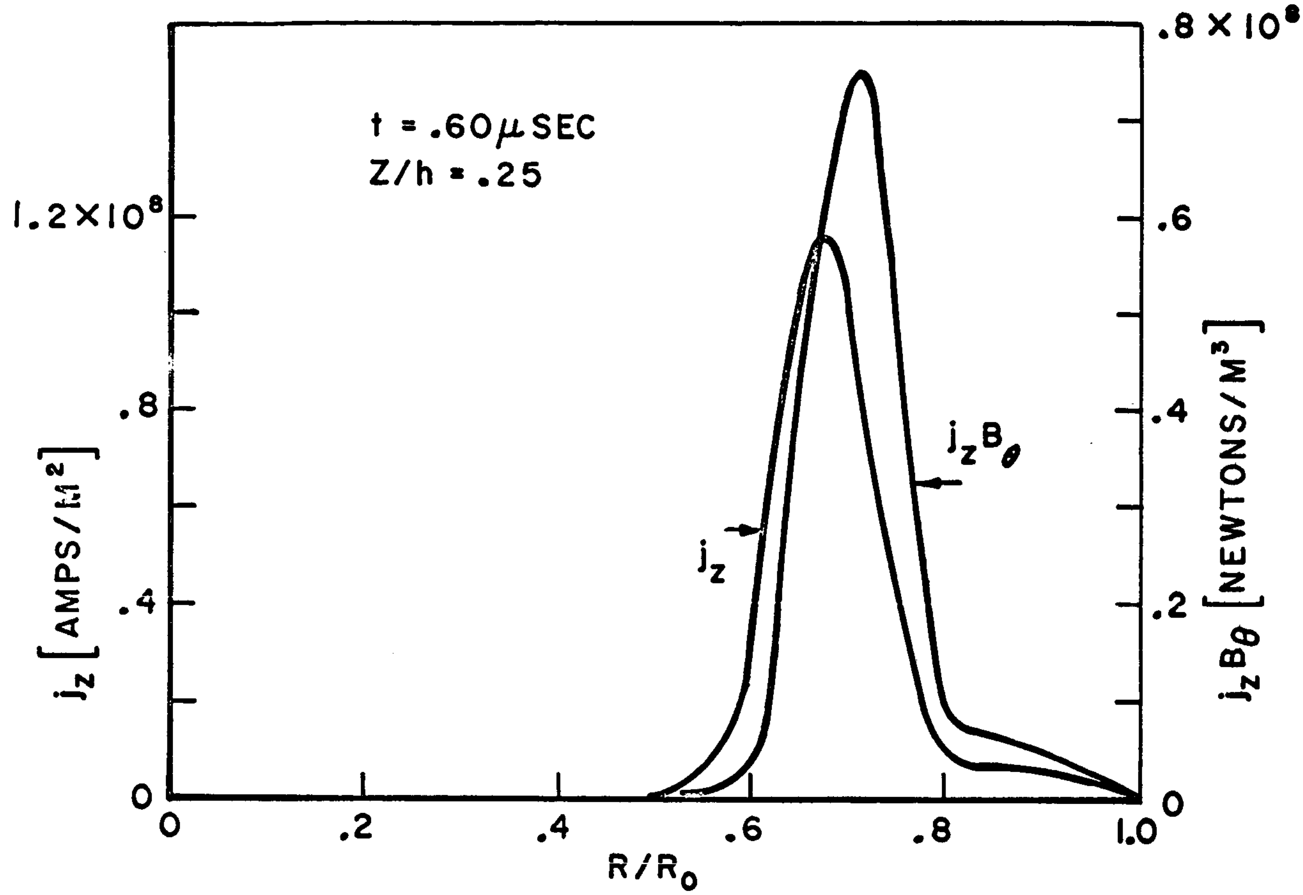

RADIAL DISTRIBUTION OF CURRENT & FORCE DENSITY, 5" PINCH, 120μ ARGON, 10KV

FIGURE 42

at different times. Except for a thin cathode region, the radial force shows little change throughout the chamber.

Integrating $j_z B_\theta$ over the entire current sheet volume and chamber volume yields the total radial electromagnetic force F_r as a function of time (Fig. 44). Outward radial force appears when the second current sheet forms at .75 μsec, and thus the integrated force over the whole chamber volume is less than the force on the first current sheet. Maximum electromagnetic force on the current sheet is 8450 newtons (1900 pounds), at .53 μsec. Dividing this force by the current sheet area on which the force acts yields an electromagnetic pressure of 5.88×10^6 dynes/cm² (6 atmospheres).

AF25-4150-60

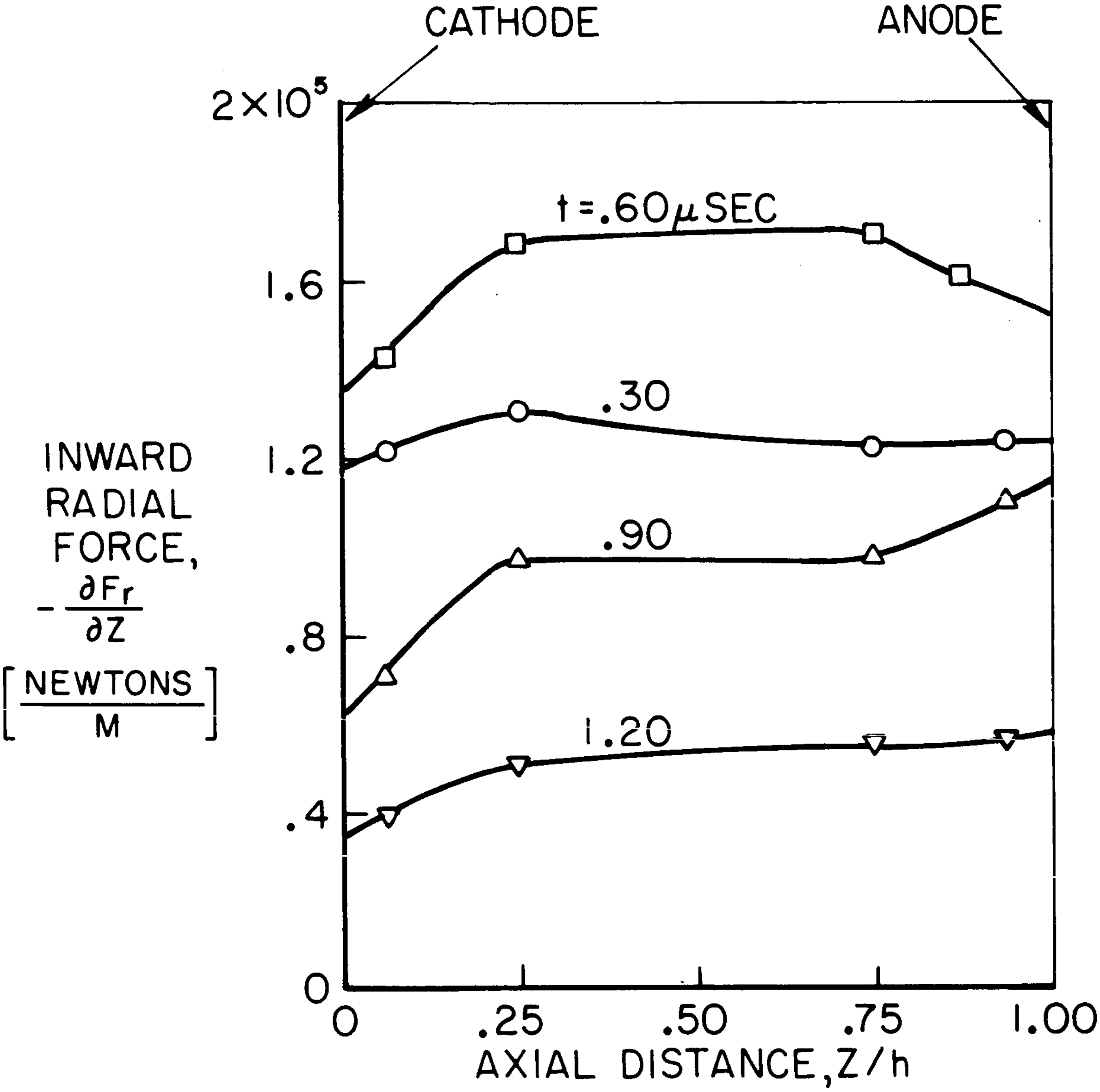

$$\frac{\partial F_r}{\partial Z} = 2\pi \int_0^r j_z B_\theta r\,dr \left[\text{NEWTONS/M}\right]$$

AXIAL DISTRIBUTION OF RADIAL FORCE IN FIRST CURRENT SHEET, 5" PINCH, 120μ ARGON, 10KV

AP25-4/52-66

FIGURE 43

AP25-4147-66

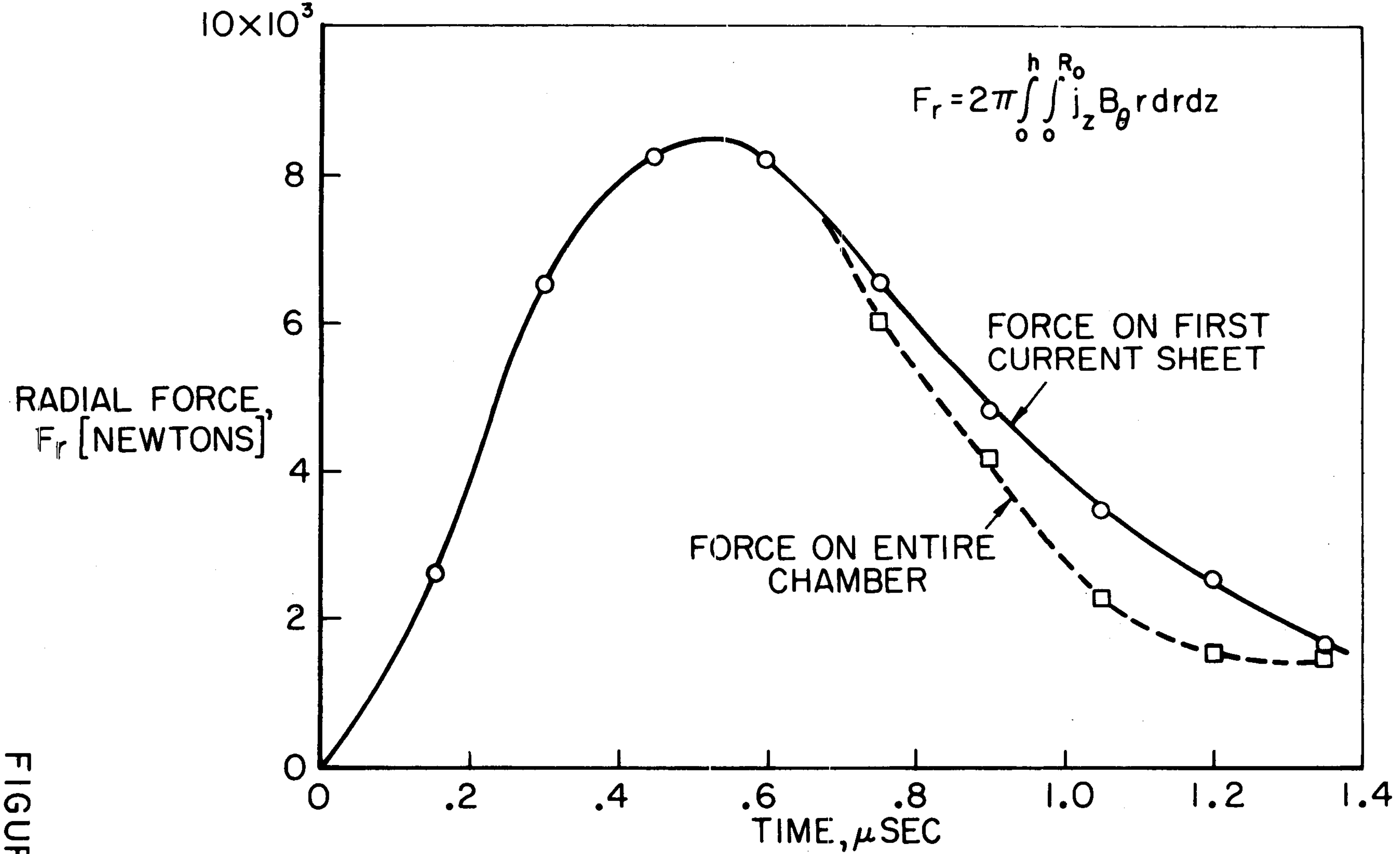

INWARD RADIAL ELECTROMAGNETIC FORCE, F_r
5" PINCH, 120μ ARGON, 10KV

FIGURE 44

The net impulse imparted to the first current sheet is calculated from the time integral of the radial force F_r in Fig. 44. At the pinch time t_p :

$$\int_0^{t_p} F_r\,dt = 6.9\times10^{-3}\ [\mathrm{kg\text{-}m/sec}]$$

The initial mass m_o filling the chamber is, for 120 μ argon:

$$m_o = 1.68\times10^{-7}\ [\mathrm{kg}]$$

The total impulse divided by m_o defines an impulse velocity U_I :

$$U_I \equiv \frac{1}{m_o}\int_0^{t_p} F_r\,dt = 4.1\times10^{4}\ [\mathrm{m/sec}]$$

This value of U_I corresponds to a thruster specific impulse of about 4,000 seconds, and agrees closely with the measured velocity of the current density maxima near the chamber axis of 4.3×10^4 m/sec. This agreement indicates that nearly all the mass in the chamber is swept up by the current sheet, precluding the possibility that, to achieve the measured impulse, a "leaky" current sheet might have elected to accelerate a mass less than m_o to a velocity greater than U_I .

Integration of the magnetic field in the chamber yields the time dependent magnetic flux $\phi(t)$:

$$\phi(t) = \int_0^{h}\int_0^{R_o} B_\theta\,dr\,dz \qquad [\mathrm{WEBERS}]$$

This integral is plotted in Fig. 45, compared with the time

AP25-4139-66

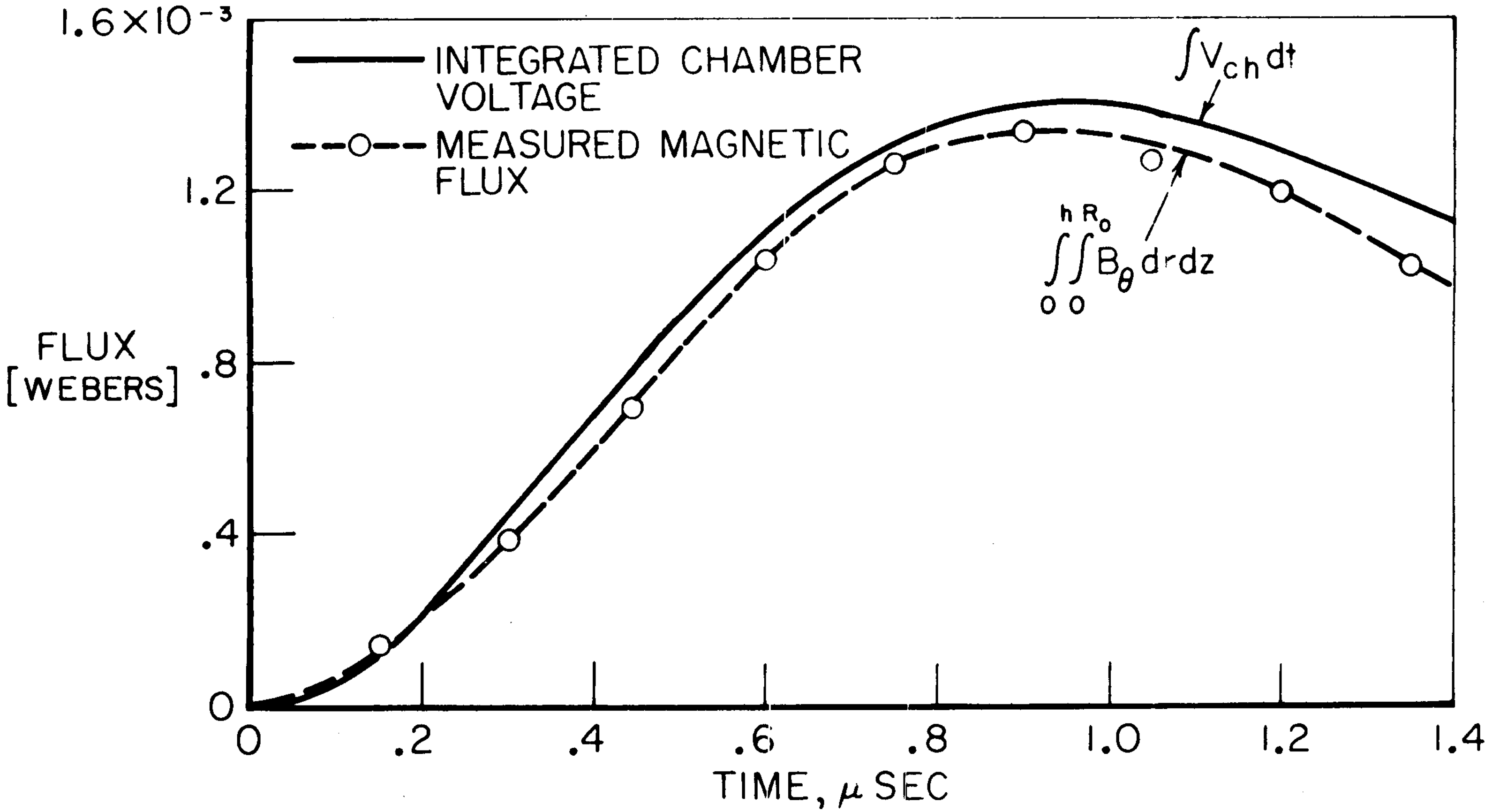

COMPARISON OF INTEGRATED CHAMBER VOLTAGE & MAGNETIC FLUX,
5" PINCH, 120μ ARGON, 10KV

FIGURE 45

integral of the chamber voltage $\int_0^t V_{CH}\, dt$, which equals $\phi(t)$ when the plasma resistance is zero. The close agreement of the magnetic and voltage probe data provides more evidence that the impedance of the chamber is inductive and not resistive.

The radial current density j_r was also determined by graphical differentiation of the B_θ field. Figures 46 and 47 show j_r versus z/h at eight selected times, for $R/R_o = 0.5$. In the central region of the sheet the radial current density is an order of magnitude smaller than j_z , consistent with the observation of a small tilt angle. The vector relation among the components of current density is shown below; to scale:

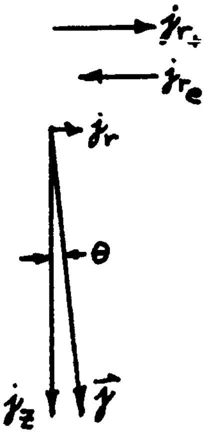

The magnitude of the radial ion current is computed by assuming the incoming particles are fully ionized, which gives a value $j_{r_+} = 2.9\text{x}10^7$ amps/m^2. The radial current j_r is the sum of ion and electron current, and when added vectorially to j_z , causes the total current $\vec{j}$ to tilt an angle θ from the axis. Since θ and φ (Fig. 21) are both measured to be

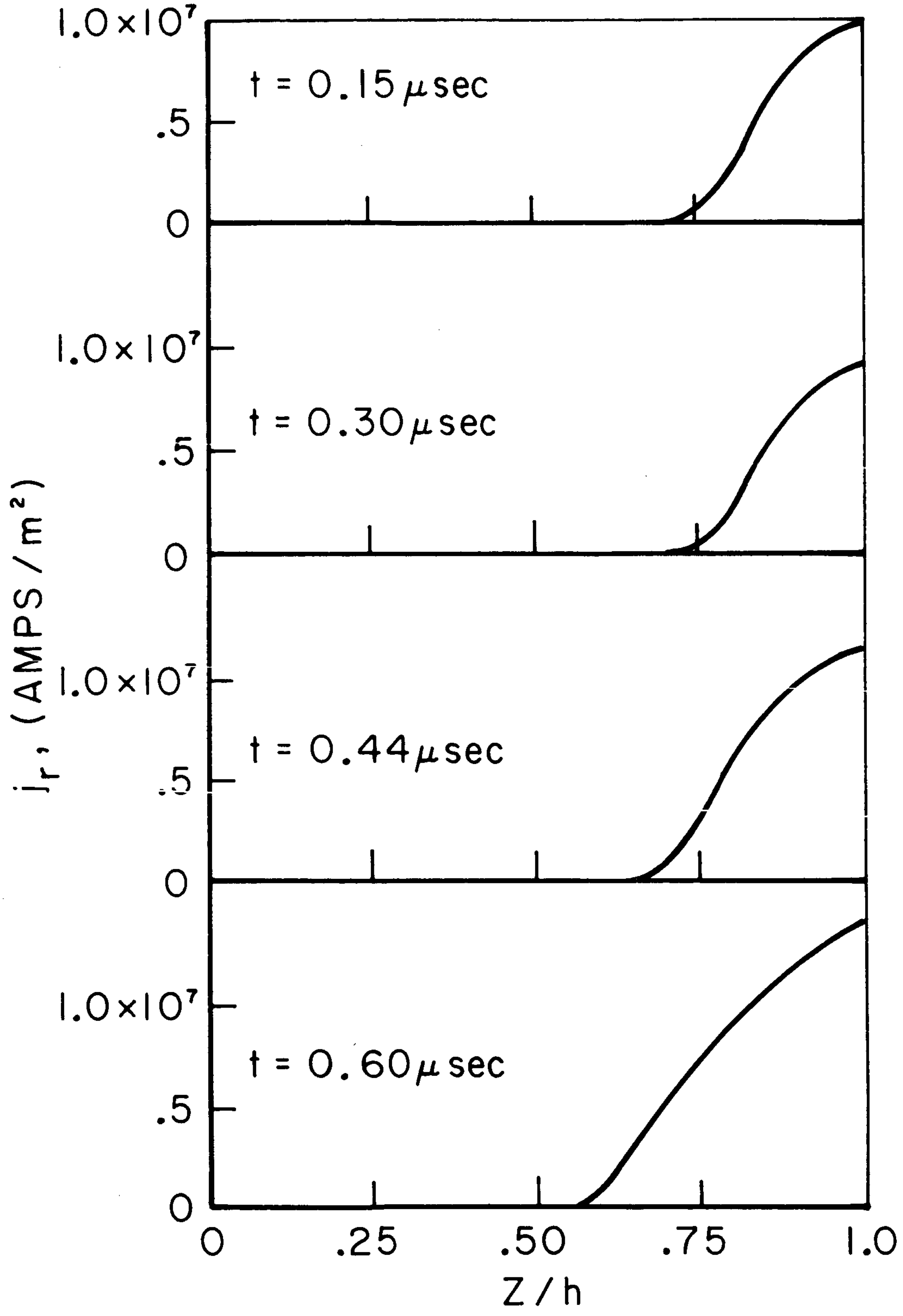

AP25-R4166-66

RADIAL CURRENT DENSITY DISTRIBUTION
5" CHAMBER, 120μ ARGON, 10KV, $R/R_0 = 0.5$

FIGURE 46

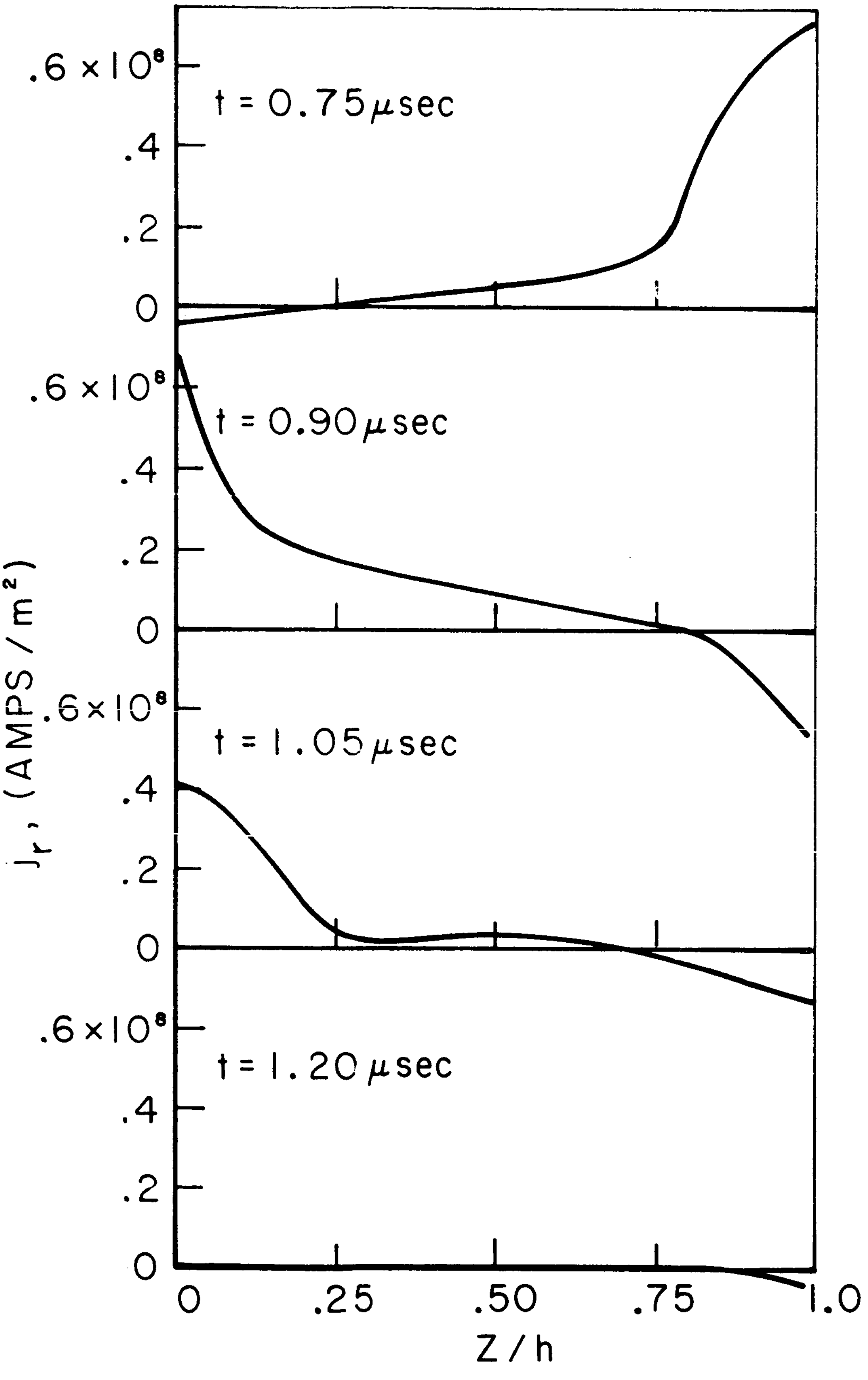

AP35-R 4165-66

RADIAL CURRENT DENSITY DISTRIBUTION
5" CHAMBER, 120μ ARGON, 10 KV, $R/R_0 = 0.5$

FIGURE 47

a few degrees, it is very probable that the tilt angle of the current sheet is just that angle seen on the luminous photographs (Fig. 18).

The data shows (Fig. 47) that the radial current density on the electrodes reverses sign as the sheet passes the probe. Before .75 μsec, j_r is positive (radially outward) on the anode, and zero on the cathode. At later times j_r is negative on the anode and positive on the cathode. This behavior is more clearly shown in Fig. 29, and corresponds to the behavior of the luminous "hooks" discussed previously. Behind the sheet j_r was found to be zero at all axial positions.

F. ELECTRIC PROBE MEASUREMENTS

A point-by-point survey of the radial electric field was made at 1/8" intervals for conditions of 120 μ Hg argon, 10 kV. (Figs. 48 and 49). Double overlays were taken, moving the probe outward in 1/4" steps beginning at a radius of 5/8", and then inward in 1/4" steps beginning at a radius of 2-1/4". The Rogowski coil signal was recorded simultaneously on the lower trace of the oscilloscope, and a blanking pulse recorded simultaneously on both beams provided a time correlation.

The distribution of the radially inward electric field is sharply peaked, and the trajectory of this peak agrees well with the axial current maxima and snowplow results (Fig. 50). The E_r maxima exist at a slightly larger radius than the axial current maxima for all times, and move radially inward at the same velocity. It was found by simultaneous probing

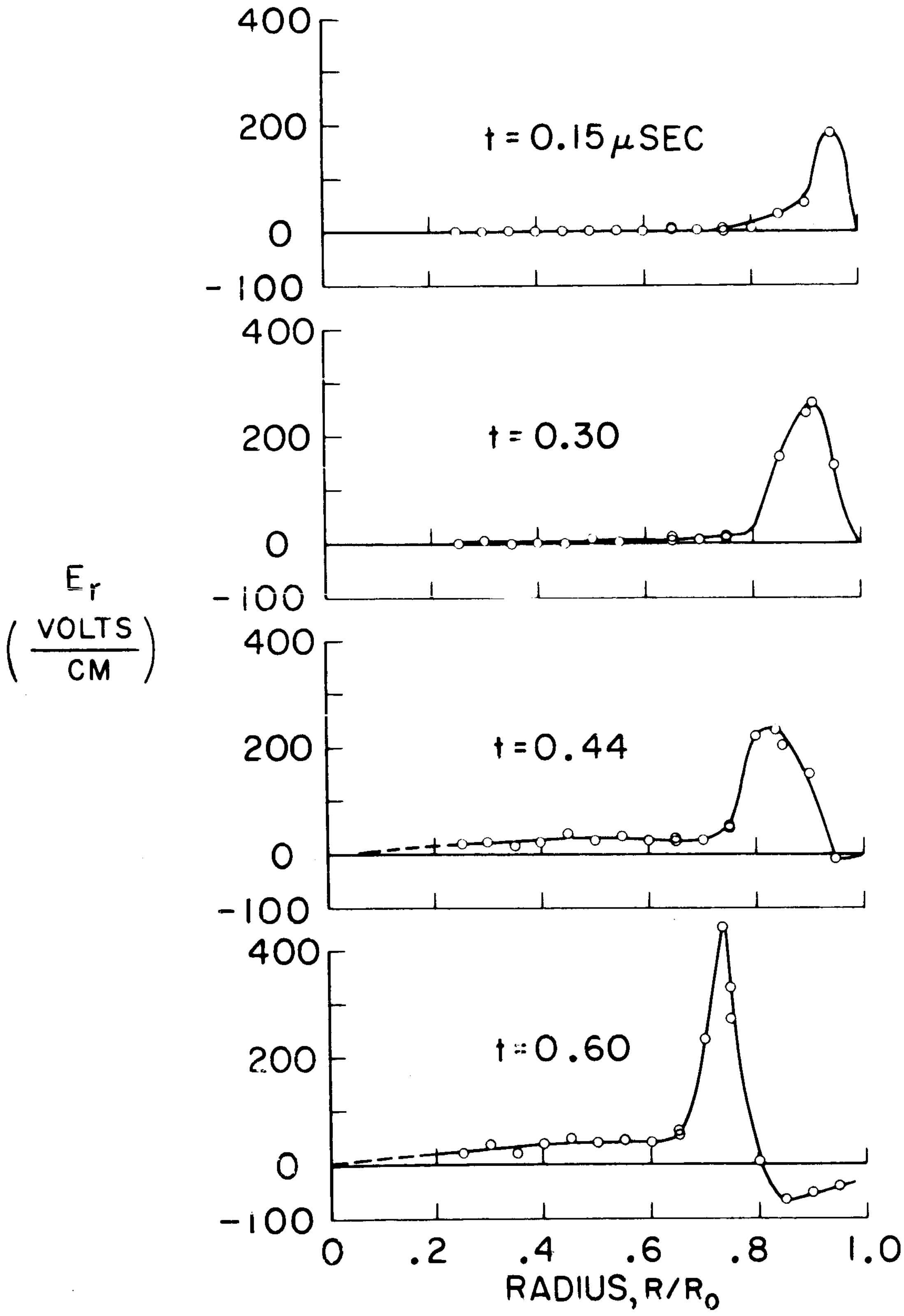

RADIAL ELECTRIC FIELD DISTRIBUTION, $z/h = 0.5$

5" CHAMBER, 120μ ARGON, 10 KV

AP25-4088-66

FIGURE 48

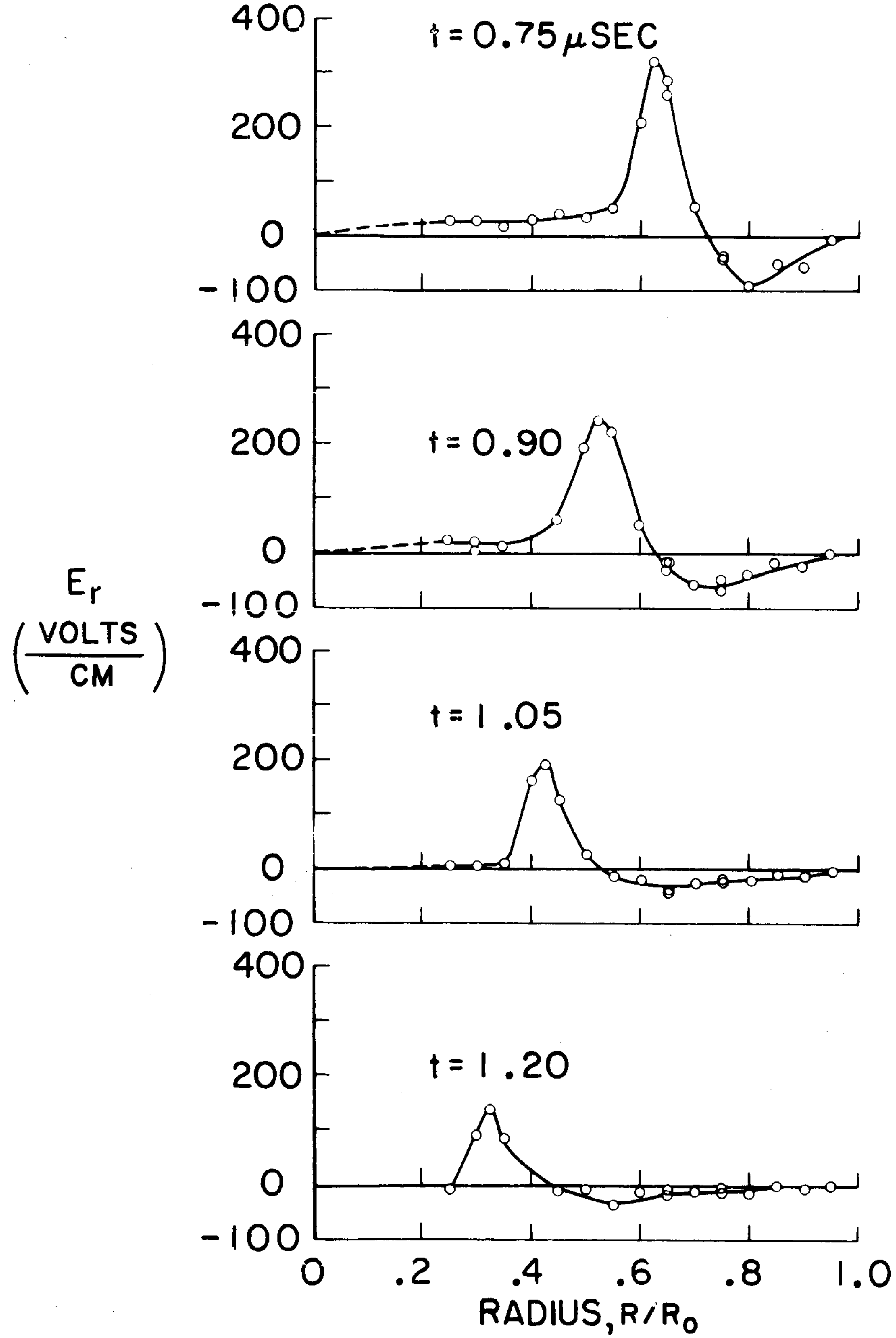

RADIAL ELECTRIC FIELD DISTRIBUTION, $z/h = 0.5$

5" CHAMBER, 120μ ARGON, 10KV

FIGURE 49

AP25-4089-66

AP25-4065-66

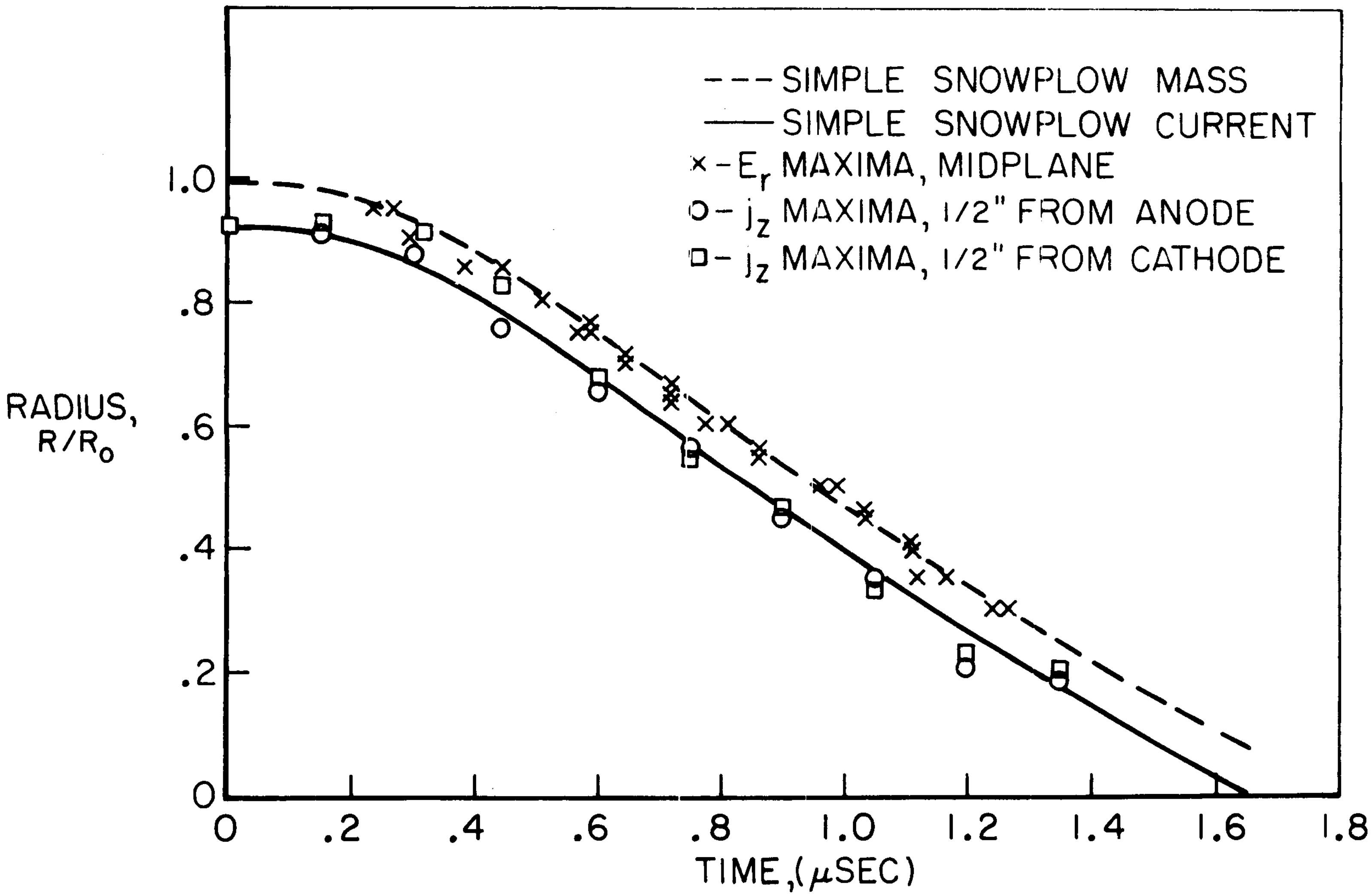

SNOWPLOW, AXIAL CURRENT, & RADIAL ELECTRIC FIELD TRAJECTORIES

5" CHAMBER, 120μ ARGON, 10KV

FIGURE 50

of the discharge with magnetic and electric field probes, that the radial separation between the E_r and $\dot{j}_z$ maxima in Fig. 50 is about 1.5 mm. Figure 51 is an oscillogram showing that the E_r maximum occurs .035 μsec later than the maximum in $\frac{\partial B_\theta}{\partial t}$. Interpreting the $\dot{B}_\theta$ probe trace in Fig. 51 as a convecting distribution of magnetic field, the 1.5 mm separation can be calculated. Furthermore, the E_r maximum is found to coincide with the maximum in electromagnetic force density $j_z B_\theta$. The equality of the electrostatic force density $en_e E_r$ and $\dot{j}_z B_\theta$ is discussed in Chapter IV.

The electric field distributions in Figs. 48 and 49 show that E_r is either zero or slightly positive (radially inward) far ahead of the current sheet, and rises sharply at the sheet. The pulse has a half width of about 7 mm, and behind the current sheet the electric field reverses direction, and points radially outward.

The small scatter in data points in the $E_r(r)$ distributions is due in part to the method of crossplotting the $E_r(t)$ records from the oscillograms. The pulse blanking marks and Rogowski coil records were initially used for time correlation in the r-t plot of maximum E_r (Fig. 50). A curve was fitted to the peak E_r data points, and this curve was assumed to represent the correct arrival time of peak electric field at each radius. In this way a smoothly varying function $E_r(t)$ was crossplotted into a smoothly varying function $E_r(r)$.

The integral of the radial electric field $\int_{r_1}^{r_2} E_r dr$ was

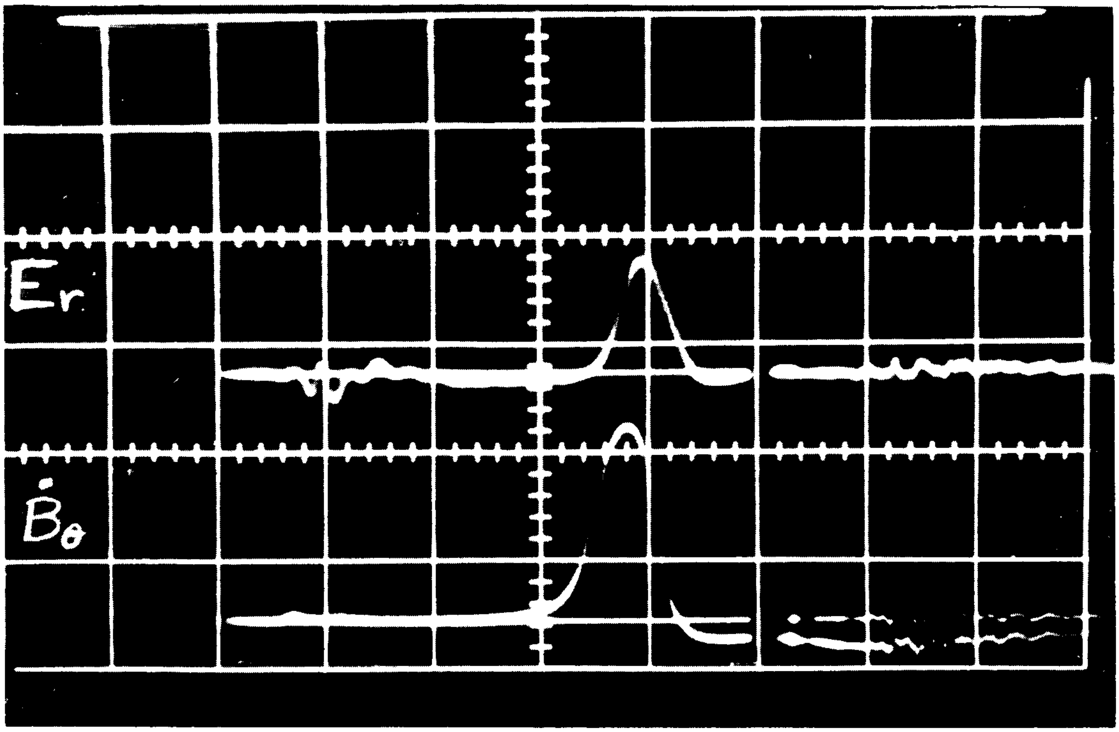

SIMULTANEOUS ELECTRIC AND MAGNETIC PROBE RESPONSES, E_r AND $\dot{B}_\theta$
120μ ARGON, 5" CHAMBER, $R/R_0 = .66, z/h = 0.5$

FIGURE 51

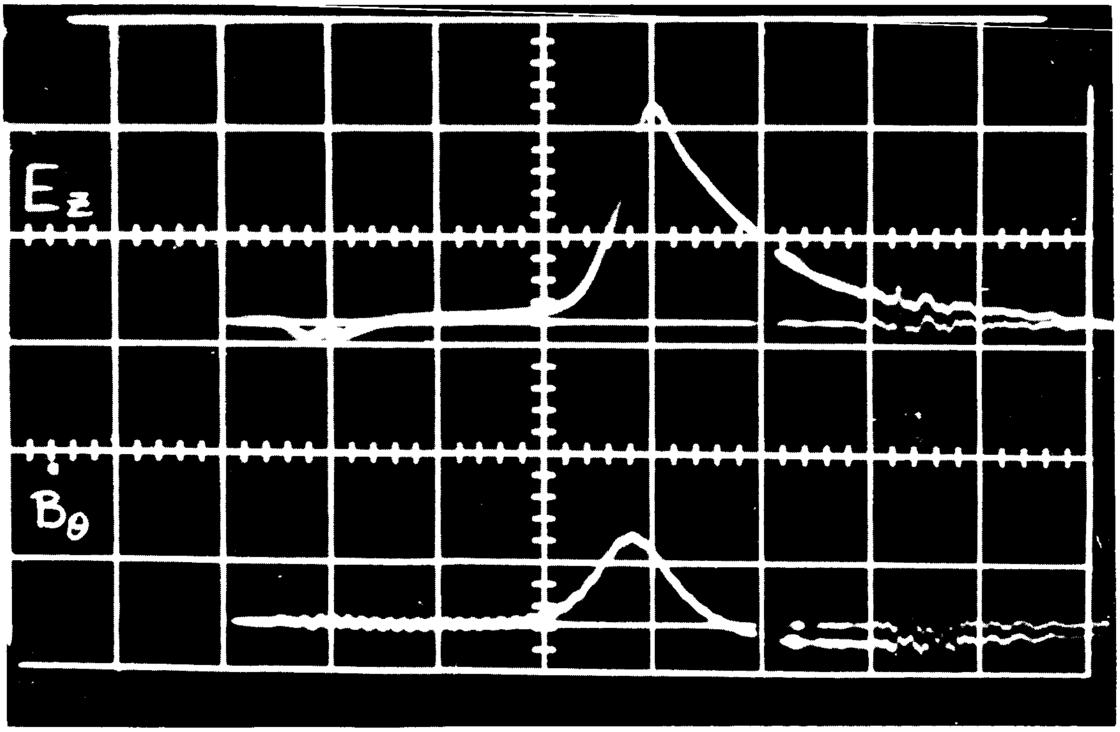

SIMULTANEOUS ELECTRIC AND MAGNETIC PROBE RESPONSES, E_z AND $\dot{B}_\theta$
120μ ARGON, 5" CHAMBER, $R/R_0 = .66, z/h = 0.5$

FIGURE 52

AP25 P53 66

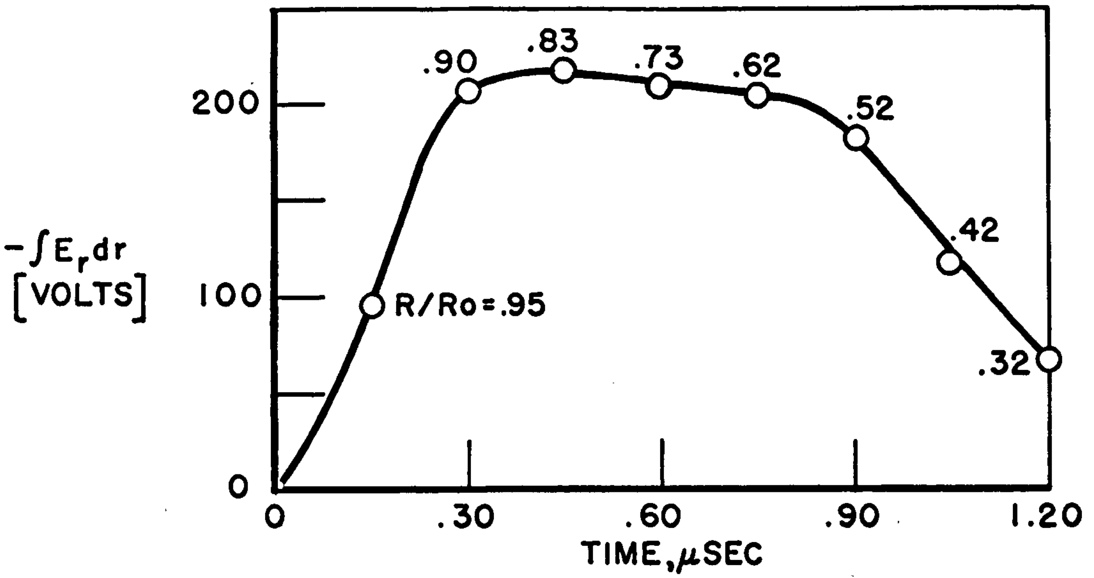

EXPERIMENTAL VOLTAGE ACROSS CURRENT SHEET, $-\int E_r dr$
5" PINCH, 120μ ARGON, 10KV

FIGURE 53

computed from the sheet leading edge, where E_r rises sharply, to the back of the sheet, where E_r falls to zero (Fig. 53). The resulting integral, which is equal to the change in electrostatic potential of an ion moving from the front to the back edge of the current sheet, is a function of sheet position, or equivalently, time. This potential across the current sheet achieves a value of more than ~200 volts at $R/R_o = .90$, remains constant to $R/R_o = .55$, and then decreases linearly for the remainder of the inward excursion.

It is important to notice that despite strong experimental evidence that the current sheet is effectively accelerating the bulk of the argon, the electrostatic energy drop across the current sheet is not sufficient to impart sheet velocity to a stationary singly charged ion. An argon ion in the gas in front

AP25-4/40-66

of the sheet has an energy of 430 e.v. with respect to the sheet, and less than half of this energy can be supplied by the electrostatic potential. A one-dimensional theoretical model of the current sheet is presented in Chapter IV, in which it is hypothesized that the ions are accelerated both by electromagnetic and gasdynamic pressure forces.

Two axial surveys of the axial electric field E_z were made at radii $R/R_0 = .48$ and $R/R_0 = .66$. These surveys established that E_z is induced by the magnetic field. A typical axial electric probe output versus time is shown in Fig. 52, compared with a $\dot{B}_\theta$ signal from a magnetic probe at the same position, $R/R_0 = .66$ and $z/h = .5$. The E_z probe signal begins to rise at the same time as the magnetic field, and as expected the waveform is similar to that of the inner voltage divider (Fig. 25). The peak of the E_z occurs .035 μsec later than the $\dot{B}_\theta$ peak, as was observed for the radial electric field (Fig. 51), and thus E_r and E_z reach their maxima at the same radial position. Unlike E_r , E_z does not fall quickly to zero, but remains at a large value far behind the current sheet.

Inner voltage divider measurements have established that the axial resistive electric field in the discharge is less than 10 V/cm. The total axial electric field is related solely to the changing magnetic flux from azimuthal magnetic field by Maxwell's equation:

$$\frac{\partial E_z}{\partial r} = \frac{\partial B_\theta}{\partial t}$$

where the axial gradient of E_r is assumed to be negligible.

Integrating from 0 to R/R_0, E_z is related to the induced magnetic flux field:

$$E_z = R_0\int_0^{R/R_0} \frac{\partial B_\theta}{\partial t}\, d\left(\frac{R}{R_0}\right) + E_z(0) \qquad [\text{volts/m}]$$

where $E_z(0)$ is the field on the chamber axis. Due to the relatively low value of conductivity on the chamber axis, electrodynamic skin effectsare negligible, and $E_z(0)$ may be identified with the resistive component of $\vec{E}$. The time derivative of the integrated magnetic probe data is plotted as a function of time (Fig. 54), compared with an E_z probe output, at $R/R_0 = .48$, midway between the electrodes. The electric probe signal begins to rise at .65 μsec along with the magnetic flux field, and peaks at 400 volts/cm at .97 μsec, in agreement with the magnetic probe data. A displacement of 0.05 μsec is found at the leading edge of the current sheet, but this is within the limit of accuracy with which magnetic probe data can be recorded in this environment. It is concluded that in the absence of plasma resistance, where the quantity $E_z(0)$ is small, the axial electric field distribution in the discharge chamber can be measured by a series of radial magnetic probe surveys.

The picture which emerges from the electric probe survey is illustrated in Fig. 55, relating the radial and axial components of the electric field in two coordinate systems. In the laboratory system in which the fields are measured, the electric field vector points radially inward and down toward

AP25-4066-66

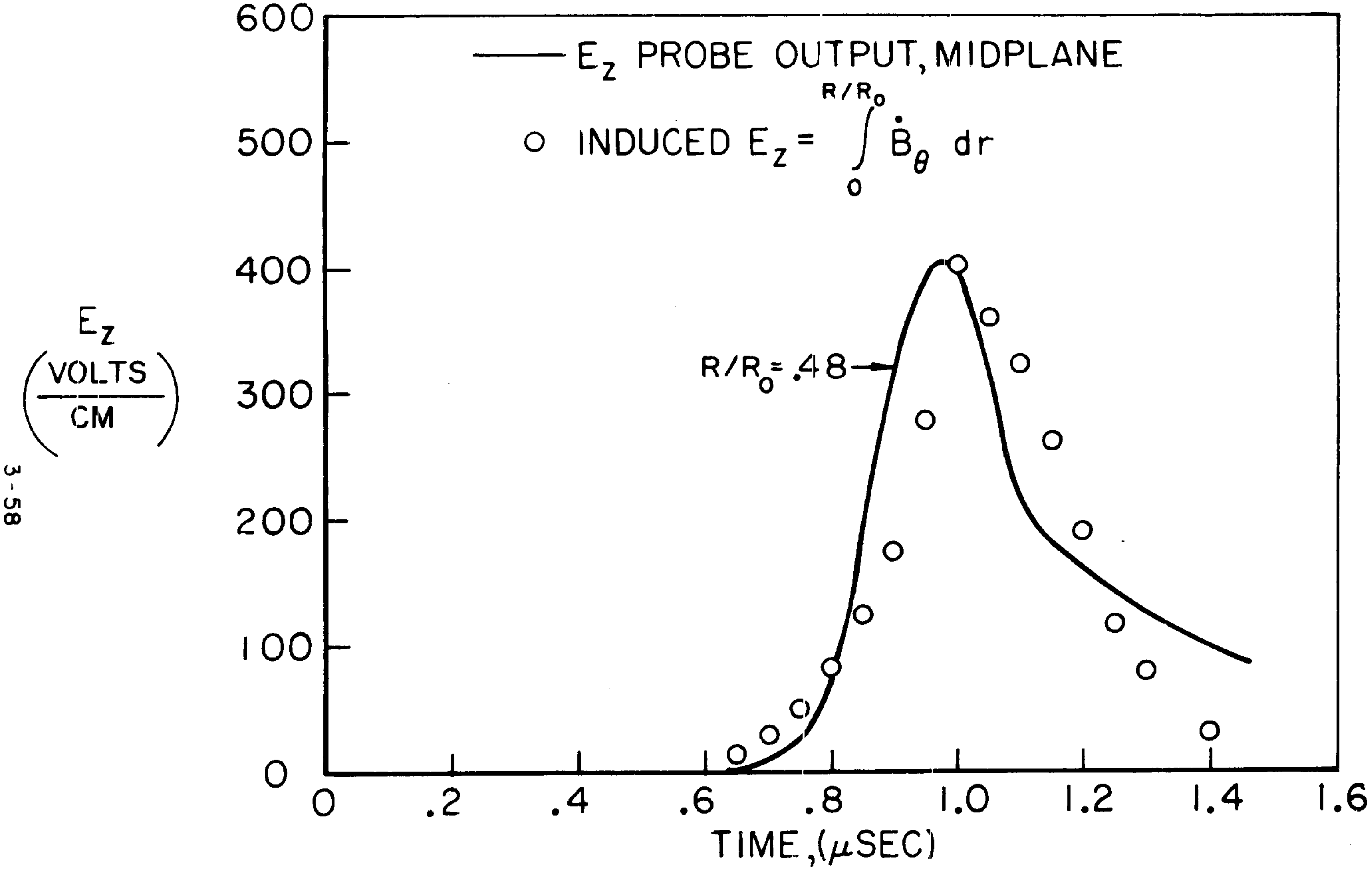

AXIAL ELECTRIC FIELD FROM ELECTRIC & MAGNETIC PROBES

FIGURE 54

AP25-4062-66

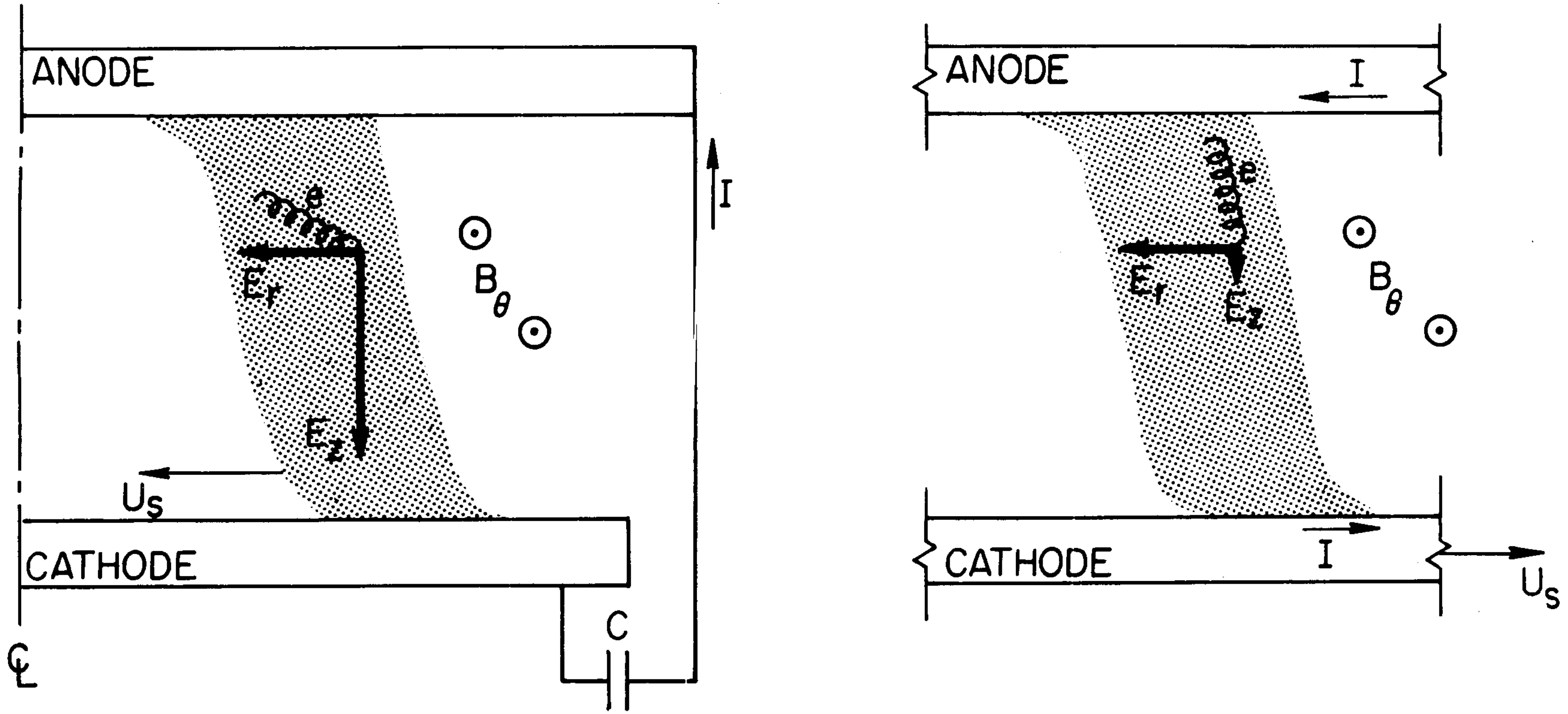

LABORATORY COORDINATES

MOVING COORDINATES

ELECTRIC FIELD COMPONENTS & ELECTRON $\vec{E} \times \vec{B}_\theta$ DRIFT

FIGURE 55

the cathode. The cycloid shows the trajectory of an average collisionless electron drifting perpendicularly to the crossed $\vec{E}$ and $\vec{B}$ fields. The electron drifts inward at sheet velocity and upwards toward the anode, thereby conducting current.

In the sheet coordinate system, moving radially at a velocity such that $\frac{\partial B_\theta}{\partial t}$ is locally zero, an observer sees no induced axial electric field, and the only E_z field is a small one due to finite plasma resistivity. Thus, electric field is predominately radial in the frame of the moving current sheet, and a collisionless electron in this frame drifts axially to the anode, conducting axial current.

Chapter IV

DISCUSSION AND THEORETICAL MODEL

A. ONE-DIMENSIONAL MODEL

In this chapter a simple model of the current sheet will be formulated to illustrate the origin and relation of the electric field to the properties of the current sheet. In the reference frame moving with the current sheet (Fig. 53), in which the dominant electric field component is radial, particles stream into the sheet from the left at velocity U_S . It is assumed that the electron temperature rises abruptly at the front of the sheet, so that the incoming particle stream will consist of ions and electrons, of equal density $n_+ = n_e = n$. Small deviations from charge neutrality must exist to account for E_r by Maxwell's equation, but these are less than 10^{-6} of the ambient density and may be ignored in Ohm's Law.

Adopting a right-handed coordinate system r, z, θ, such that B_θ points in the positive θ direction, Ohm's Law is written:

$$\vec{J} = \overleftrightarrow{\sigma} \cdot [\vec{E} + \vec{V} \times \vec{B}] \qquad [\text{amps/m}^2] \qquad (6)$$

where $\vec{V}$ is the plasma velocity relative to the frame in which $\vec{E}$ and $\vec{B}$ are measured. This equation is applied to the moving reference frame in which $E_z \approx 0$, and $\vec{V} \equiv U\hat{r} + V\hat{z}$ is then the velocity of the plasma with respect to the sheet. All net charge flux due to unsteady, viscous, pressure, and body force terms have been dropped. The largest of these neglected effects is the gradient of electron pressure ∇p_e, but it will be shown below that the electron temperature gradient is small, and thus ∇p_e is estimated to contribute only 1 percent of the axial current. For a plasma in which current is conducted only by electrons, the conductivity tensor is written:

$$\overleftrightarrow{\sigma} = \frac{\sigma_0}{1+\Omega^2}\begin{bmatrix} 1 & -\Omega & 0 \\ \Omega & 1 & 0 \\ 0 & 0 & 1+\Omega^2 \end{bmatrix} \tag{7}$$

where σ_0 is the scalar conductivity $\frac{ne^2}{m_e \nu_e}$, and $\Omega = \frac{eB_\theta}{m_e \nu_e}$, the Hall parameter. Based upon experimental estimates, the electron Hall parameter is larger than unity inside the current sheet, and the largest contributing terms to the current will thus be the two off-diagonal elements.

Having determined experimentally that j_r is much smaller than j_z, it will be useful to examine a one-dimensional current sheet model, in which the tilt angle φ and the radial current density j_r are equal to zero. The effects of a nonzero j_r are discussed below in part (B). From the axial component of the momentum equation:

$$\rho \frac{DV}{Dt} = j_r B_\theta = 0 \tag{8}$$

where V is the axial ion velocity, the axial pressure gradient is neglected, and j_r is zero by assumption. Since the axial velocity component V is zero in front of the sheet, and is therefore zero through the sheet by Eq. (8), the radial and axial components of Ohm's Law are written:

$$j_r = \sigma_{rr} E_r - \sigma_{rz} U B_\theta = \frac{\sigma_0}{1+\Omega^2}\left[E_r + \Omega U B_\theta\right] \qquad (9)$$

$$j_z = \sigma_{zr} E_r - \sigma_{zz} U B_\theta = \frac{\sigma_0}{1+\Omega^2}\left[\Omega E_r - U B_\theta\right] \qquad (10)$$

For $j_r = 0$, these equations become:

$$E_r = -\Omega U B_\theta \qquad (11)$$

$$j_z = e n \frac{E_r}{B_\theta} \qquad (12)$$

Equation (12) is the statement that the axial current is conducted by electrons in $\vec{E} \times \vec{B}$ drift, independent of the value of Hall parameter Ω. The equation can also be rearranged to show that the force on the electrons, $j_z B_\theta$, is equal to the force on the ions, enE_r. Furthermore, from Eq. (12) one may calculate the particle density n, from measured values of j_z, B_θ, and E_r. A typical density profile is plotted in Fig. 56, normalized to ambient density n_A, at 120 μ argon. The density ratio rises steadily through the sheet, reaching a compression ratio of about 6 at the point of maximum electric field. This calculation is accurate to within about 25 percent at the front and center of the current sheet, since the accuracy is limited only by the experimental measurement of B_θ and E_r.

AD25-R4169-66

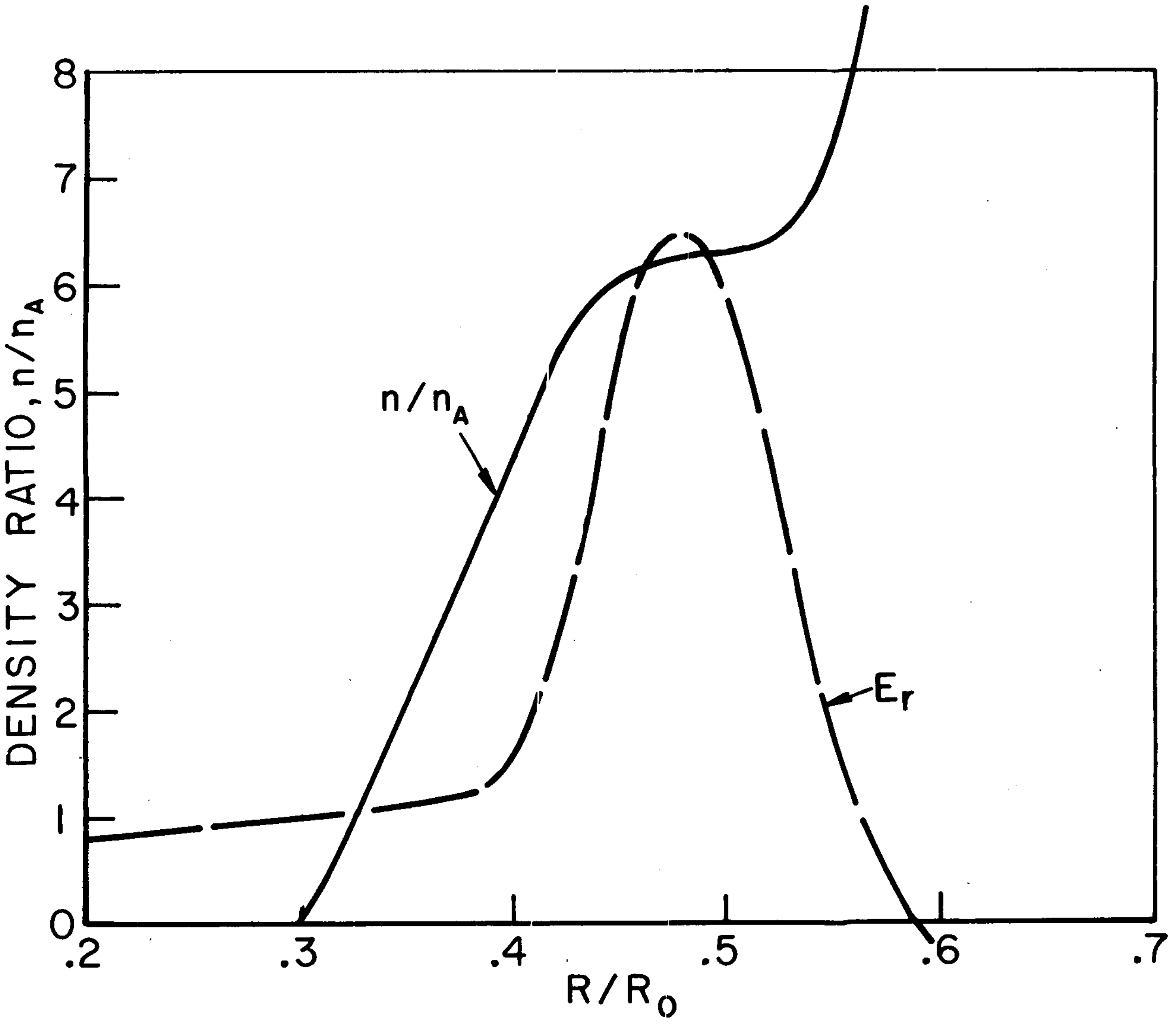

PARTICLE DENSITY VS RADIUS IN 5" PINCH
120μ ARGON, 10KV, t = .95 μsec

FIGURE 56

Moving further back in the sheet, however, the E_r field deviates strongly from the value it would have had in a truly one-dimensional current sheet. Specifically, the effect of finite radial current density causes E_r to reverse sign at the back of the sheet, as will be discussed below, and Eq. (12) is not valid in this region.

A second estimate of the density profile through the current sheet may be made by combining Eqs. (11) and (12):

$$j_z = -\sigma_0 U B_\theta \tag{13}$$

The collision frequency ν_c in the scalar conductivity σ_0 is calculated for a Maxwellian electron swarm in a neutral plasma where Coulomb collisions predominate, as described in Appendix C. Assuming that the density profile is steady (see discussion below), the continuity equation is written:

$$r n U = \text{constant} \tag{14}$$

Relating j_z to B_θ by Maxwell's equation:

$$\frac{n_A}{n(r)} = \frac{r}{r_s U_s \sigma_0 \mu_0} \frac{d \ln Br}{dr} = 145 \frac{r}{r_s U_s} T_{e\,[\text{e.v.}]}^{-3/2} \frac{d \ln Br}{dr} \tag{15}$$

In regions of the plasma where T_e is a constant, Eq. (15) states that $n(r)$ is inversely proportional to a logarithmic derivative, which can be evaluated to 20 percent accuracy from experimental magnetic probe data. Several processes compete to change electron temperature however, and it is not expected that T_e will remain constant through the sheet. It was argued above

(Chapter III) that the electron temperature within the sheet must be of the order of a few electron volts, the point at which the energy loss by inelastic collisions, thermal conduction, and radiation, balances the power input by ohmic heating. The sensitivity of the calculation of $n(r)/n_A$ to the profile of T_e may be inferred from Fig. 57, where $n(r)/n_A$ is plotted for two assumed temperature profiles. In the first, T_e assumes a constant value of 1.1 e.v. throughout the sheet. This particular value is calculated directly from Eq. (15) at the leading edge of the sheet, where the density ratio is assumed to be unity. In the second case, which more realistically approximates the actual temperature profile, T_e rises smoothly from 1.1 e.v. to a maximum of 3 e.v. at the sheet center, returning to 1.1 e.v. at the rear edge. Also included in Fig. 57 is the profile $n(r)/n_A$ from Fig. 56.

Because the current sheet is efficiently sweeping up and accelerating mass as it propagates inward, the density profile in the sheet is necessarily an unsteady one. To formulate a model of this unsteady process, one may envisage two alternate methods for storing the accumulated mass. In the first, the sheet volume remains constant, and incoming particles are stagnated in a reservoir of increasingly higher density. In the second, the sheet behaves like a strong, albeit thick, gasdynamic shock. Fluid passing through the sheet is accelerated to a large fraction of sheet velocity, and is compressed to a constant high density behind it, where it is stored in a region of increasingly larger volume. In both of these models the compressive effect due to the cylindrical geometry must be included.

AP25-R4170-66

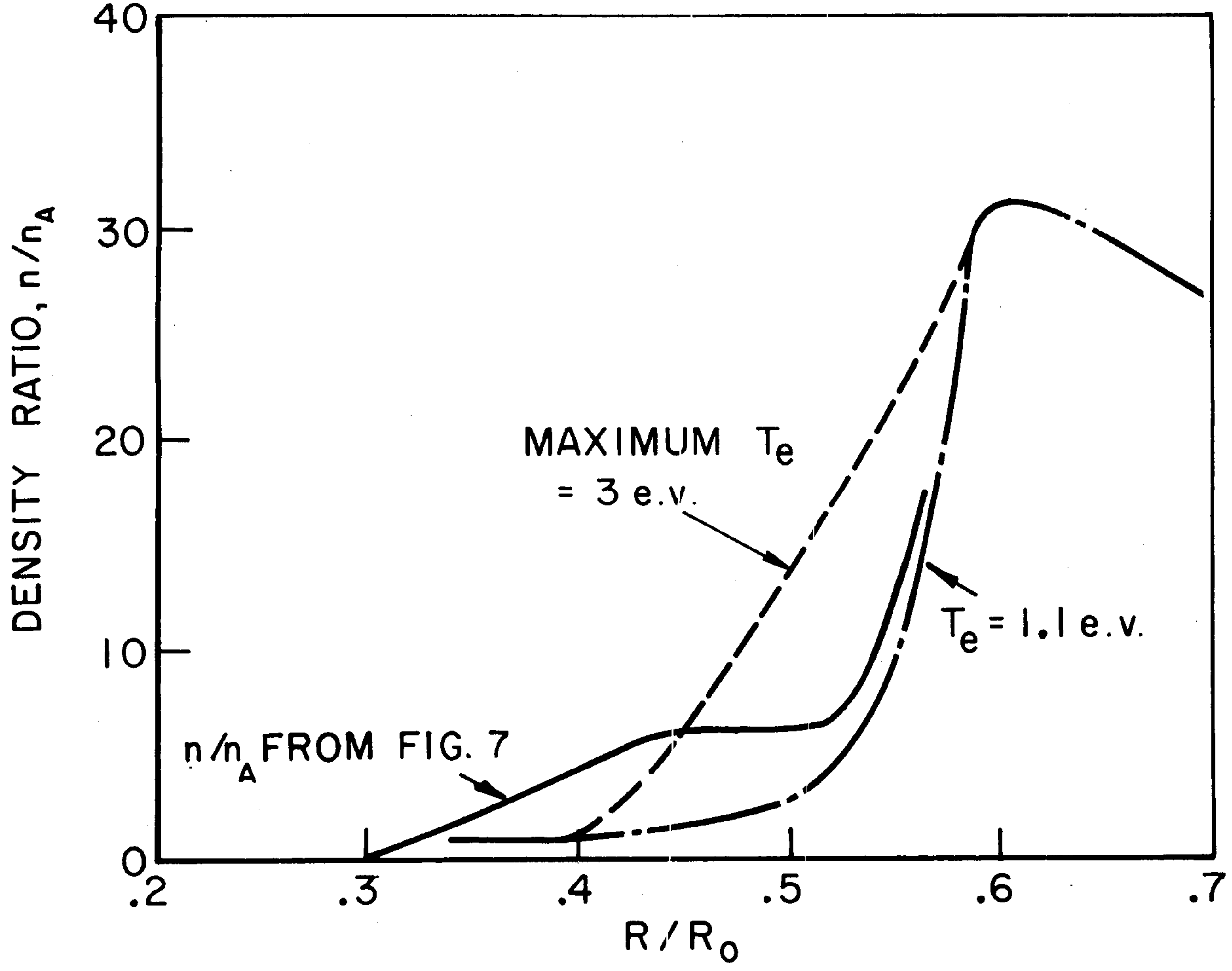

PARTICLE DENSITY RATIO VS RADIUS IN 5" PINCH,
120μ ARGON, 10KV, t = .95μsec

FIGURE 57

Unfortunately, the correct choice between these two unsteady models cannot be made on the basis of present experimental evidence. The difference between the constant volume and constant compression models will most readily manifest itself in a measurement of the time history of the density at the back of the sheet, or of the thickness of the high density region, and measurements of this type have proven extremely difficult. Lacking any experimental indication of the more proper point of view, the constant compression model has been adopted arbitrarily, largely because it has the virtue that the density profile becomes steady in the reference frame of the current sheet, over propagation distances small compared with the radius.

From this point of view it is then reasonable to write "jump conditions" across the entire sheet, and for propagation distances small compared with the sheet radius, to view the sheet as a steady, one-dimensional, dissipation zone. Replacing the radial coordinate by x, these conditions may be derived from the differential forms of the continuity, momentum, and energy equations, as written by S-I. Pai:(31)

$$\frac{d\,nU}{dx} = 0 \tag{16}$$

$$\rho U \frac{dU}{dx} + \frac{dp}{dx} + \frac{1}{2\mu_0}\frac{dB_\theta^2}{dx} = 0 \tag{17}$$

$$\rho U \frac{d}{dx}\left(h + \tfrac{1}{2}U^2\right) = \vec{j}\cdot\vec{E} + \frac{d}{dx}\left(\kappa \frac{dT}{dx}\right) - \frac{dq_R}{dx} + \frac{d}{dx}\left(U \tau_{ij}^{M}\right) \tag{18}$$

where q_R is the x component of the radiation energy flux,

τ_{ij}^{M} is the stress tensor minus the scalar pressure p, and the gas is perfect with equation of state

$$p = \rho R T \tag{19}$$

Each term in these equations may be immediately integrated through the current sheet, except $\vec{j}\cdot\vec{E}$. Because $\vec{j}$ is perpendicular to $\vec{E}$ in the sheet, $\vec{j}\cdot\vec{E}$ is zero, but it is instructive to examine $\vec{j}\cdot\vec{E}$ more closely. Solving Eq. (6) for $\vec{E}$, and taking the dot product with $\vec{j}$:

$$\vec{j}\cdot\vec{E} = \vec{j}\cdot\overleftrightarrow{\eta}\cdot\vec{j} + \vec{v}\cdot\vec{j}\times\vec{B} \tag{20}$$

Taking only the radial component of $\vec{v}$, and noting that $\eta_{zz} = 1/\sigma_0$, we have:

$$\vec{j}\cdot\vec{E} = \frac{j_z^2}{\sigma_0} + U j_z B_\theta \tag{21}$$

which could have been derived dirctly from Eq. (13). It must be concluded from Eq. (21) that the plasma does work on the fields at exactly the same rate as it is heated resistively.

Equations (16), (17) and (18) are now integrated, and yield the jump conditions between the leading edge, 1, and the trailing edge, 2:

$$n_1 U_1 = n_2 U_2 \tag{22}$$

$$\rho_1 U_1^2 + p_1 + \frac{B_1^2}{2\mu_0} = \rho_2 U_2^2 + p_2 + \frac{B_2^2}{2\mu_0} \tag{23}$$

$$h_1 + \tfrac{1}{2} U_1^2 = h_2 + \tfrac{1}{2} U_2^2 \tag{24}$$

where the heat conductivity, radiation, and viscous terms are set equal to zero in the flow ahead of and behind the current sheet. These equations resemble those for a purely gasdynamic discontinuity, except for the addition of magnetic pressure to the momentum equation (23). Dividing the momentum equation by $\rho_1 U_1^2$, the energy equation by $\frac{1}{2} U_1^2$, and neglecting the terms p_1, $\frac{1}{2\mu_0} B_1^2$, and h_1 :

$$\frac{p_2}{\rho_1 U_1^2} = 1 - \frac{n_1}{n_2} - \frac{\epsilon}{2} \tag{25}$$

$$\frac{2h_2}{U_1^2} = 1 - \left(\frac{n_1}{n_2}\right)^2 \tag{26}$$

The parameter ϵ in Eq. (25) is the ratio of magnetic energy density to streaming kinetic energy density $B_2^2/\mu_0 \rho_1 U_1^2$ and has a measured value of 1.33. (In the snowplow theory, for a constant velocity sheet $n_1/n_2 = 0$, $p_2 = 0$, and $\epsilon = 2$). As has been calculated by the one-dimensional model (Fig. 57), the compression n_2/n_1 is large compared to unity, and thus Eqs. (19), (25), (26) may be combined to give:

$$\frac{1}{2} U_1^2 = h_2 \tag{27}$$

$$1 - \frac{\epsilon}{2} = \frac{k}{2m_+ \overline{C_p}} \frac{n_2}{n_1} \tag{28}$$

where $\overline{C_p} \equiv h_2/T_2$ is an average specific heat for the compressed plasma. Equation (27) is the statement that the streaming kinetic energy of a particle ahead of the sheet appears as enthalpy behind the sheet, most of which is held by the ions, whose internal energy will be large. Equation (28) relates n_2/n_1 to the average specific heat $\overline{C_p}$ for the case of a constant velocity sheet. As ϵ approaches 2.0, $\overline{C_p}$ must become very large if the sheet is to retain a constant velocity. Taking experimental values for ϵ and U_1, T_2 may be related to n_2/n_1 :

$$\frac{n_2}{n_1} T_{2\,[\mathrm{e.v.}]} = 280 \tag{29}$$

For example, for $n_2/n_1 = 30$, $\overline{C_p} - 9.3 \times 10^3$ joules/kg °K (corresponding to $\overline{\gamma} = \frac{\overline{C_p}}{\overline{C_v}} = 1.02$), and $T_2 = 9.4$ [e.v.]. This ion temperature is larger than the electron temperature, and the ions therefore can heat electrons in and behind the sheet.

The electric field E_r can be related to the properties of the sheet by combining Eqs. (12) and (13):

$$E_r = -\frac{j_z^2}{\sigma_0}\left(\frac{1}{enU}\right) \qquad \left[\frac{\text{volts}}{\text{meter}}\right] \tag{30}$$

For a thin sheet at large radius, Eq. (30) can be written:

$$\frac{j_z^2}{\sigma_0} = -e n_A U_s \cdot E_r \tag{31}$$

Equation (31) states that the ohmic heating is proportional to the product of radial electric field and the radial ion current density. This implies that the origin of the radial electric field is collisional in nature, since by the definition of σ_0, E_r is proportional to the electron-ion collision frequency, ν_c. The exact balance between joule heating and work done on the plasma (Eq. 21) is now explained by Eq. (31). A flux of positively charged ions is acted upon by a force $-eE_r$, raising the ion potential energy. Simultaneously, an equal flux of negatively charged electrons is acted upon by an equal but opposite force eE_r, and the electrons lose potential energy, thereby doing work on the fields.

Using Eq. (31) and various experimentally measured sheet properties, one may calculate joule heating, scalar conductivity, and electron temperature distribution in the current sheet. A net joule heating rate in the sheet may be calculated by integrating Eq. (31) over the sheet volume, and applying the results of Fig. 53:

$$\int \frac{j_z^2}{\sigma_0}\, dV = -e n_A U_s (2\pi r_s h) \int E_r\, dr \qquad (32)$$

For the electric field distribution of Fig. 56, the following calculations may be made, as shown in Table II.

maximum electric field: $E_r = 1.6\times10^4$ V/m
maximum current density: $j_z = .93\times10^8$ amps/m^2
ohmic heating: $j_z^2/\sigma_0 = 4.7\times10^{11}$ joules/sec m^3
volume ohmic heating: $\int j_z^2/\sigma_0\, dV = 34\times10^6$ joules/sec
scalar conductivity: $\sigma_0 = 1.9\times10^4$ mhos/m
electron-ion collision frequency: $\nu_c = 3.7\times10^{10}$/sec
electron temperature: $T_e = 2.2$ e.v.
electron Hall parameter: $\Omega = 3.0$

TABLE II

As shown above, the volume ohmic heating for the case chosen is 34 joules/μsec, a power loss which is 5-10 percent of the total power input to the chamber. The total ohmic heating loss up to pinch time is less than 100 joules. Because much of the energy of the ohmic heating is lost by inelastic processes, and therefore is not useful for propulsion, a propellant should be chosen which would miminize the ohmic heating. The correct choice is not entirely straightforward, because the excitation potential varies from gas to gas, and this potential influences the electron temperature and hence the conductivity. Therefore the question is most simply answered by direct measurement.

The relative importance of ohmic heating was checked in neon, argon, and krypton (molecular weights 20, 40, 84). The chamber mass density was kept nearly constant for each gas, so that in all three cases the sheet velocity was constant, $U_s = 4.3\text{x}10^4$ m/sec. The probe output $E_r(t)$ was converted to $E_r(r)$ by a Galilean transformation as described in Chap. III, and the results are plotted in Fig. 58 for 240 μ Hg. of neon, 120 μ Hg. of argon, and 70 μ Hg. of krypton. In these three gases the value of the peak electric field varies only slightly. The current sheet widens, however, as molecular weight increases. The effect of gas type on the sheet properties is illustrated in Table III (see Table II for units).

AP25-R4168-66

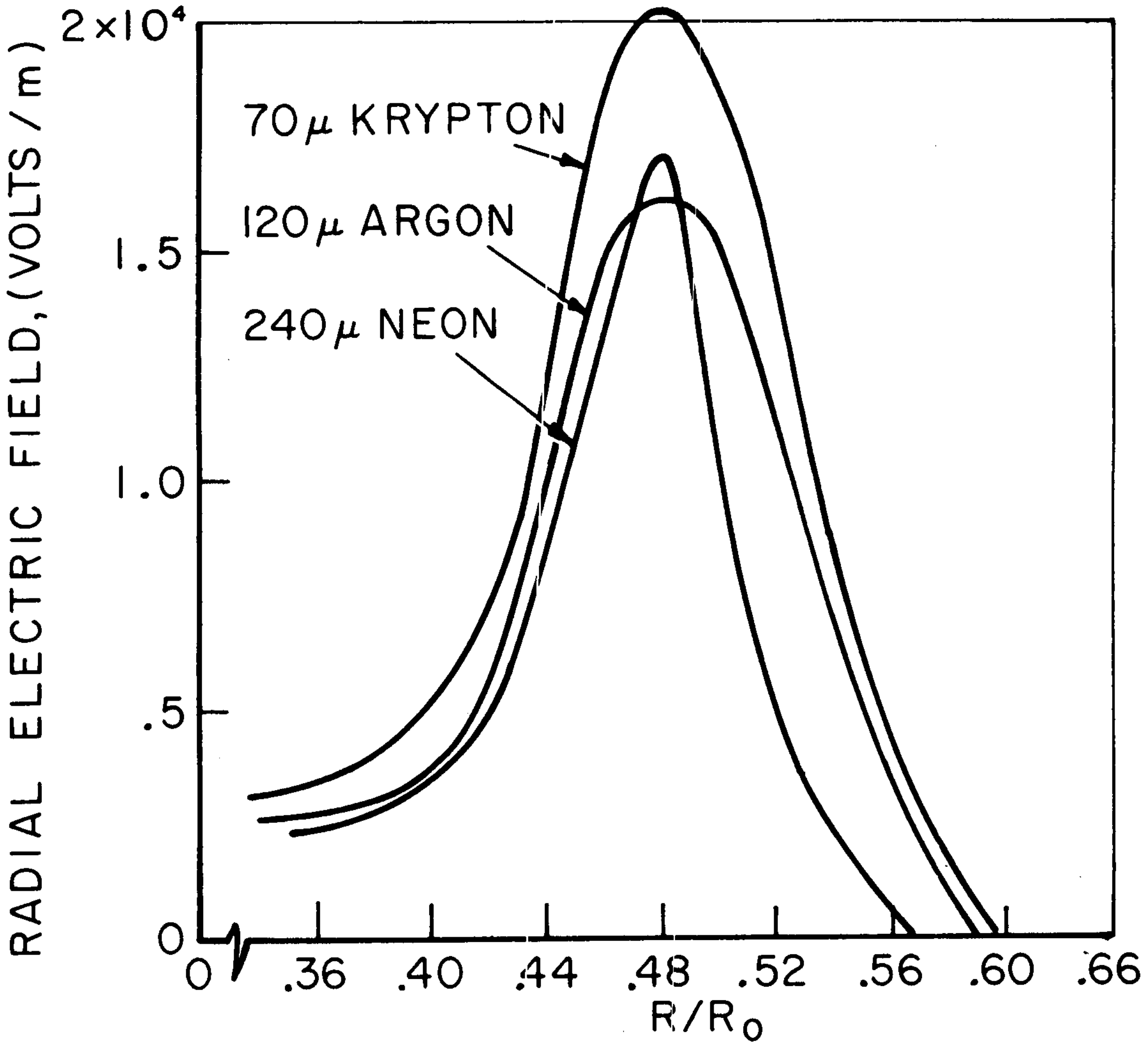

RADIAL ELECTRIC FIELD PROFILES IN NEON, ARGON, AND KRYPTON, 5" PINCH, 10KV

FIGURE 58

	Neon 240μ	Argon 120μ	Krypton 70μ
maximum E_r	$1.7x10^{4}$	$1.6x10^{4}$	$2.0x10^{4}$
maximum j_z	$.77x10^{8}$	$.93x10^{8}$	$.74x10^{8}$
ohmic heating, j_z^2/σ_0	$10x10^{11}$	$4.7x10^{11}$	$3.4x10^{11}$
volume ohmic heating, $\int j_z^2/\sigma_0 \, dV$	$48x10^{6}$	$34x10^{6}$	$26x10^{6}$
scalar conductivity, σ_0	$.593x10^{4}$	$1.9x10^{4}$	$1.6x10^{4}$
electron-ion collision frequency, ν_c	$23.3x10^{10}$	$3.7x10^{10}$	$2.5x10^{10}$
electron temperature, T_e	1.0	2.2	2.0
electron Hall parameter, Ω	.48	3.0	4.4
1st excitation potential, e.v.	16.6	11.5	9.9

TABLE III

The data in Table III shows a trend toward lower ohmic heating as molecular weight $\mathcal{M}$, increases. The effect of large $\mathcal{M}$ is to permit a lower ambient particle density while keeping mass density and sheet velocity constant, thereby decreasing the ion current. This density effect is only partially offset by a thickening of the current sheet, suggesting that efficient pulsed accelerators should use high molecular weight gases.

B. TILT OF THE CURRENT SHEET

The slight tilting of the current sheet toward the axis of the discharge is evident in luminous photographs (Figs. 18 and 21), and in magnetic field data (Fig. 31). The fact that the radial current $\dot{j}_r$ is nonzero will allow the ions to acquire an axial velocity, as indicated in Eq. (8). For a small tilt angle, φ, the axial and time dependence of axial flow velocity V may be neglected, radial current can be written as $j_r \approx \varphi j_z$, and Eq. (8) is written:

$$\rho U \frac{dV}{dr} \approx \varphi \dot{j}_z B_\theta \tag{33}$$

To the approximation that the sheet is thin compared to its radial position, Eq. (33) is simply integrated, giving the axial ion velocity

$$V(r) \approx -\frac{\varphi}{2\mu_0 m_+ n_A U_s} B_\theta^2 \tag{34}$$

where nU has again been assumed constant. For example, when $\varphi = 3^\circ$, $V \approx -1.7\times10^3$ m/sec, directed toward the cathode, a value less than 4 percent of the sheet speed. The ion current density may be relatively high near the back of the sheet, however, due to the high particle density. Assuming a compression ratio $n_2/n_1 = 30$, the ion current at the back of the sheet is 3.3×10^7 amps/m^2, a value 25 percent of the peak current density.

The expression used previously for axial current (Eq. 12) must be modified in the region behind the sheet to include ion current:

$$j_z \rightarrow ne\left(\frac{E_r}{B_\theta} + V\right) \qquad (35)$$

Although j_z is relatively small behind the sheet, it is never observed to reverse sign. In the region where E_r points radially outward, $|V|$ must exceed $\left|\frac{E_r}{B_\theta}\right|$ by Eq. (35), in order to keep the current from reversing sign. Using measured values of $\left|\frac{E_r}{B_\theta}\right|$ in the region behind the sheet, $|V|$ must exceed 10^4 m/sec, a value 6 times larger than that estimated by Eq. (34). Despite this quantitative discrepancy in the measurements, it seems clear that the electric field reversal behind the sheet counteracts the axial ion current induced by the tilt of the current sheet, making total j_z behind the sheet nearly zero.

C. SUMMARY OF RESULTS OF THE THEORETICAL MODEL

To summarize the above theoretical description, the discussion has concentrated on the central part of the current sheet, far from the regions of the cathode and anode "foot." It has been shown on the basis of a one-dimensional model that the ohmic heating is equal to the product of radial electric field and radial ion current. Jump conditions, written for a one-dimensional, constant velocity, constant compression sheet, indicate a particle compression ratio n_2/n_1 much larger than unity, depending on the value of the average specific heat ratio. Also, the ion temperature behind the sheet is found to be larger than electron temperature. Experiments in neon, argon, and krypton at constant mass density show that lowering particle density by increasing molecular weight decreases the ohmic heating. The tilting of the current sheet explains qualitatively the sign reversal of radial electric field behind the current sheet.

Appendix A

THE SNOWPLOW MODEL

The snowplow model of the current sheet, discussed in an earlier publication,(32) is herein modified in two ways. A constant resistance, the sum of constant chamber and external circuit resistances, is introduced into the circuit equation. Secondly, the radial position of the current sheet and mass sheet are allowed to differ by a constant amount. Let

R_0 = radius of chamber
L_0 = inductance of external circuit
h = electrode separation
C = capacitance of bank
V_0 = initial voltage on capacitors
ρ_0 = ambient mass density of test gas

and introduce eight dimensionless parameters:

$$\tau = \frac{t}{\sqrt{L_0 C}} \qquad r(\tau) = \frac{R_p}{R_0}$$

$$q(\tau) = \frac{Q}{CV_0} \qquad \alpha = -\frac{\mu_0 h}{2\pi L_0}$$

$$\beta = -\frac{\mu_0 (CV_0)^2}{4\pi^2 \rho_0 R_0^4} \qquad \Delta r = \frac{R_c - R_p}{R_0} = \text{CONSTANT}$$

$$OHM = \frac{\text{CIRCUIT RESISTANCE}}{\sqrt{\frac{L_0}{C}}} \qquad GAM = \frac{\text{CHAMBER RESISTANCE}}{\text{CIRCUIT RESISTANCE}}$$

where τ is time, R_p and R_c are mass and current radius, Q is charge on the capacitor bank and $\mu_0 = 4\pi\times10^{-7}$ [h/m]. With inductance in the form

$$L = L_0 + \frac{\mu_0 h}{2\pi} \ln \frac{R_0}{R_c}$$

the dimensionless snowplow circuit and momentum equations become:

$$[1+\alpha \ln(r+\Delta r)]\ddot{\varphi} + \left(\frac{\alpha}{r+\Delta r}\dot{r} + OHM\right)\dot{\varphi} + \varphi = 0$$

$$r\frac{d}{d\tau}[(1-r^2)\dot{r}] - \beta(\dot{\varphi})^2 = 0$$

The voltage across the chamber at R_0 is:

$$V_{ch} = [\alpha \ln(r+\Delta r)]\ddot{\varphi} + \left[\frac{\alpha}{r+\Delta r}\dot{r} + GAM\cdot OHM\right]\dot{\varphi}$$

These equations were evaluated on an IBM 1620 for specified values of the dimensionless parameters. The quantities α and β are fixed for given values of gas density, initial voltage, and external inductance. L_0 was measured from the ringing frequency of the circuit with the chamber shorted. The initial current sheet radius was taken from experimental results. Initial mass sheet radius was assumed to be unity, so that all the chamber mass was swept up. Initial current sheet velocity was zero. The resistance OHM was selected to damp the snowplow current maximum to the known measured value from the Rogowski coil. Likewise, GAM was chosen to make the snowplow voltage maximum agree with the measured maximum from the high voltage probe. The values used in evaluating the dimensionless parameters were:

chamber radius : $R_o = .063$ [m]
chamber height : $h = .0508$ [m]
external inductance : $L_o = 7.65\text{x}10^{-9}$ [h]
bank capacitance : $C = 15.68\text{x}10^{-6}$ [fd]
initial voltage : $V_o = 10{,}000$ [volts]
gas density (120 μ argon): $\rho_o = 2.6\text{x}10^{-4}$ [kg/m^3]
sheet separation : $R_c - R_p = .0044$ [m]
total circuit resistance : $\Omega_T = .00553$ [ohm]
chamber resistance : $\Omega_c = 0$

The computed snowplow circuit current and chamber voltage show excellent agreement with the measured current and voltage up to $t = 0.60$ μsec, at which time a second (negative) current sheet begins to flow at large radius.

The computed snowplow trajectories $R(t)$ are compared with the measured current density and radial electric field maxima in Fig. 50. Agreement is good until the current gets very close to the chamber center.

Appendix B

DESIGN OF ELECTRIC PROBE PULSE TRANSFORMER

An isolation-step down pulse transformer, pictured in Fig. 7, was designed to reproduce faithfully a 0.4 μsec flat topped, fast rising pulse from a low source impedance. Following Millman and Taub,(33) the equivalent circuit of the transformer is shown below:

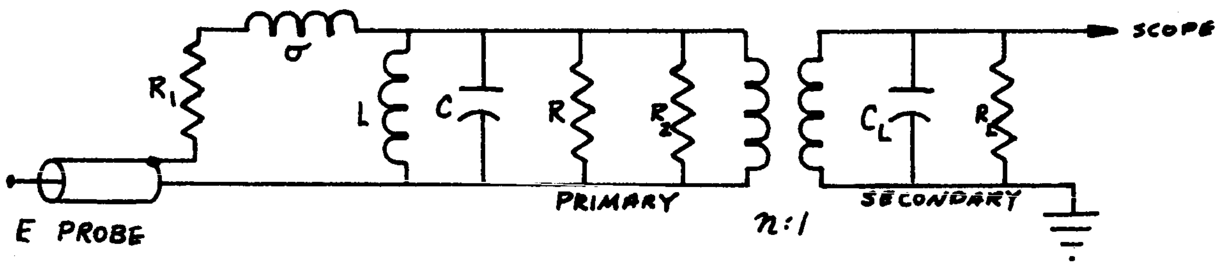

where R_1 is the resistance of the probe plus primary winding, σ is the leakage inductance of the primary, C is the interwinding capacitance C' plus the reflected load capacitance C_L/n^2, R is the probe cable termination, and R_2 is the reflected load resistance $n^2 R_L$.

The rise time at the secondary, for a square pulse to the E probe, is:

$$t_r = 3.35\left(\frac{\sigma C R_2}{R_1 + R_2}\right)^{1/2} \quad [\text{sec}]$$

when the circuit is critically damped. Critical damping is achieved by making the damping constant k equal to unity:

$$k = \left(\frac{R_1}{\sigma} + \frac{1}{R_2 C}\right)\frac{\sqrt{\sigma C}}{2}$$

For large n , R_2 is much greater than R_1 , and the formula for risetime t_r is simplified. The capacitance C is fixed by the number of feet of coaxial cable to the scope, the scope preamplifier input capacitance, the turns ratio n , and the interwinding capacitance, and is approximately 2×10^{-12} fd. for $n = 8$, and the cable lengths used in the experiment. Risetime can only be further reduced by reducing σ , and this is done by winding the primary tight to the transformer core.

The resistance R_1 was set at 50 ohms, by placing a 50 Ω resistor, visible in Fig. 7, in series with the primary. The leakage inductance σ was estimated to be 5×10^{-5} henries, and the quantity R_1/σ can be dropped from the expression for k . Requiring $k = 1$ thus gives:

$$R_2 = n^2 R_L = \frac{1}{2}\sqrt{\frac{\sigma}{C}} \approx 5000\,\Omega$$

For $n = 8$, an estimate of R_L is thus 78 Ω . In the laboratory, R_L was adjusted to get a nearly square leading edge on the pulse, and turned out to be 200 ohms.

Note that only the primary winding must be tight on the ferrite core to give low leakage inductance and good frequency response. The secondary winding can be spaced away from the core to reduce the common mode response, and thus the secondary was wound on an 1" nylon bobbin in this design.

The remaining design parameter is the primary inductance L , which determines the percentage decay of a flat topped pulse of width t_p . The fractional droop in voltage after the initial rise is given by

$$F = \frac{t_p}{L} \frac{R_1 R_2}{R_1 + R_2} \approx \frac{R_1 t_p}{L}$$

with $R_1 = 50\,\Omega$ and $t_p = 0.4\,\mu\text{sec}$, the inductance L was approximately $200\text{x}10^{-5}$ henries for a 1 percent droop. This was achieved with 32 turns on a type W-03 ferrite core. With $n = 8$, four turns were wound on the secondary.

The response of the transformer to a 30 nsec risetime pulse from a 1.25 ohm noninductive source, was found to be 45 nsec. Due to transformer heating losses, the overall attenuation was a factor of 10.0, for the 8 to 1 turns ratio.

Appendix C

CALCULATION OF ELECTRON
AND ION COLLISION PROPERTIES

Preceding any discussion of ion and electron trajectories, in the current sheet it is necessary to compare the particle mean free paths, Larmor radii, and other characteristic plasma lengths. The plasma is considered to be fully ionized, electrically neutral, and composed of streaming singly charged ions, and an electron swarm having a Maxwellian distribution. The electron thermal energy is two orders of magnitude less than the ion kinetic energy relative to the current sheet, but because of the small electron mass, electron thermal velocity is two orders of magnitude larger than the ion velocity. Assuming then that the heavy ions are stationary with respect to the thermal electrons, it is shown by Spitzer that the largest contribution to electron-ion collision frequency is from small angle coulomb deflections, which rapidly accumulate to 90°.(20) The reciprocal of Spitzer's "90° deflection time" defines a frequency for 90° deflection of the electrons:

$$t_D^{-1} = A \frac{n_e \ln \Lambda}{v_e^3} \quad [sec^{-1}]$$

where A is a constant, n_e and v_e are electron density and velocity, and the cutoff parameter Λ is the ratio of Debye length to the impact parameter for a single 90° deflection, and has a value of $\ln \Lambda \approx 6$ in this plasma. Following Wharton and Heald,(34) the velocity dependent collision frequency t_D^{-1} is averaged over a Maxwellian distribution, yielding the "effective collision frequency" in a constant electric field:

$$\nu_{eff} = .855 \times 10^{-12} \frac{n_e \ln \Lambda}{T_e^{3/2}}$$

with T_e in e.v., n_e in m^{-3}, and $\ln \Lambda \approx 6$. This calculation does not include magnetic field, but these effects are not important until the electron Larmor radius becomes smaller than the Debye length, which is not the case here.

Spitzer calculates the "self-collision time," for a perturbed electron distribution to become Maxwellian, by electron-electron small angle coulomb collisions:

$$t_{ce}^{-1} = 3 \times 10^{-6} \frac{n_e \ln \Lambda}{T_e^{3/2}} \quad [sec^{-1}]$$

The "self-collision time" for argon ions scales from t_{ce} as the square root of the electron-ion mass ratio:

$$t_{c+}^{-1} = 1.1 \times 10^{-8} \frac{n_e \ln \Lambda}{T_+^{3/2}} \quad [sec]$$

This expression for t_{c+} only holds up to $T_+ \approx 5$ e.v. At this temperature the distance of closest approach equals the ion's outer electron shell diameter, and at higher temperatures the cross section is no longer coulombic, but is approximately constant, so that t_{c+}^{-1} increases as $\sqrt{T_+}$.

Following Petschek and Byron,(29) the rate of argon atom excitation is calculated by integrating the velocity dependent collision frequency $n(v)\,Q(v)\,v$ over a Maxwellian distribution.

The excitation cross section is assumed to vary linearly with electron energy above the 11.5 e.v. argon first excitation potential, with slope:

$$S = 4.38\times10^{-3} \; [\mathrm{m}^2/\mathrm{joule}]$$

This value of the slope is a fit to experimental data of Maier-Leibnitz,(35) whose results are more readily available from a paper by Druyvesteyn and Penning.(36) The excitation rate, which controls the ionization process, is:

$$\nu_{ex} = \frac{(2k)^{3/2}}{\sqrt{\pi m_e}} S n_e \sqrt{T_e}\,(T_{ex}+2T_e)\, e^{-T_{ex}/T_e} \; [\mathrm{sec}^{-1}]$$

where MKS units apply. If the density n_e is to be expressed in $[\mathrm{m}^{-3}]$, and the temperatures are in electron volts, then

$$\nu_{ex} = 4.68\times10^{-16} n_e \sqrt{T_e}\,(11.5+2T_e)\, e^{-11.5/T_e}$$

The reciprocal of ν_{ex}, the excitation time t_{ex}, is plotted in Fig. 24 for $n_e = 10^{22}$ $[\mathrm{m}^{-3}]$.

Corresponding to the above elastic and inelastic collision events are mean free paths, defined as particle velocity divided by the collision frequency. The neutral excitation mean free path, for example, equals U_s/ν_{ex}. These mean free paths are compared in Fig. 59, together with the electron and ion Larmor radius, and Debye length, for typical values of density, temperature, and magnetic field.

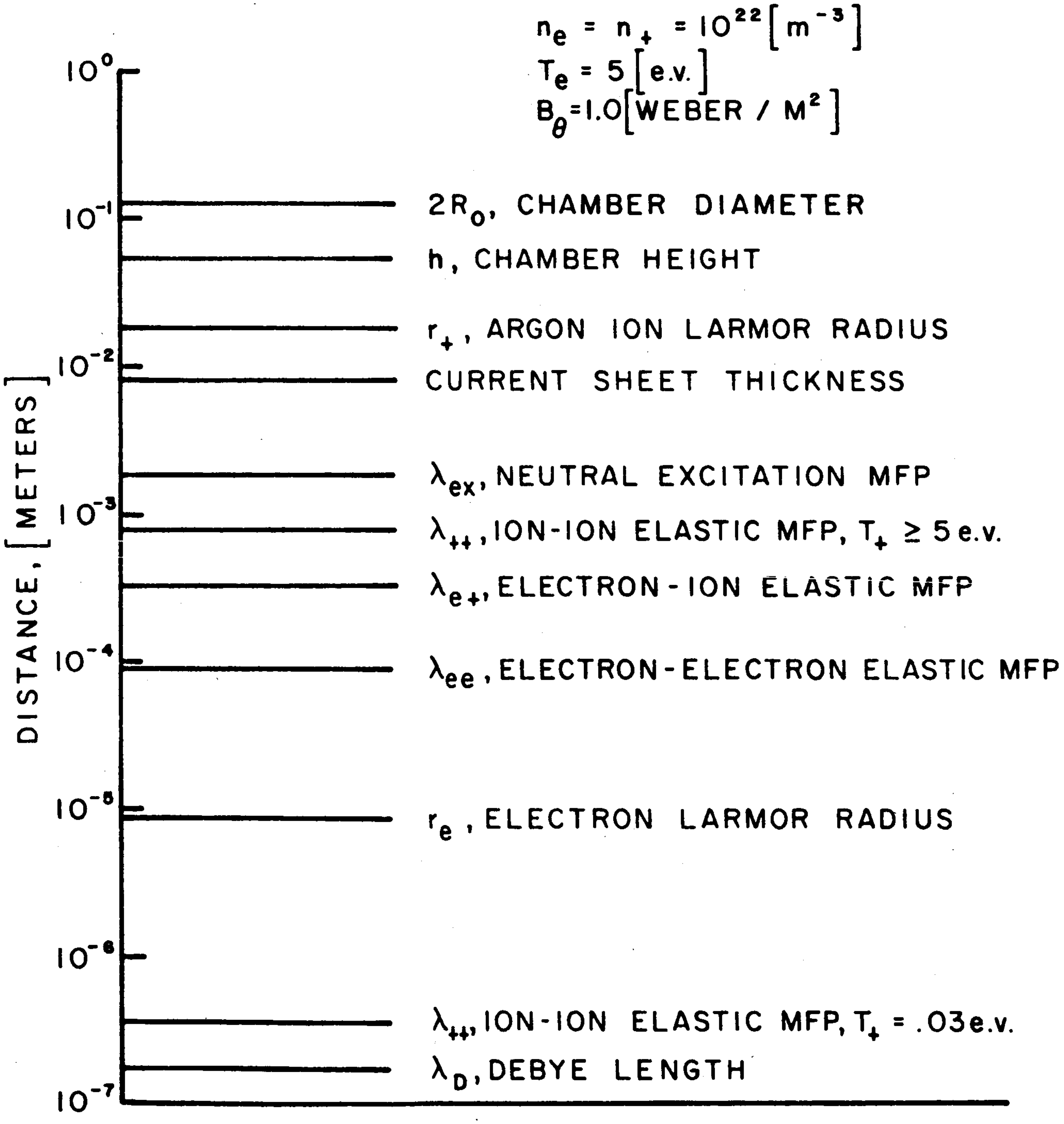

AP25-4167-66

COMPARISON OF MEAN FREE PATHS AND LARMOR RADII FOR ARGON IONS AND ELECTRONS IN THE 5" PINCH

FIGURE 59

ACKNOWLEDGEMENTS

I especially wish to thank my advisor, Professor Robert G. Jahn, who suggested this investigation, and by his insight and encouragement, kept a sometimes jumbled problem continually in focus. Much of the flavor of this work reflects his teaching. I also wish to thank Professor Ralph H. Lovberg, who has developed several of the diagnostic techniques used in this research. As a thesis reader, Professor Lovberg also contributed greatly to the interpretation of the later phases of the work. Thanks are due to Professor George Bienkowski, from whom the author gained a better understanding of the diagnostic techniques, and who as a thesis reader, helped formulate the theoretical model. Woldemar F. von Jaskowsky contributed in discussions almost daily, and aided greatly in interpreting the spectral data. Professor William Criminale contributed in many fruitful discussions, mathematical in nature.

My thanks are extended to the members of the Electric Propulsion Group. In particular, Albert L. Casini was the indispensable man in the laboratory, both in building equipment and encouraging me to better efforts.

Valuable assistance was given by the staff of the Guggenheim Laboratories Design Group. Mr. Tony Poli, Mrs. Ann Jansak, and Mrs. Kathryn Walter prepared the necessary drawings. Mr. Donald Neiler contributed his photographic ability to the data reduction, and to the preparation of slides and prints.

ACKNOWLEDGEMENTS

Mr. Jack Cooper contributed to the design of various pieces of diagnostic equipment.

I am grateful for having been the recipient of fellowships granted by the Ford Foundation, and by the National Science Foundation. Financial support for the laboratory was provided by the National Aeronautics and Space Administration, under grant NsG-306-63.

To my wife Debby go my thanks for her patience and encouragement, towards what must have seemed at times to be a long and unprofitable venture. To her this thesis is dedicated.

REFERENCES

1. R. L. Garwin and M. Rosenbluth, "An Infinite Conductivity Theory of the Pinch," AEC LA 1850, (1954).

2. S. A. Colgate, "Initial Conditions for the Dynamic Pinch," AEC UCRL 4895, (1957).

3. I. Granet and W. J. Guman, "Some Engineering Aspects of Magnetohydrodynamic Pinch Process for Space Propulsion." Republic Aviation, PPL Report #120, (1959).

4. G. Rowell, "Cylindrical Shock Model of the Plasma Pinch," Princeton University, Department of Aerospace and Mechanical Sciences, Rept. No. 742, (1966).

5. V. O. Jensen, et al., "An Experiment on Magnetically Driven Shocks," Research Establishment Riso Report No. 28, (1961).

6. J. E. Allen, "An Elementary Theory of the Transient Pinched Discharge," Proc. Phys. Soc. B, 70, 24 (1957).

7. G. C. Vlases, "Experiments in a Cylindrical Magnetic Shock Tube," J. Fluid Mech. 16, Pt. 1, 82 (1963).

8. Y. Sorrell, Private Communication, Karman Laboratory, Cal. Tech., (1966).

9. L. C. Burkhardt and R. H. Lovberg, "Current Sheet in a Coaxial Plasma Gun," Phys. Fluids 5, 341 (1962).

10. R. Lovberg, "Inference of Plasma Parameters from Measurement of $\vec{E}$ and $\vec{B}$ Fields in a Coaxial Accelerator," Phys. Fluids 7, S57 (1964).

11. R. B. Johansson, "Current Sheet Tilt in a Radial Magnetic Shock Tube," Phys. Fluids 8, 866 (1965).

12. R. H. Lovberg, "Acceleration of Plasma by Displacement Currents Resulting from Ionization," Proc. VI. Int. Conf. on Ionization Phenomena in Gases, Vol. IV., p. 235 (Paris, 1963).

13. J. C. Keck, "Current Distribution in a Magnetic Annular Shock Tube," Phys. Fluids 5, 630 (1962).

14. R. H. Lovberg, "Schlieren Photography of a Coaxial Accelerator Discharge," Phys. Fluids 8, 177 (1965).

15. T. J. Falk, "Current-Layer Diffusion in a One-Dimensional Magnetic Pinch," Ph.D. Thesis, Cornell U., (1963).

16. K. Thom, J. Norwood, and N. Jalufka, "Velocity Limitation of a Coaxial Plasma Gun," Phys. Fluids 7, S67 (1964).

17. R. G. Jahn, W. von Jaskowsky, and A. L. Casini, "Gas-Triggered Pinch Discharge Switch," Rev. Sci. Instr. 36, 101 (1965).

18. R. H. Lovberg, Private Communication.

19. R. H. Lovberg, "Magnetic Probes," in "Plasma Diagnostic Techniques," by R. H. Huddlestone and S. L. Leonard, ed., Academic Press, New York, (1965), Chapter 3.

20. L. Spitzer, Jr., "Physics of Fully Ionized Gases," 2nd Ed., Interscience Publishers, New York, 1962.

21. S. H. Lam and M. Greenblatt, "Flow of a Collisionless Plasma over a Cone," AIAA J. 3, 1850 (1965).

22. D. Bohm, "The Characteristics of Electrical Discharges in Magnetic Fields," (A. Guthrie and R. K. Wakerling, eds.) McGraw-Hill, New York, (1949).

23. F. F. Chen, "Electric Probes," in Plasma Diagnostic Techniques," by R. H. Huddlestone and S. L. Leonard, ed., Academic Press, New York, (1965), Chapter 4.

24. J. P. Appleton, "Electrical Precursors of Ionizing Shock Waves," Phys. Fluids 9, 336 (1966).

25. H. D. Weymann and L. B. Holmes, "Plasma Density Ahead of Pressure-Driven Shock Waves," Bull. Am. Phys. Soc, 10, 1143 (1965).

26. E. O. Johnson and L. Malter, "A Floating Double Probe Method for Measurements in Gas Discharges," Phys. Rev. 80, 58 (1950).

27. "Pulsed Electromagnetic Gas Acceleration, Fourth Semi-Annual Progress Report," Princeton University, Guggenheim Laboratories for the Aerospace Propulsion Sciences, Rept. No. 634c,(1964).

28. K. E. Harwell and R. G. Jahn, "Initial Ionization Rates in Shock-Heated Argon, Krypton, and Xenon," Phys. Fluids 7, 214 (1964).

29. H. Petschek and S. Byron, "Approach to Equilibrium Ionization Behind Strong Shock Waves in Argon," Cornell University, Graduate School of Aeronautical Engineering, Ithaca, New York (1955).

REFERENCES-cont'd

30. G. Sutton and A. Sherman, "Engineering Magnetohydrodynamics," McGraw-Hill, Inc., New York, 1965.

31. Shih-I. Pai, "Energy Equation of Magneto-Gas Dynamics," Phys. Rev. 105, 1424, (1957).

32. R. G. Jahn and W. von Jaskowsky, "Current Distributions in Large-Radius Pinch Discharges," AIAA J. 2, 1749 (1964).

33. J. Millman and H. Taub, "Pulse and Digital Circuits," McGraw-Hill, Inc., New York, (1956), Chapter 9.

34. M. A. Heald and C. B. Wharton, "Plasma Diagnostics with Microwaves," John Wiley and Sons, Inc., New York, (1965).

35. Maier-Leibnitz, Z. Physik 95, 499 (1935).

36. M. J. Druyvesteyn and F. M. Penning, "Electrical Discharges in Gases," Rev. Mod. Physics 12, 87 (1940).